MAX-PLANCK-INSTITUT FÜR KOLLOID- UND GRENZFLÄCHENFORSCHUNG

Polymers from the Natural Product Betulin; A Microstructural Investigation

Dissertation

zur Erlangung des akademischen Grades

"doctor rerum naturalium"

(Dr. rer. nat.)

in der Wissenschaftsdisziplin "Kolloid- und Polymerchemie"

eingereicht an der

Mathematisch-Naturwissenschaftlichen Fakultät

der Universität Potsdam

von

Jekaterina Jeromenok

geb. in Tallinn, Estland

Golm, 12.03.2012

Tag der mündlichen Prüfung: 03.07.2012
1. Gutachter. Prof. Dr. Markus Antonietti
2. Gutachter. Prof. Dr. Hans-Jürgen Holdt
3. Gutachter. Prof. Dr. Michael Meier

Published online at the
Institutional Repository of the University of Potsdam:
URL http://opus.kobv.de/ubp/volltexte/2012/6138/
URN urn:nbn:de:kobv:517-opus-61380
http://nbn-resolving.de/urn:nbn:de:kobv:517-opus-61380

Table of contents

1 Introduction

There is an uncountable number of known porous materials nowadays. New materials are extensively synthesised, investigated and utilised on industrial scale. Recently, much attention has been focused on microporous materials with interconnected pores of size less than 2 nm, due to their significant potential applications in separation processes and gas storage, as catalyst support, or as sorbents.[1–4] The most prominent examples are zeolites and activated carbon, which are used as heterogeneous catalysts, as adsorbents and in molecule separation.[5] With the arising interest towards ordered crystalline metal-organic frameworks (MOFs) and covalent-organic frameworks (COFs), the subject of microporous *polymers* has gained more importance as well.[6] Their lightweight organic components and functionalisability attract the attention for potential industrial implementation. During the last eight years, enormous efforts have been applied to the development of so called PIMs, polymers with intrinsic microporosity. These materials possess an amorphous, chemically well-defined structure with high surface areas. The first known PIMs were based on spirocyclic molecules which prevent the aggregation of the stiff planar components. [7–13] Generally, highly rigid and nonlinear linking groups are essential for space-inefficient packing and thus forming materials with interconnected pores and voids, hereby preventing structural relaxation and consequent loss of microporosity.

Many valuable porous polymers have been synthesised and adapted for utilisation in energy storage, gas separation, medical and catalyst applications etc.[4,14–16] Conventional methods for rendering these polymers are often based on environmentally noxious reactants and involve non-economical procedures. However, there has been significant advance in the use of renewable resources in a variety of applications in polymer science, including plant oils, glycolides and furfural compounds.[17–19] Compared to those approaches, a rather small amount of work was dedicated to the use of terpenes.[20,21]

This work focuses on a low-cost preparation and analysis of polymers from the natural product betulin. Betulin is a naturally occurring triterpene, which is one of the major components of birch bark and could be available as a large scale byproduct of the wood industry. Depending on the birch species, its content can be as high as ca. 30%. Its rigid structure of four six- and one five-membered interconnected rings should serve as a contortion site preventing efficient packing of the polymer chains. Polymers based on betulin have already been made before [22–24], but to my best knowledge, there have been no reports on synthesis and investigations of porous, betulin-containing polymers. Moreover, this work sets a distinct accent in the characterisation techniques for microporous materials. It is remarkable that nitrogen adsorption at 77 K has remained the most widely used standard characterisation method for analysing surface area and pore size distribution of porous materials. Nevertheless, there are some shortcomings known, especially in the case of microporous materials. A more detailed analysis can though be achieved by using both various adsorbates of different kinetic diameters and conducting several experiments at different temperatures to overcome the energy barrier associated with the hindered entrance through narrow pores.[25]

The motivation for this work is the synthesis and investigation of polymer materials from a renewable natural resource, betulin. The polymers are thoroughly analysed with regard to their porosity by means of gas adsorption, X-ray scattering and NMR spectroscopy.

The first part is devoted to the synthesis and characterisation of insoluble polyester networks based on betulin. The emphasis is put on gas adsorption analysis and the study of intrinsic microporosity of the networks with different post-treatment. The focus of the second part lies on soluble betulin-containing polymers. Linear and hyperbranched structures are introduced and analysed in relation to gas separation applications. Synthesis and investigations of other betulin-based polymers are outlined in the third part. The summary is presented in “Conclusions and Outlook”.

2 Background

2.1 Porous polymers

According to IUPAC, pores are divided into three groups with respect to their size. The smallest ones with interconnected pores of the diameter of less than 2 nm are called micropores. Mesopores lie in the region between 2 nm and 50 nm and macropores are larger than 50 nm.[26,27]

Macroporous materials with pores larger than 50 nm in diameter are commonly prepared by methods which can be divided in templating or non-templating. Emulsion templating and utilising porogens belong to the first technique, whereas thermally induced phase separation, phase separation during cross-linking and gas blowing are the most common approaches of the latter.[28] One of the most famous examples of a large scale industrial macroporous polymer, synthesised by using a porogen, is polystyrene (Styropor™, Styrofoam™). It is polystyrene, pre-expanded with pentane. Generally the surface energies of macroporous systems are not that high, which allows stable non-crosslinked materials.

Most prominent examples of mesoporous materials, with pore sizes of 2-50 nm, are silicates and metal oxides. Employing the self-assembly approach, the first ordered mesoporous materials emerged in the early 1990s.[29] The block copolymers and surfactants aggregate in three-dimensional mesostructures and can be removed after the successful templating e.g. by oxidation, calcination or extraction.[30] The first prominent largely ordered mesoporous silica, MCM-41, was synthesised via liquid crystal templating under basic conditions in 1992.[31] Templating with block copolymers in acidic media led to another famous representative of mesoporous silica, SBA-15.[32] Lately, there has been increasing interest towards mesoporous *polymers*, prepared via hard- or soft-templating. The former procedure is based on using rigid templates like mesoporous silica,

whereas the latter involves utilising soft, i.e. more dynamic structures like block copolymer surfactants and micelles.

Microporous materials contain interconnected pores of less than 2 nm in diameter and possess high internal surface area, which provides potential use in gas adsorption, separation and heterogeneous catalysis. The class of conventional amorphous materials includes silica and activated carbon. The crystalline materials are represented by crystalline inorganic networks such as zeolites.[5]

Polymers with intrinsic microporosity can be generally regarded as polymers with high free volume.[33,34] The high free volume polymers were first described by *Masuda et al.*[35] in his pioneering research on polyacetylenes.

Free volume V_f is a fraction of a polymer volume which is not occupied by the polymer chains. To discuss this phenomenon in more detail there are some physical properties, which need to be introduced. The specific volume V is the reciprocal to polymer density. It contains the volume occupied by the polymer molecules and the free volume of the material. Free volume is frequently calculated as the difference between the total and a zero point volume, which is estimated from the extrapolation of the densities of crystalline or liquid materials at 0 K.[13,36] With the commonly accepted value of

$$V_f = V - 1.3V_W \qquad (2\text{-}1)$$

where V_w is the specific van der Waals volume, the fractional free volume f_v is

$$f_V = \frac{V - 1.3V_W}{V} \qquad (2\text{-}2)$$

The fractional volume generally lies in the range of 0.10-0.23 for common polymers.[6] The factor 1.3 is introduced to take into account the fact that even for a perfect crystal at absolute zero, there is a limit to the obtainable packing density. There are, however, other definitions of free volume which result in smaller values because they count in the thermal vibrations within the occupied volume. Moreover, when probed by other molecules (e.g. nitrogen adsorption), the detected free volume is dependent on the size of the probe molecules. The temperature dependence of the specific volume is depicted in Figure 1. The specific volume increases with temperature, whereby after the glass transition temperature T_g the slope runs steeper since the expansion coefficient is higher in the rubbery state (above T_g) than in the glassy state (below T_g). At a given temperature *T,* the non-equilibrium excess free volume increases with increasing of T_g. On rapid cooling of a rubbery polymer the excess of free volume is trapped within the polymer. If a polymer is then annealed at a temperature slightly lower than T_g, the chains relax to lower energy conformations, which results in loss of the confined free volume. This process is also called isothermal volume recovery or physical aging.

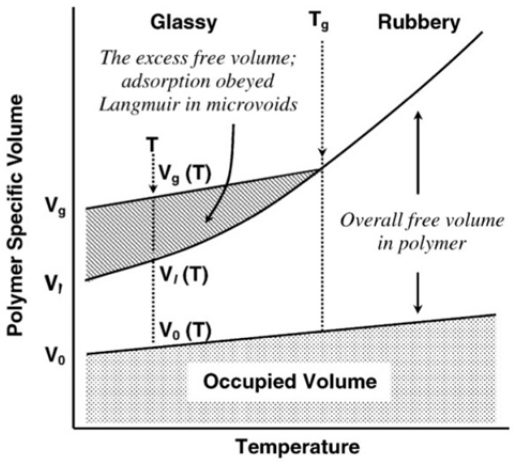

Figure 1. Schematic representation of the temperature dependence of the polymer specific volume in an amorphous polymer (reprinted from [37]).

The excess of free volume can also be captured by quick removal of a swelling solvent. In this case it can also be lost with physical aging. Thus, the microporosity of a material built via interconnected voids of the excess of the free volume can be lost because of the isothermal volume recovery.

Rubbery polymers are in a hypothetical thermodynamic equilibrium liquid state and their gas solubility obeys Henry's law.[37] The glassy polymers, however, are assumed to be in a non-equilibrium state, consisting of two components; a hypothetical liquid state and a solid state. The gas sorption of these polymers is described and analysed by the dual-mode sorption model.[38,39] This model is based on two types of solutions that obey Henry´s law dissolution and Langmuir-type sorption. The former is associated with the dissolution of gases into rubbery polymers and low molecular weight liquids. The latter is related to Langmuir-type sorption in porous solids. The Langmuir sorption sites in a glassy polymer correspond to holes or microvoids which arise from the non-equilibrium nature of glassy polymers. The dual-mode sorption model is described by the following equation:

$$C = C_D + C_H = k_D p + \frac{C'_H b p}{1 + b p} \qquad (2\text{-}3)$$

C is the total gas concentration in a glassy polymer; C_D is the concentration of "dissolved" molecules based on Henry´s law; C_H is the gas concentration in microvoids, based on Langmuir sorption; k_D is the Henry´s law coefficient; b and C'_H are the Langmuir hole affinity parameter and the capacity parameter, respectively. The k_D parameter represents the penetrant dissolved in the polymer matrix at equilibrium and b outlines the sorption affinity for a particular gas-polymer system. C'_H is often utilised to determine the amount of the non-equilibrium excess free volume. It was discussed that in gas sorption measurements the dual sorption process is responsible for the elastic deformation by increasing gas pressures and thus a hysteresis of the desorption branch.

Polymers with intrinsic microporosity are constituted of a continuous three-dimensional network of molecular-sized voids between the rigid chain macromolecules.[40] Normally, polymers try to maximize the attractive interactions between the chains and pack closer, i.e. minimising the amount of void space. The rotational and conformational flexibility allows the chains to rearrange to a more compact structure, maximising inter- and intramolecular cohesive forces and thus efficiently filling the space in the solid. The packing efficiency of any polymer depends on the physical state (amorphous or crystalline) and molecular structure (shape, flexibility) and can be altered e.g. by heat treatment and solvent swelling.[6] It should be remembered that high internal surface area is associated with the large interfacial energy of the system, which predestines polymers to deform. The contribution of Young´s modulus to the free energy of the system needs to be larger than the surface energy (comparing absolute values), which is why microporous polymers are mostly crosslinked. The cross-linking binds the polymer chains together and thus prevents the pore collapse, which would minimize the surface energy.

There are several approaches to synthesize microporous polymers, i.e. polymers possessing large free volume. Firstly, they can be prepared through reversible formation of linkages under thermodynamic control, e.g. covalent organic frameworks (COFs). These porous crystalline networks are connected with strong covalent bonds and can exhibit large surface areas up to 4210 $m^2 \cdot g^{-1}$.[41,42] Secondly, free volume can be trapped in amorphous hypercrosslinked polymer (HCP), which on removal of the included solvent can form micropores.[6] And finally, polymers with intrinsic microporosity can be designed from rigid and contorted monomers, which connected to macromolecules, prevent efficient spatial packing of the chains, resulting in high free volume.[9] In the following, all three groups of polymers are shortly presented.

The first reports on ordered covalent organic frameworks, COFs, have been done by *Yaghi* in 2005.[41] It was shown that linking of six-membered boroxine or five-membered BO_2C_2 rings is reversible and allows the scaffold to rearrange itself

under thermodynamic control. The formation of *COF-1* is illustrated in Figure 2. Successful synthesis of COFs from light non-metallic building units is appealing for applications such as catalysis and gas storage. Based on the same principle, covalent triazine-based frameworks, CTFs, have been synthesised and investigated. One of the superior features of CTFs comparing to metal-containing MOFs is their inertness towards water which could make them more desired for possible industrial applications. CTFs were proven to be effective in low temperature methanol oxidation catalysis.[43–46]

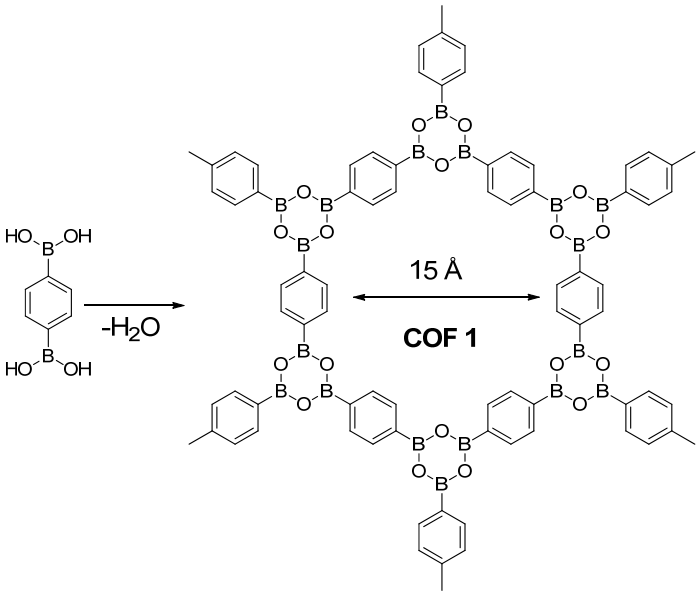

Figure 2. Condensation reaction of diboronic acid used to produce *COF-1*.[41]

Hypercrosslinked polymers (HCPs) are joined together using irreversible, kinetically controlled reaction. A large amount of excess free volume can be captured by their formation in a solvent-swollen polymer gel. The subsequent removal of the solvent results in microporous materials. The most investigated class of those polymers are hypercrosslinked polystyrenes, which are prepared from lightly crosslinked polystyrene beads via extensive cross-linking in a solvent-swollen state. A typical reaction pathway is shown in Figure 3. The micropore formation in such polymers can be attributed to the template effect of the

solvent molecules. In addition to this, there are also phase-separation induced mesopores present. Their amount can be increased by using thermodynamically poor solvent like hexane during the cross-linking reaction. The hypercrosslinked polymers have found applications as adsorbents of organic vapours and organic contaminants from water as well as substrates for chromatography.[6]

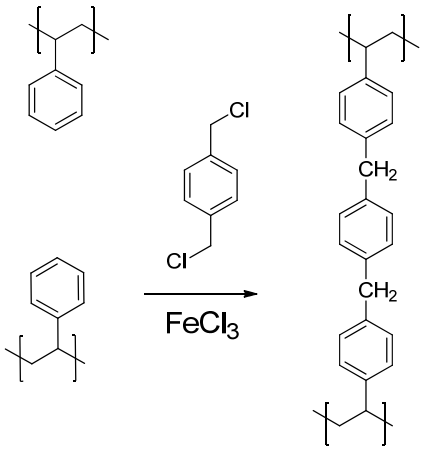

Figure 3. The synthesis of hypercrosslinked polystyrene via Friedel-Crafts alkylation.

Recently there has been an immense interest towards amorphous organic microporous polymers with so-called intrinsic microporosity, PIMs.[3] PIMs were firstly introduced by *Budd* and *McKeown* in 2004.[8] The soluble *PIM-1* prepared via aromatic nucleophilic substitution from a spiro-functionalised monomer and a fluorine-containing compound is displayed in Figure 4.

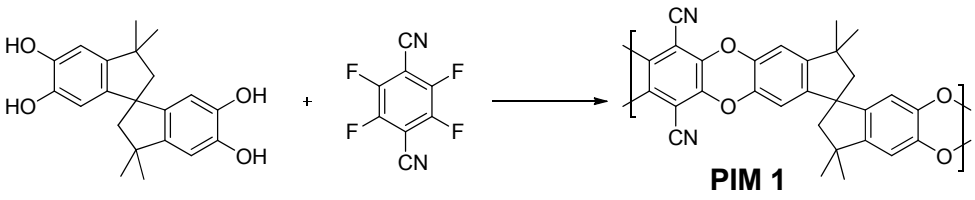

Figure 4. Reaction scheme of the synthesis of *PIM-1*.[8]

For the first time it was demonstrated that a network of covalent bonds is not a prerequisite for a microporous organic material. Due to the rigid and contorted molecular structure of the monomers, the polymers simply cannot fill the space efficiently, resulting in processable microporous organic polymers with high specific surface areas as measured by nitrogen sorption (S_{BET}(*PIM-1*) = 720-780 $m^2 \cdot g^{-1}$).

PIMs can be synthesised as soluble polymers (e.g. *PIM-1*) or insoluble network polymers, when using monomers with functionality $f > 2$. For such potential application as a gas separation membrane, a processable soluble material is certainly desired. For example, a cast film of *PIM-1* has demonstrated promising selectivities for gas pairs O_2/N_2 and CO_2/CH_4.[15] Polyimides are also favoured for separation applications.[47] Polyimides in general are high-performance materials with good thermal and mechanical stability.[48] They have also been synthesised from contorted monomers to yield polymers with intrinsic microporosity.[49–51]

2.2 Renewable resources and polymers

In a world of increasing emissions of greenhouse gases, depleting fossil oil reserves and skyrocketing petrol prices it is evident that utilising renewable resources is a well-acknowledged necessity. Renewable resources often bring along other benefits like built-in design for degradation and lower toxicity of the resulting product.[18] The application of renewable resources is not a novelty in the industry. Some of the most prominent examples include plant oil and polysaccharides. Enormous amount of effort is directed towards the utilisation of biomass.[52,53] Products derived from renewable resources include pharmaceuticals, coatings, paints, packaging materials, etc. In Germany alone ca. 3.6 million tons of renewable resources have been consumed in 2008 with 30% of these being plant oils.[54] Plant oils have been known for decades, e.g. Linoleum has been produced since the end of 19th century from its basic

component, linseed oil.[55] Narrowing natural resources down to renewable polymers, one can divide them into two groups: unmodified and chemically modified polymers. Abundant cellulose, chitin and starch belong to the former group. Esterifications of cellulose, surface modification and derivation of chitosan, lignin and suberin have been immensely developed due to their ubiquity and hence broad potential.[18,19] The latter group includes uncountable number of both natural polymers which have been chemically modified and polymers derived from natural monomers. The natural monomers, which have been extensively utilised for polymerisations, include furans, terpenes and lactic acid. Some polymers, such as polyhydroxybutyrate (PHB), are produced by microorganisms. Polylactic acid can be synthesised via a dilactid route or by bacterial fermentation. Both of them are biocompatible biodegradable polymers which are of immense interest in medicine and also for the packaging industry.[56,57]

Much less attention has been dedicated to polymerisation of terpenes and particularly of already mentioned betulin. Betulin (lup-20(29)-ene-3β,28-diol) is a naturally occurring triterpene, see Figure 5. Its content in birch bark can be as high as ca. 30% depending on the birch species. Betulin can be easily extracted with common organic solvents. Betulin is always accompanied by lupeol and betulinic acid, present in much smaller amounts. First publications on potential use of betulin have emerged in the early 1980s in Russia and Finland, countries with high population of birch trees and their wide use in the wood industry.[22–24]

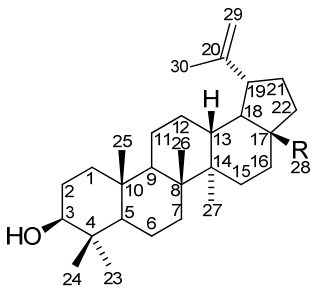

Figure 5. Chemical structure of betulin (R = CH_2OH), lupeol (R = CH_3) and betulinic acid (R = COOH).

There are many theraupeutical substances and cosmetics based on betulin and its derivatives. The rising interest towards betulin and its derivatives in medicine is provoked by their biological activity. It has been shown that betulin derivatives exhibit antiseptic, anti-inflammatory, anticarcinogenic and antioxidant activities.[58–63] Several studies have been convicted to explore their anti-HIV activity.[64–66] Due to the fact that birch bark is a large-scale byproduct of the wood industry, the enormous potential of betulin-based chemicals is clearly evident.

Apart from pharmaceutical uses of birch bark extract, there have been attempts to synthesise polyesters with commercially available terephthaloyl-, maleic and adipic acid derivatives.[67,68] Polycondensation in melt resulted in molar masses of ca. $2 \cdot 10^4$ g·mol^{-1}. Reaction in solvent with maleic acid dichloride yielded thermally curable polyesters with molecular weights up to $2.5 \cdot 10^3$ g·mol^{-1}. It was also found that the reactivity of the primary hydroxyl group was four times higher comparing to the secondary hydroxyl group. Moreover, it was declared that the reactivity of the third functional group, the double bond, is almost non-existent under applied moderate reaction conditions. To my best knowledge, no reports on direct betulin polymerisation via double bond have been published. Nor are there known publications on thorough investigations of betulin-based polymers containing micropores.

It is straightforward that betulin, as a monomer diol, can be e.g polymerised to polyurethanes or polyesters in a polyaddition and a polycondensation reaction, respectively. For industrial applications of the former it is, however, common to use macromer diols, thus being able to tailor the desired material properties.[69] As for the latter, one of the most famous industrial polyesters is certainly polyethylene terephthalate (PET), which is synthesised via transesterification of dimethyl terephthalate with ethylene glycol. Generally it is rather profitable from the economical point of view to let a diol and a diacid to react in a polycondensation reaction. Equimolar amounts of reactant, a catalyst and a constant removal of resulting low molecular condensate (e.g. water, methanol,

etc.) are required to reach good conversions and higher molecular weights in a polyesterification reaction.[70,71] As growing chains contain hydroxyl and acid groups, transesterifications are taking place throughout the reaction, resulting in medium molecular weight distributions, which can be calculated using the Schulz-Flory method.[72] The properties of the polyesters are largely dependent on the presence of terminal hydroxyl groups, i.e. they can react as dialcohols and for example be used in a subsequent synthesis of polyurethanes. The ester linkage of polyesters can be rather easily hydrolysed. The resistance to hydrolysis is a function of polyester structure, and it increases with the hydrophobic character of the utilised monomers and decreasing number of ester linkages.[69] Aromatic polyesters are usually more hydrolysis-resistant due to the steric reasons.

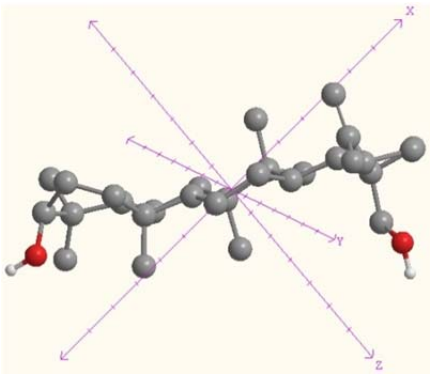

Figure 6. 3D-representation of betulin molecule with a view axis. Apolar hydrogen atoms are omitted for clarity.

Betulin is a suitable renewable monomer for formation of polymers with intrinsic microporosity. It has two reactive hydroxyl groups in sterically fixed positions due to the contorted structure of the fused betulin rings, see Figure 6.

This rigid structure should act as an appropriate basis to generate a microporous polymer.

3 Methods

A number of methods have been established for characterising porous media. Usually, a combination of several of them is needed to understand how molecular structure influences the pore structure, i.e. the properties of a microporous polymer. A variety of methods is being employed to investigate microporous materials, such as small-angle X-ray scattering (SAXS), positron annihilation lifetime spectroscopy (PALS), computational techniques, gas adsorption and ^{129}Xe-NMR. The most appropriate for this work, the latter two, will be discussed in more detail.

3.1 Gas Sorption

Adsorption is a process of enrichment of one component at the interface. The substance being adsorbed to the adsorbent (substrate) is called adsorbate. The reverse process is called desorption.[73] The coverage θ is defined as the fraction of occupied adsorbed sites, equation (3-1):

$$\theta = \frac{number\ of\ occupied\ sites}{total\ number\ number\ of\ sites} \qquad (3\text{-}1)$$

Considering the strength of the interactions between the adsorbate and the substrate, there are two types of possible processes: physisorption and chemisorption. The former is characterised by weak van-der-Waals forces. The enthalpy of adsorption lies in the same dimension as the enthalpy of condensation. This small amount of energy can be easily absorbed by the substrate as heat. The enthalpy of physisorption can be calculated by measuring the temperature elevation during adsorption by a sample with known heat capacity. Typical values are in the range of −10 to −20 kJ·mol^{-1}. On the contrary, typical values for chemisorption are ca. −200 kJ·mol^{-1}. A true chemical bond,

mostly a covalent bond, is established between the surface and the particle during chemisorption.

There are several techniques which provide a way to determine the amount of adsorbed gas. They all can be divided into two groups: gravimetric and volumetric. In the first case the amount of gas adsorbed is directly measured by weighing the sample prior and upon the adsorption. The recent developments in vacuum microbalance methods have revived this technology. Gravimetric methods are especially preferred for high-pressure adsorption applications. However, the volumetric methods are more popular and routinised. They are discussed below in more detail.

In a standard static volumetric method a known quantity of gas is admitted to a confined volume, which contains adsorbent at a given temperature. After the adsorption has taken place, the amount adsorbed is calculated as the difference between the amount of gas admitted and the amount of gas required to fill the volume, the *dead space*, at the equilibrium pressure. The adsorptive is admitted in charges and the isotherm is thus recorded point-by-point. The volume of the dead space should be determined thoroughly prior to measurement. Usually, this is done by admission of a gas with negligible adsorption capacity, e.g. helium. It can, however, be pre-calibrated, subtracting the volume occupied by the adsorbent, which is not very convenient for routine measurements.

It should be noted that in this work, the term “gas sorption” is used as a synonym to “gas adsorption-desorption”, i.e. it is definitely related to adsorption as a process of enrichment of one component at the interface and not absorption, which is the process of enrichment of one component within the material.

Classification of adsorption isotherms

The IUPAC differentiates six common types of isotherms, see Figure 7.[27] The reversible *Type I* isotherm is common for microporous solids with relatively small external surface areas, like activated carbons and molecular sieve zeolites. The gas uptake is aiming a plateau at $p/p_0 \rightarrow 1$ due to complete micropore filling. The

reversible *Type II* isotherm is typical for non-porous or macroporous materials with unrestricted monolayer-multilayer adsorption. Point *B* indicates the completion of monolayer coverage and the beginning of multilayer adsorption. The convex reversible *Type III* isotherm is rather uncommon, although it is characteristic for some particular systems like nitrogen on polyethylene. The predominant adsorbate-adsorbate interactions give rise to this type of isotherm. The *Type IV* isotherm is exemplary for mesoporous adsorbents. Starting like the *Type II* isotherm, it reveals a hysteresis loop upon desorption, which is associated with capillary condensation proceeding in mesopores. It also features a limiting uptake at $p/p_0 \rightarrow 1$. The *Type V* isotherm is uncommon and is related to weak adsorbent-adsorbate interactions like *Type III*. The *Type VI* isotherm demonstrates stepwise multilayer adsorption on a uniform non-porous surface with each step height representing a monolayer capacity for each adsorbed layer. Such isotherms are generally obtained with argon or krypton on graphitised carbon black at liquid nitrogen temperature.

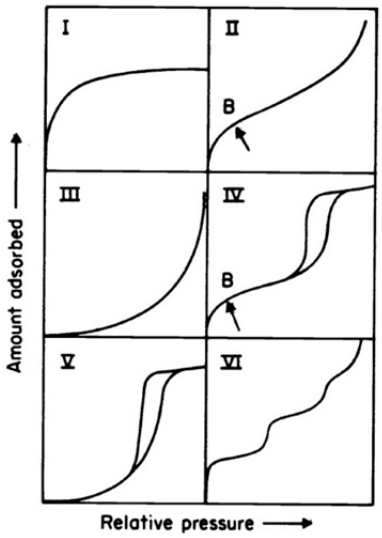

Figure 7. Types of isotherms. Reprinted from reference [27].

The frequently observed hysteresis upon desorption at higher p/p_0 values is generally associated with capillary condensation in mesopores structures. Many

systems, however, exhibit so called *low pressure hysteresis*. This phenomenon has been reported for microporous carbons[74], zeolites[75], non-crosslinked polymers[33,49,50] and microporous polymer networks[51,76]. It is commonly present in microporous polymers and is usually indicating the swelling of a non-rigid porous structure. However, it can also be induced by irreversible gas adsorption through pore necks of similar size like the adsorbate molecules or even by irreversible chemical adsorbent-adsorbate interactions.

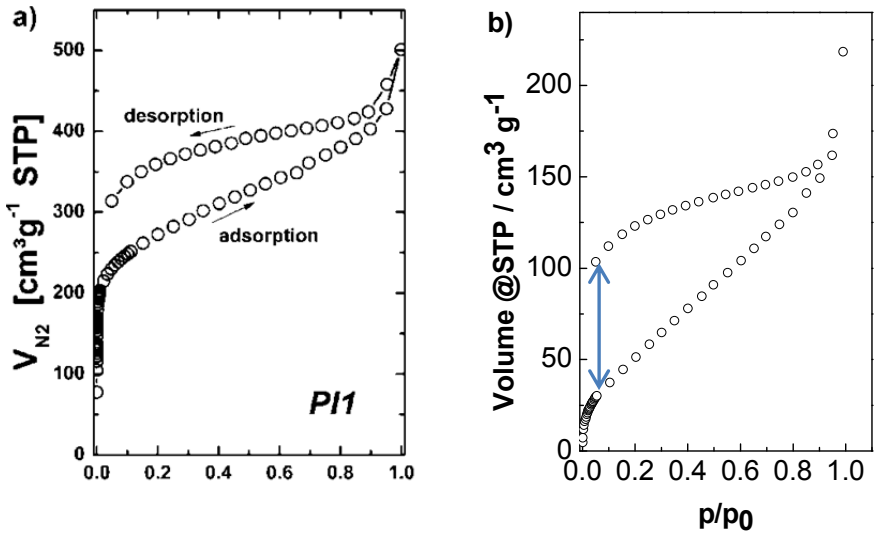

Figure 8. Low pressure hysteresis of nitrogen adsorption isotherms, reported in (a) non-crosslinked polyimide (reprinted from [51]) and (b) betulin-based polyester networks presented in this work. The arrow is depicted for the emphasis.

An example of low-pressure hysteresis with desorption branch of the isotherm not closing at low p/p_0 (< 0.05) is given in Figure 8.

BET method and surface area

The Brunauer-Emmet-Teller method for the determination of the specific surface area from the gas adsorption measurements has become the most commonly used procedure, in spite of oversimplified assumptions of the model on which the theory is based. The assumptions are:

1. Adsorption occurs only at well-defined adsorption sites.

2. The only molecular interaction takes place when an already adsorbed gas molecule acts like a substrate for another one.
3. The molecules of the upper layer are in equilibrium with the gas phase.
4. Desorption is a kinetically limited process. The heat of sorption is the same for each molecular layer. For the first layer it is the heat of sorption at the solid sample surface. The other layers are assumed to be similar and thus can be represented as a condensed phase with the heat of sorption equal to the heat of liquefaction.
5. The molecule layer number tends to infinity at the saturation pressure.

The BET equation is usually written in linear form:

$$\frac{p}{n^a \cdot (p_0 - p)} = \frac{1}{n_m^a \cdot C} + \frac{(C-1)}{n_m^a \cdot C}\frac{p}{p_0} \qquad (3\text{-}2)$$

where n^a is the amount adsorbed at the relative pressure p/p_0 and n_m^a is the monolayer capacity. This equation requires linear relation between $p/n^a(p - p_0)$ and p/p_0. The linearity is usually provided in low p/p_0region of ca. 0.05-0.25. Only at this region close to monolayer coverage the BET plot can deliver the true value of n_m^a.[77] However, this region can be shifted to lower relative pressure when the surface of the adsorbent is homogenous and consequently the system displays high absolute adsorption energies, e.g. nitrogen on graphitised carbon.

Applying the BET method allows the calculation of the surface area from the monolayer capacity. This is only achievable with the knowledge of the molecular cross-sectional area s_m, the area occupied by the adsorbate molecule in the complete monolayer. Hence,

$$S(BET) = n_m^a \cdot N_A \cdot s_m \qquad (3\text{-}3)$$

and

$$s(BET) = \frac{S(BET)}{m} \qquad (3\text{-}4)$$

where *S(BET)* and *s(BET)* are the total and specific surface areas, respectively. N_A is the Avogadro constant, *m* is the mass of the adsorbate and s_m = 0.162 nm^2 for N_2 at 77 K.

The complete assessment of microporosity is, however, not straightforward. The models developed for analysing mesopores cannot be directly transferred to give a complete viable image of the micropore structure. Due to the very small pores (molecular dimension), the mechanism of physisorption is altered because the close proximity of the pore walls gives rise to strengthened adsorbent-adsorbate interactions. As a result of the enhanced adsorption, the pore filling occurs at low p/p_0, which indicates that the adsorbent is microporous. The limiting dimensions of micropore filling are difficult to specify, but this process should be differentiated from the secondary process of capillary condensation in mesopores. It is believed that there are two different micropore filling mechanisms taking place below the onset of capillary condensation: the first one is the entering of the adsorbate molecules into the very narrow pores at low p/p_0 and the second one is happening at somewhat higher p/p_0 and is a cooperative process involving adsorbate-adsorbate interactions. Discussions about the interpretations of the experimentally achieved isotherms have been arising while investigating microporous materials. According to classical Langmuir theory, the limiting adsorption (the plateau) of the *Type I* isotherm designates the monolayer completion, and can therefore be used for the calculation of the surface area. With the concept of micropore filling widely spread nowadays, it is believed that the initial steep part of the isotherm belongs exactly to this process, so that the plateau originates from the multilayer adsorption on the small external area. In this case the value of *S(BET)* cannot be accepted as the true value of surface area for a microporous material. The overlap of micropore filling and multilayer formation invalidate the assumption of the BET theory that

adsorption takes place by multilayer formation and that the number of adsorbed layers is infinite at the saturation pressure, i.e. adsorption occurs as if on a free surface. Hence, the BET surface area provides a rough estimate for comparing different materials but does not propose meaningful results on an absolute scale. Nevertheless, the BET method has been proven to be suitable to analyse microporous MOFs, yielding calculated BET areas which agree well with the experimental data.[77] Although the surface of MOFs is far from flat and the adsorption can happen via pore filling, it has been shown that the simulated isotherms agreed well with the accessible surface areas calculated directly from crystal structures in a geometric fashion. It was also pointed out that the best results are obtained by applying the BET theory over the proper pressure region and not in a common range of p/p_0 of 0.05 – 0.3, with the implicit assumption that monolayer formation occurs in this pressure range. The structure of the materials presented in this work is not similar to that of the MOFs, yet a report of good applicability of the BET model to microporous materials, is promising for the first assessment of microporosity.

Pore size distribution

The gas sorption behaviour in smaller micropores is almost entirely governed by the interactions between fluid molecules and the pore wall.[78] The adsorption occurs via multilayer formation or pore filling mechanism. By contrast, in mesopores both attractive fluid-wall and fluid-fluid interactions play the leading role. The resulting pore condensation is characteristic for mesopores.

The macroscopic thermodynamic considerations of methods based on Kelvin equation (e.g. BJH-method; Barrett, Joyner, Halenda) are only appropriate for analysis of mesoporous materials. They fail completely to describe pore filling of micropores in a correct way. Other methods, like the semiempirical HK-method (Horvath and Kawazoe), is only valid for micropore filling and cannot be applied for mesopores size analysis. It assumes that all pores of a certain size will fill at a

particular relative pressure, which is related to the fluid-solid interaction energy and the effective pore radius.

DFT (Density Functional Theory) methods have been established to provide description of pore size distribution in materials containing both micro- and mesopores. In narrow pores, where attractive fluid-wall interactions become dominant and the concept of a smooth liquid-vapour interface and bulk-like core fluid cannot be applied, DFT and molecular simulations (Monte Carlo and Molecular Dynamics) deliver more accurate results. NLDFT (Non-Local Density Functional Theory) models are widely employed for theoretical predictions of adsorption isotherms in nanoporous materials and are implemented in commercial adsorption instruments.[79] However, NLDFT models assume smooth and homogenous pore walls and do not take into account the effects of surface roughness and heterogeneity explicitly. The models are effectively one-dimensional, since the solid-fluid potential and the fluid density vary only in the direction normal to the pore wall. The consequence of this simplification is that it induces strong layering in the adsorbed phase, causing artificial steps of adsorption isotherms in the region of multilayer adsorption. This layering gives rise to prominent artificial gaps in pore size distribution (e.g. in graphite at 77 K where monolayer transition occurs at the same pressure as the pore filling in a ~1 nm slit pore).[80]

In contrast to NLDFT models assuming flat graphitic pore walls, the QSDFT (Quenched Solid Density Functional Theory) method takes into account the surface roughness and heterogeneity. Suggested by *Ravikovitch* and *Neimark* in 2006[80], it has now been extended and commercialised by *Quantachrome*. In this approach a multi-component DFT is used, in which the solid is treated as one of the components with a fixed spatially distributed density. The solid atoms are represented as quenched component(s) of the solid-fluid system, with given density distribution(s), rather than the source of the external potential. The fluid is an “annealed” component. Solid-fluid intermolecular interactions are split into hard-sphere repulsive and mean-field attractive parts. The corresponding

parameters are determined from the fit of the reference experimental adsorption isotherms on graphitised and non-graphitised carbon blacks. The fluid-fluid parameters are determined to reproduce bulk thermodynamic equilibria of nitrogen at low temperatures. The main strength of this method is the description of the surface roughness.

CO_2 sorption

The sorption of nitrogen and argon at 77 K is most widely used for the investigations of the mesoporous materials and has been studied in sufficient detail. The study of the pore structure of ultramicropores is, however, associated with a number of problems. The application of the BET model has been questioned because of the frequently occurring activated diffusion phenomenon of the N_2 and Ar molecules into the volume of ultrafine pores at 77 K.[81,82] It leads to the incomplete filling of the pores, so that the resulting information on the microstructure parameters of the nanoporous material becomes unreliable, e.g. the *S(BET)* derived from nitrogen sorption is thus underestimated. There are two possible ways to overcome this drawback. One way includes the deployment of adsorbate with smaller critical molecular sizes, e.g. H_2 (σ_k = 0.289 nm as compared with σ_k = 0.364 nm for N_2). The other way is to conduct the measurement at higher temperature to increase the kinetic energy of adsorbate molecules to alleviate diffusion into the volume of ultrafine pores. CO_2 with σ_k = 0.33 nm can be used for this purpose (mostly at 195 K and 273 K). It has been used at different temperatures of 195 K, 298 K and 273 K since 1964.[83,84] At 273 K, CO_2 is 32 K below its critical temperature and has a high saturation pressure, which is why the relative pressure necessary for the micropores analysis is achieved at lower absolute pressure. Besides, the diffusion rate is also higher so that equilibrium is reached faster. However it should be taken into account that the large quadrupole moment of CO_2 (in comparison with N_2) would lead to preferable interactions with polar groups of the adsorbent. In polymers, CO_2 can even lead to plasticisation effects under high pressure (> 10 bars, dependent on polymer and experimental conditions).[85–88] It has also been

reported that the BET surface area alone measured by nitrogen sorption at 77 K does not necessarily correlate with the CO_2 uptake capacity at 1 bar and 273 K. For a series of aromatic polymers the highest CO_2 uptake was registered in those containing electron-rich triazole units in the network and not in those displaying the largest BET surface area.[89] For some metal organic frameworks, *MOFs*, it was even theoretically predicted (using Grand Canonical Monte Carlo method) that materials with carboxylic acid groups would exhibit stronger interactions with CO_2 gas, consequently having higher isosteric heat of adsorption and thus the overall CO_2 uptake.[90] The same was experimentally observed for conjugated microporous networks (which on the contrary to MOFs are amorphous and covalently bound) with various functional groups on the aromatic benzene ring.[86] It was established that bulky non-polar groups have negative impact on CO_2 sorption. The gas uptake can be chemically enhanced via introducing polar functional groups in the order –COOH > – $(OH)_2$ > $–NH_2$ > $–(CH_3)_3$ > non-functionalised (the order of decreasing isosteric heat of adsorption).

3.2 Xe-NMR

Xenon has nine stable isotopes. Two of them, the spin ½ ^{129}Xe and spin 3/2 ^{131}Xe with natural occurrence of 26.4% and 21.2% respectively, have magnetic moments and are therefore detectable by NMR spectroscopy.[91] Based on sufficient natural abundance of the former and its magnetic moment, its receptivity comparing to ^{13}C is 31.8. Hence, the resonant absorption signal is simple to detect. The electron cloud of Xe is highly polarisable and responds sensitively to physical interactions of xenon atoms with their environment.

Fraissard et al.[92] have developed a method, which allows the estimation of pore radii in microporous materials. This technique has evolved into a powerful tool for analysing porous solids.[91–97] Furthermore, it has been applied for the characterisation of microporous polymers.[98,99] It has been shown that the

chemical shift δ_S is related to the size and the shape of the pore.[91,92,100–102] The smaller the pore, the more difficult is the diffusion, i.e. the impact of the environment on the xenon atoms is higher. This results in larger value of δ_S. The mean free path *l* of xenon was calculated for various known zeolites. The correlation between *l* and δ_S was thus introduced, providing an opportunity to determine any void dimensions in any material where xenon can be adsorbed.[103]

The observed chemical shift of xenon adsorbed in a porous solid consists of several contributions corresponding to various interactions,

$$\delta = \delta_0 + \delta_S + \delta_{Xe} + \delta_{SAS} + \delta_E + \delta_M \qquad (3.5)$$

where δ_0 is the reference shift, δ_S is reflecting the interactions of xenon with the surface, δ_{Xe} arising from Xe-Xe interaction by increasing xenon pressure, δ_{SAS} coming from specific interactions with strong adsorption sites, and the latter two corresponding to electric and magnetic fields. The chemical shift of xenon adsorbed in pores and extrapolated to zero concentration depends only on the internal void space of the material. In the materials presented in this work, mainly δ_S and δ_{Xe} can be assigned to significantly contribute to the observed signal, simplifying the data analysis.

As a rule, the observed chemical shift is plotted against the xenon pressure and extrapolated to zero. From an empirical relation between δ and λ,[104]

$$\delta = 499.1/(2.054 + \lambda) \qquad (3.6)$$

the mean free path λ and thus the diameter of the pore can be calculated.

$$D_{sp} = 2\lambda + D_{Xe} \qquad (3.7)$$

$$D_{cy} = \lambda + D_{Xe} \quad (3.8)$$

The mentioned equations (3.7) and (3.8) enable deducing the diameter of a spherical and cylindrical pore, respectively.

Xe-NMR is both chosen as an elegant method for its applicability, as well as it adds to a complete investigation of microporous polymers presented in this work.

4 Results and Discussions

4.1 Microporous polyester networks

4.1.1 Introduction

Betulin, presented in Chapter 2.2, is the main component of birch bark and hence a renewable resource. Its stiff structure of fused six- and five-membered rings along with its two reactive hydroxyl groups make betulin a perfect starting compound for polymer synthesis. Commercial betulin with 98% purity is available from *Sigma Aldrich*. The study was initiated with commercial betulin and further continued with betulin extracted from the birch bark.

The group of polymers with intrinsic microporosity introduced in Chapter 2.1 includes primarily aromatic dioxane-linked polymers, polyimides, poly(benzimidazoles), etc. Yet there are no known microporous polyesters with thorough studies on their microstructure. To my best knowledge, the only known microporous polyesters are cured films of hyperbranched polyarylates based on tetrakis(4-carboxyphenyl)silane, which have an apparent BET surface area of 158 $m^2 \cdot g^{-1}$.[105] No other microporosity investigations were conducted on those, apart from a standard N_2 adsorption at 77 K.

The ester linkage permits more rotational freedom than stiff amide or dioxane linkages or an all-aromatic backbone. Therefore it can be considered “softer” and it would be insufficient to build up a polymer with kinked and/or twisted backbone geometry, which is a prerequisite for a polymer with intrinsic microporosity. Even the utilisation of a sterically contorted monomer would probably be not enough. Thus, it is straightforward to attempt to prepare crosslinked polyesters. The simplest way to do so is to employ appropriate monomers with functionality greater than two. With betulin being an A_2 monomer, one can think of a B_3 comonomer with acid functionalities for the formation of a crosslinked polyester. Polyester networks from betulin were synthesised using 1,3,5-benzenetricarbonyl trichloride in THF with pyridine as a

base, see Figure 9. Freeze-drying resulted in considerable nitrogen uptake, see Figure 10. Therefore, a microporous polyester consisting of ca. 78 wt.% (ideal composition) renewable resource has been successfully synthesised.

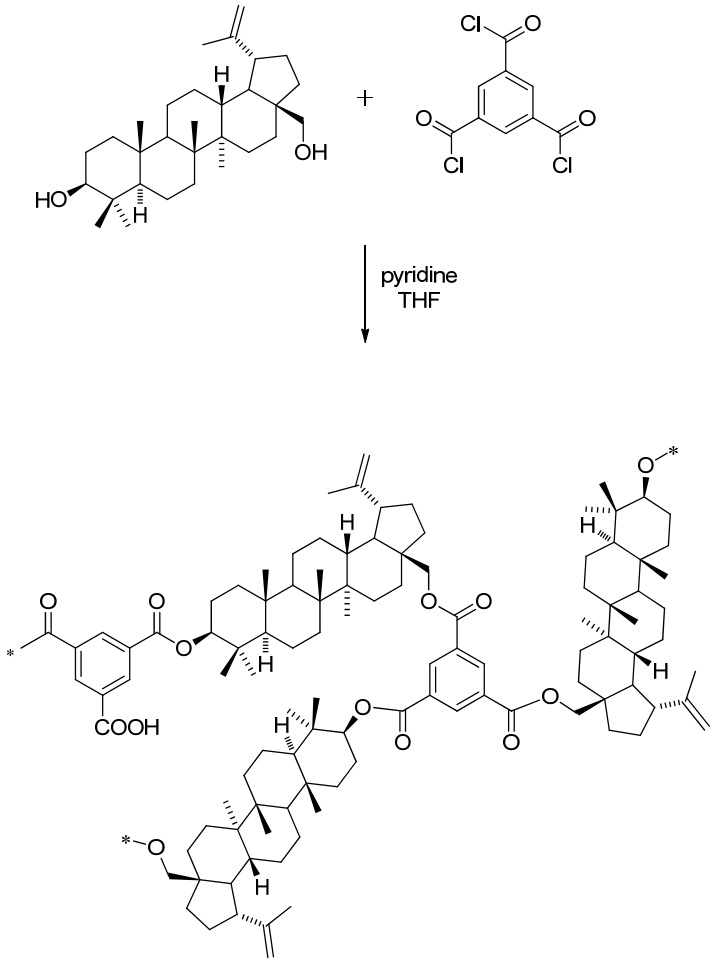

Figure 9. Reaction scheme for the synthesis of a polyester network from betulin and 1,3,5-benzenetricarbonyl trichloride. The structure of the product represents one of the possible linkages and not the repeating unit.

The solid state ^{13}C-NMR provided proof of ester bond formation, see the signal at δ = 164 ppm in Figure 11. Eventually present acid carbonyl groups did not produce any detectable signal.

The prepared polyester network turned out to be stable in inert conditions at 100 °C for 48h. The microstructure seemed to be practically unaffected by

thermal treatment, since the nitrogen isotherm displayed similar quantitative and qualitative behaviour, see Figure 10. The change is within the typical error-range of the applied method.

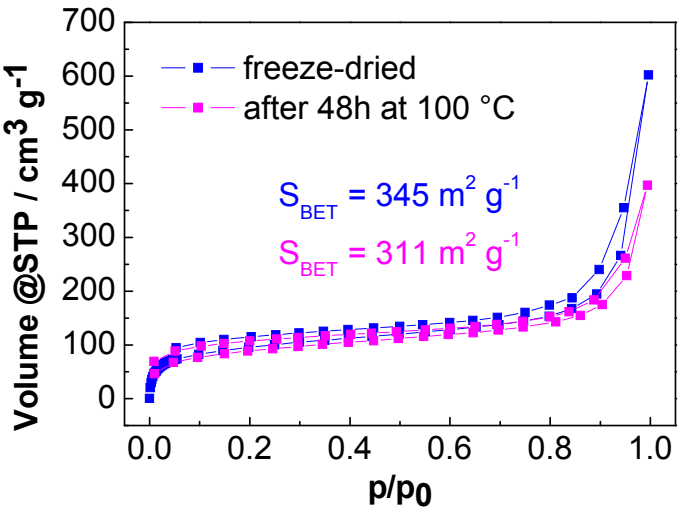

Figure 10. Nitrogen adsorption isotherms collected at 77 K for a freeze-dried sample (blue) and the same sample after being heated in an inert atmosphere at 100 °C for 48h (magenta).

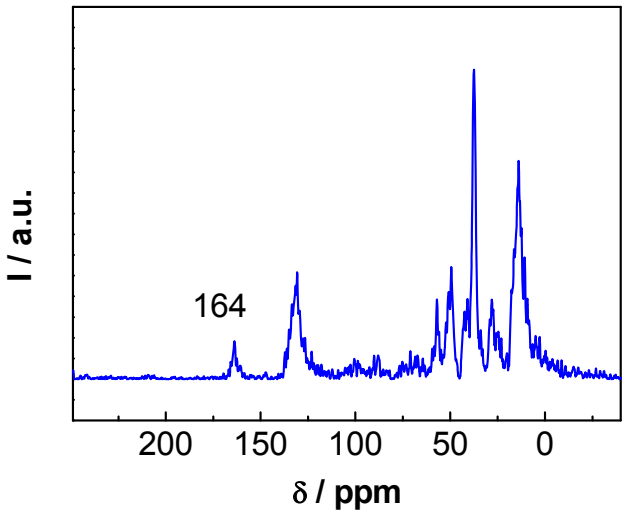

Figure 11. Solid state ^{13}C-NMR of the polyester network.

After having successfully synthesised the microporous polyester network from commercial betulin, the influence of various factors on the product characteristics has been investigated in more detail with the birch bark extract.

Betulin can be extracted via sublimation or extraction with various solvents like ethanol, chloroform, diethyl ether, butanol-water azeotrope, etc.[58,106,107] Methylene chloride was chosen because of the low extraction temperature and high yields of betulin (Figure 12).

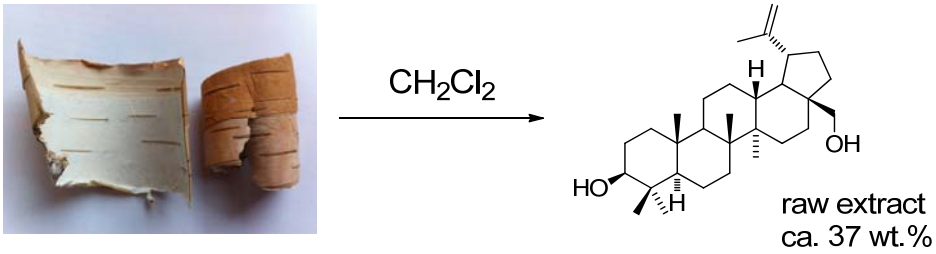

Figure 12. Scheme of betulin extraction from birch bark.

Yellowish extract bark of *Betula pendula* was subsequently recrystallised from ethanol to give a white powder with slight yellow stain. For some experiments it was even found that no extra purification steps were needed, and the crude extract could be used as collected.[108] The properties of resulting products were practically unaffected.

The FTIR spectra of commercial betulin and the crude extract are comparable, differing only in appearance of two extra shoulders at ca. 1707 cm^{-1} and 1246 cm^{-1} in the latter. These bands can be assigned to carbonyl and ether groups' oscillations of betulinic acid and/or betulinic aldehyde respectively, both present in birch bark extract, see Figure 13a.[109]

After the reaction with 1,3,5-benzenetricarbonyl trichloride, the resulting polymer was dried to form a powder with a slight yellowish stain. The network from commercially available betulin was an off-white powder. Nevertheless, the analytical data displayed the alikeness of both types of networks, i.e. the

presence of other compounds in the crude extract did not seem to drastically influence the formation and the physical properties of the resulting polymer. In fact, the FTIR spectrum of the network synthesised from the crude extract copies exactly the one from the commercially available betulin (Figure 13b).

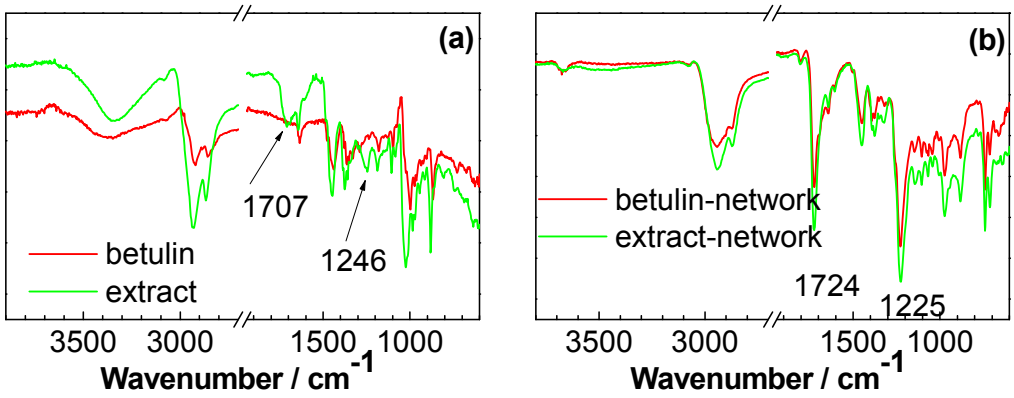

Figure 13. (a) FTIR spectra of crude birch bark extract (green) and commercially available (Sigma Aldrich, 98%) betulin (red); (b) FTIR spectra of the networks, respectively.

The ester formation is confirmed by the appearance of the carbonyl band at 1724 cm^{-1}, C-O oscillation at 1225 cm^{-1} and the disappearance of the broad hydroxyl band at ca. 3350 cm^{-1}.

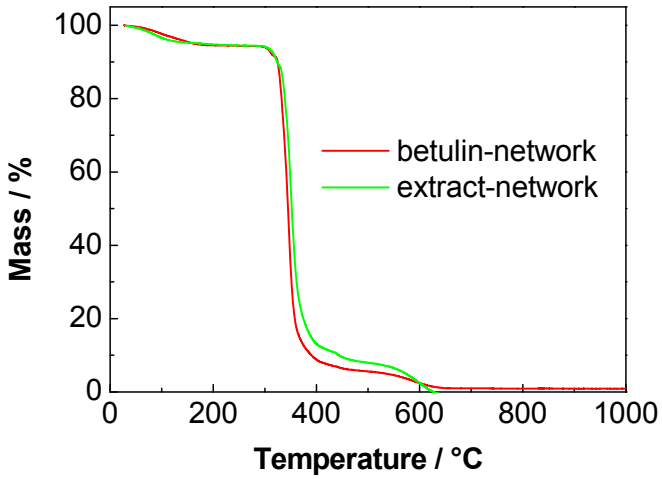

Figure 14. TGA plot of networks made from commercially available betulin (red) and crude extract (green), measured in nitrogen flow.

The thermal stability was investigated by means of thermogravimetric analysis (TGA), see Figure 14. It showed that both networks are stable up to ca. 300 °C under nitrogen.

After the above mentioned promising data on the successful preparation of thermally stable microporous polyester networks with high renewable resource content, the impact of various factors on the polymerisation reaction was investigated.

The concentration of reactants proved to be essential for the formation of the desired insoluble network. Depending on the reaction conditions, this A_2+B_3 reaction yielded hyperbranched soluble polymers (discussed in Chapter 4.2: "Soluble polymers from betulin"). An overview of selected experiments is presented in Table 4-1.

Table 4-1. An overview of selected experiments of polyester networks (N1-N9) synthesis. *Py* denotes pyridine, *BTC* - 1,3,5-benzenetricarbonyl trichloride. Concentrations are given with respect to betulin in [M] = mol/L. *Betulin-ethanol solvate used.

	$n_{Bet.}$/ mmol	Bet./BTC/ eq	THF/ mL	n_{Py}/ mmol	Py/ eq	V_{Py}/ mL	c_{THF}/ M	c_{all}/ M	gel	S_{BET}/ $m^2 \cdot g^{-1}$
N1	2.2	1.57	30	24.7	11.23	1.99	0.073	0.069	yes	390
N2	1.13	1.49	15	12.3	10.88	0.99	0.075	0.071	yes	380
N3	3.3	1.57	45	37	11.21	2.99	0.073	0.069	yes	350
N4	1.13	1.49	9	12.3	10.88	0.99	0.126	0.113	yes	350
N5	1.13	1.49	90	12.3	10.88	0.99	0.013	0.012	no	
N6	1.1	1.57	15	2.5	2.27	0.20	0.073	0.072	yes	
N7	1.1	1.58	15	7	6.36	0.57	0.073	0.071	yes	420
N8	1.1*	1.58	15	6.96	6.33	0.56	0.073	0.071	no	
N9	1.1*	1.57	15	6.9	6.27	0.56	0.073	0.071	no	

The impact of the reactant concentration was investigated with a 3:2 stoichiometry between betulin and 1,3,5-benzenetricarbonyl trichloride, i.e. the exact stoichiometry between the functional groups. It turned out that the

reaction was sensitive to the amount of pyridine. A stoichiometric amount of the base needed to capture the forming hydrochloric acid was not sufficient to provide high network yields. Thus, the reactions were performed in a mixed (THF/pyridine) solvent. Consequently, the pyridine content was kept fixed (11 eq with respect to betulin), and only the amount of THF was modified (pale green entries in Table 4-1). At a betulin concentration of 0.013 M (with regard to THF; *N5*) almost no gel was formed. The isolated sol was analysed by GPC to give a weight average molecular weight of M_w = 7000 g mol^{-1} and a polydispersity of 1.9. Increasing the concentration to 0.073 M (*N3*) resulted in formation of polymer networks with yields ranging from 75% to 90%. A further increase in concentration up to 0.126 M (*N4*) did not result in a significant increase in gel yield or specific surface area.

It was also revealed that the amount of pyridine used contributed to higher conversions and higher yields of the network (yellow entries in Table 4-1). The pyridine content was altered from very slight excess to large excess with betulin concentration remaining constant (0.073 M with respect to THF). Although an excess of pyridine was used in all cases, it was established that slight excess was insufficient and hence a significant excess of the substance was essential to form a large fraction of gel. Using 1.13 eq of pyridine (with respect to functional groups; *N6*) resulted in moderate yield of 50% and the gel showed no microporosity. Surprisingly, the sol fraction had a rather low molecular weight of M_w = 5500 g mol^{-1}. Raising the amount to 3.2 eq (per functional group; *N7*) increased the yield up to 75%. However, a larger excess of pyridine (5.6 eq per functional group; *N1*) was required to achieve higher yields between 80% and 90%. It should be noted that the use of triethylamine was tested but comparing to pyridine, it rather impaired the yield. This is why it was excluded from further investigations. Similar findings were reported for kinetic investigations of the reactivity of the hydroxyl groups of betulin: the rate constant does not alter much on changing the solvent in presence of triethylamine, but scales up from ca. 10^{-3} to 10^{1} on exchanging solvent to pure pyridine.[24]

Another aspect of interest of this reaction was the tolerance against a stoichiometric imbalance. It was confirmed that a slight imbalance did not result in substantive changes of the outcome, since the experiments were performed at the reaction extent greater than gel point. For example, the use of slight excess of betulin (1.6 eq instead of 1.5) resulted in networks with comparable yields and surface areas (determined by gas sorption).

4.1.2 Characterisation and discussion

After adjusting the reaction conditions, the microstructure of the polyester networks was thoroughly investigated. To gain insight to the morphology of the materials, gas adsorption techniques (nitrogen, carbon dioxide, hydrogen and argon), small angle X-ray scattering (SAXS), xenon NMR and scanning electron microscopy (SEM) measurements were employed. The comparative analysis of different networks was deliberately omitted. Instead, several large batches of one network were prepared for the detailed study of microporous structure. Comparable analytical investigations were conducted on one batch of the network in each case.

The material was expected to form stable pores due to the rigid betulin unit in the network. It was found that the drying method was also crucial for their formation. Initial investigations of the permanent porosity of the networks by means of nitrogen sorption at 77 K indicated apparent absence of micropores. However, the severe impact of the drying method on the observable porosity in nanoporous polymers has been reported in a number of recent papers.[110,111] Hereby, we have studied the impact of the drying method in more detail. After washing the reaction mixture, samples from one batch were either freeze-dried from dioxane after solvent-exchange (process A) or dried at 50 °C *in vacuo* (process B), see Figure 15.

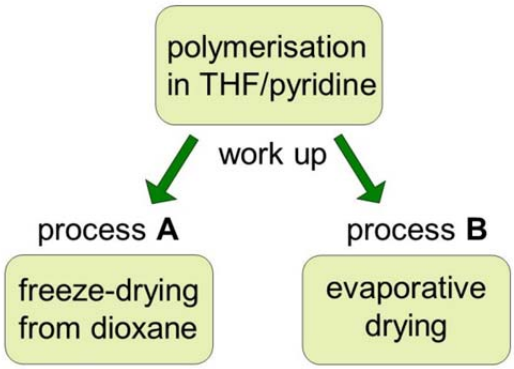

Figure 15. Scheme of the drying processes employed to the networks.

The latter process resulted in the seemingly absence of permanent microporosity and/or pore collapse as probed by nitrogen sorption at 77.3 K ($S_{BET} \approx 2$ m^2 g^{-1}). On the contrary, the freeze-drying leads to apparent BET surface areas between 250 $m^2 \cdot g^{-1}$ and 450 $m^2 \cdot g^{-1}$. The isotherms of freeze-dried materials indicate the existence of micropores (type I at $p/p_0 < 0.8$) with relative high nitrogen uptake at low p/p_0 and the presence of larger pores (meso- to macroporosity) too, see Figure 16a.

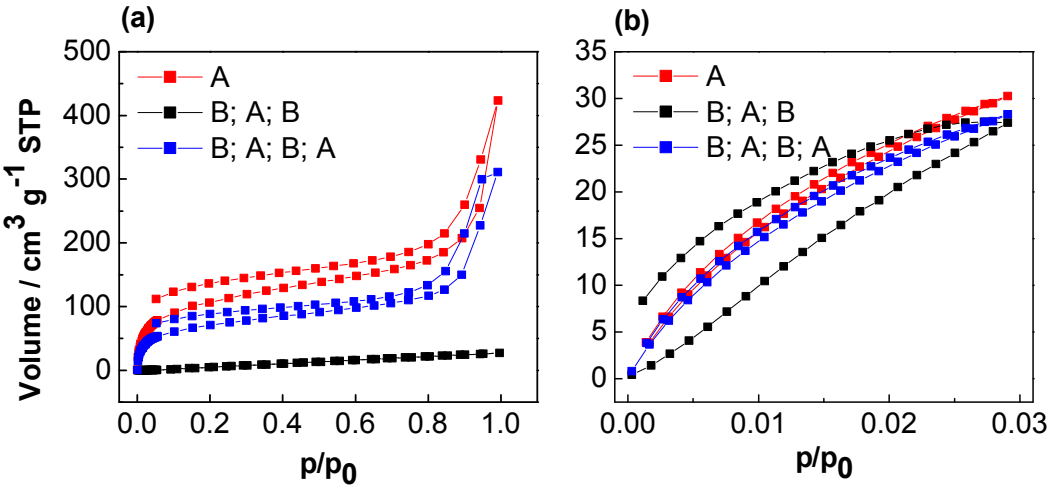

Figure 16. (a) Nitrogen sorption at 77 K; (b) CO_2 sorption at 273 K. *A* – freeze-dried from dioxane, *B* – evaporative dried.

Interestingly, reswelling of the collapsed sample in dioxane followed by freeze drying (processes B and A) resulted in recovery of the microporosity (S_{BET} = 393 m^2 g^{-1}). To ensure the reversibility, the cycle was repeated once more (B; A; B; A) and a slightly decreased surface area of S_{BET} = 257 m^2 g^{-1} was detected. This value is still within the typical range obtained by freeze drying.

A characteristic feature of all prepared microporous betulin networks is the occurrence of a low-pressure hysteresis upon nitrogen desorption (see also Figure 8 in Chapter 3.1: "Gas Sorption"). This means that not all nitrogen is released upon desorption and some of it stays entrapped in the material. This effect is commonly observed in microporous polymers and points to some flexibility of the network structure. This should be attributed to plasticisation and swelling upon nitrogen sorption or the tortuosity of the micropore structure.[3,112]

More detailed analysis of porous structures can be achieved using several adsorbates at various temperatures. By increasing the temperature, one can often overcome the energy barrier associated with the "activated entry" of molecules through constrictions of narrow pore entrances.[25] In order to analyse the microporosity of the networks in more detail, it was decided to utilise carbon dioxide sorption. This method can be used to extend the pore distribution to smaller micropore size and thus give additional valuable information.[3,112] It has been suggested that the diffusion of nitrogen at cryogenic temperatures is restricted and is therefore preventing the adsorptive from entering the narrowest pores.[113,114] However, the CO_2 adsorption analysis is usually performed at higher temperature and lower relative pressures, allowing the measurement of the narrow microporosity. As a result, these two methods supplement each other and can provide thorough information about the microporous structure. Surprisingly, a significant CO_2 uptake was registered for all samples, irrespective of the applied drying method, see Figure 16b.

The evaporative dried sample (B; A; B) revealed similar pore volume and surface areas as the freeze-dried samples, see Table 4-2. Only the form of the sorption isotherm displayed a distinction from the freeze-dried samples.

Table 4-2. Surface areas and pore volumes calculated from gas sorption experiments on samples from the same network batch (made from crude birch bark extract) which were dried in different ways (A – freeze-dried from dioxane, B – dried *in vacuo* at 40 °C).

Drying method[a]	$S_{BET}(N_2)$ / $m^2\ g^{-1}$	$V_{pore}(N_2)$[a] / $cm^3\ g^{-1}$	$S(CO_2)$ [b] / $m^2\ Å^{-1}\ g^{-1}$	$V_{pore}(CO_2)$ [c] / $cm^3\ g^{-1}$
A	249	0.081	272	0.110
B; A	393	0.102	333	0.119
B; A; B	0	0.002	n.a.[d]	0.117
B; A; B; A	257	0.093	288	0.111

[a] micropore volume, determined from total gas uptake at $p/p_0 = 0.1$; [b] cumulative surface area due to micropores, NLDFT model (CO_2, slit pores, carbon); micropore volume , NLDFT model (CO_2, slit pores, carbon); [d] not applicable.

Although all freeze-dried samples showed only almost negligible hysteresis, a pronounced hysteresis loop was often observed for evaporative dried materials, see black line and symbols in Figure 16b. This points to kinetic effects of the CO_2 molecules' hampered ability to enter and/or leave the micropores.[49] The preparation details of the different batches and exact drying conditions must have played a crucial role in formation and/or fixation of the microstructure. For example, the CO_2 adsorption isotherms in Figure 20a were measured on a sample from another batch and they do not feature a pronounced hysteresis.

This hypothesis is supported by SEM images of both types of materials, see Figure 17. Evaporative drying generates a rather dense network which does not display any visible porosity. In opposition to this, freeze drying leads to an open meso-/macroporous network structure where the diffusion of gas molecules to the pore walls can occur more easily.

Still, this does not provide a satisfactory explanation for the ability of carbon dioxide to adsorb on both freeze-dried and evaporative dried samples as well as the inability of nitrogen to adsorb on the evaporative dried sample.

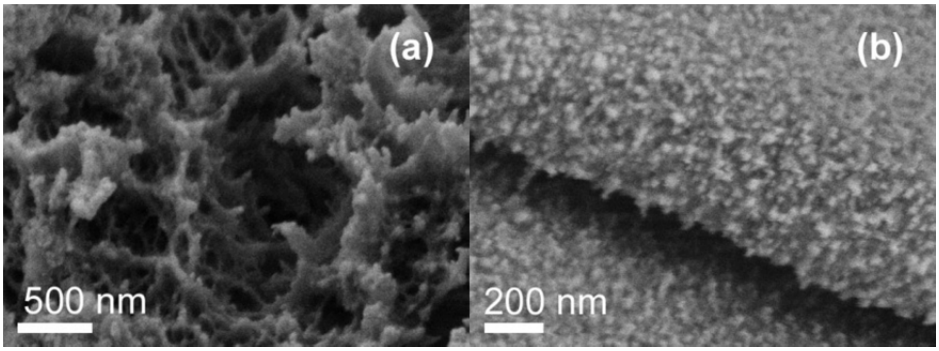

Figure 17. (a) SEM images of a freeze-dried and (b) evaporative dried sample.

This mismatch between CO_2 and N_2 adsorption data has been investigated in more detail. Three assumptions have been made in attempt to illuminate this problem. Firstly, the simplest explanation is to suggest that the molecule size of the adsorbate plays the leading role. CO_2 with its kinetic diameter of 3.3 Å could access smaller pores than the N_2 (d = 3.64 Å). In this case, one can utilize a probe with even smaller kinetic diameter and monitor if it would be able to access the pores of the both materials. Secondly, the measurements can be conducted at different temperatures. Possible temperature effects can be observed and the adsorbate behaviour can be compared at its condensation temperature. And thirdly, it would also be plausible to suggest that a certain surface barrier, impenetrable for some of the adsorbates, emerges after the processing. These three assumptions are discussed in greater detail below.

Assumption 1: The size of the adsorbate molecules

The first feasible assumption to explain the observed data is to propose that the magnitude effect takes place in gas sorption measurements. The kinetic diameter of CO_2 is with 3.3 Å smaller than that of N_2 (3.64 Å). The difference could possibly be responsible for the fact that CO_2 is adsorbed on any sample, irrespectively of the drying method. This is why an experiment using an adsorbate with a smaller kinetic diameter, i.e. H_2 (2.89 Å)[115], was conducted. The hydrogen sorption isotherms are presented in Figure 18. The unambiguous preference in adsorption

on the freeze-dried material is evident. The same trend was observed with the nitrogen sorption shown in Figure 16a.

This means that the size effect alone cannot be attributed to these networks; otherwise hydrogen would have also been adsorbed on the surface of the evaporative dried sample like CO_2. However, it can be suggested that the interactions of polar groups with CO_2 can lead to its better solubility in polymer. Thus, CO_2 can reach the void spaces more easily than H_2.

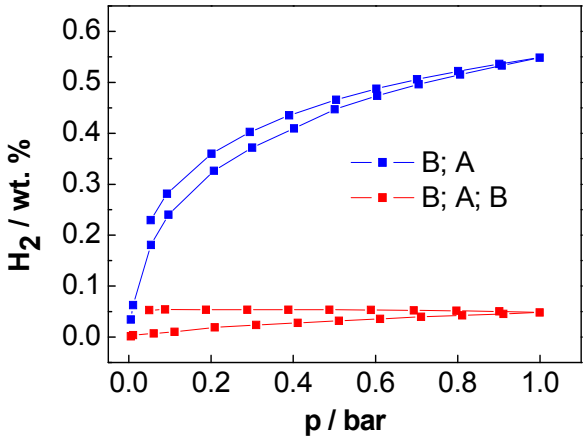

Figure 18. H_2 sorption at 77 K of a freeze-dried (blue) and an evaporative dried sample (red).

Meanwhile, the H_2-uptake of 0.55 wt.% at 1 bar of the freeze-dried sample (S_{BET} = 393 $m^2 \cdot g^{-1}$) is quantitatively comparable to other reported materials. The *PIM-1* (S_{BET} = 760 $m^2 \cdot g^{-1}$) discussed in Chapter 2.1 was able to adsorb ca. 1 wt.% H_2 at 1 bar and 77 K.[116] Polydivinylbenzenes, reported by *Frechet et al.*, with BET surface areas of ca. 460-570 $m^2 \cdot g^{-1}$, adsorbed 0.5 wt.% H_2 at 1.2 bar.[117]

Assumption 2: Temperature

To investigate the effects of temperature, gas adsorption measurements were conducted using various adsorbates at different temperatures. At this point it should be stated that the temperature can have two competitive effects on gas adsorption onto the surface of a material. Firstly, the thermal energy of the adsorbate can be rather low at the experimental conditions applied, i.e. at

cryogenic temperatures. This means that if the pores are approximately the size of the probe gas, the thermal energy of the adsorbate may be insufficient to "push" the molecules into the pores. This results in none or negligible adsorption, though the pores are present in the material. In this case, a slight increase in temperature provides the gas molecules with extra thermal energy, leading to larger uptake than at a lower temperature. Naturally, thermal energy also affects the adsorbent. A narrow pore channel would gain thermal energy on temperature rise, which would result in more molecular vibrations and hence, the variation of the pore width with time. This accounts for a larger gas uptake at a slight temperature increase as well. Secondly, there is an opposite effect which accounts for a smaller uptake with increasing temperature. This happens when the temperature rise is big enough to supply for a major increase of the vibrational energy of the adsorbent. The higher the energy, the greater is the amplitude of molecule vibrations. The constant moving and reshaping of the surface counteracts the gas adsorption and contributes to desorption, decreasing the coverage with time. In other words, an increase in temperature results in lower gas uptake.

Considering the difference between the N_2 and CO_2 sorption measurements, it can be suggested that the formerly described temperature effect takes place. Nitrogen is able to access the pores of a freeze-dried sample at 77 K, but not those of the evaporative dried material. It can be assumed that the denser structure of the latter comprises collapsed voids and the nitrogen solely lacks thermal energy to agitate the voids to open up. Therefore, it can be proposed that an increase in temperature would allow the material to exhibit the ability to adsorb nitrogen as well. Hence, additional gas sorption measurements were conducted at 273 K, 195 K and 87 K (Figure 19, Figure 21 and Figure 23).

Firstly, CO_2 and N_2 at 195 K and 273 K have been compared. Higher nitrogen uptake at 195 K (Figure 19a) of the freeze-dried sample and negligible uptake of the evaporative dried material follow the same tendency as at 77 K, like in principle in all nitrogen sorption measurements. From the nitrogen sorption

measurements at different temperatures, it seems that the evaporative dried material displays a non-porous character, as no significant uptake could be registered.

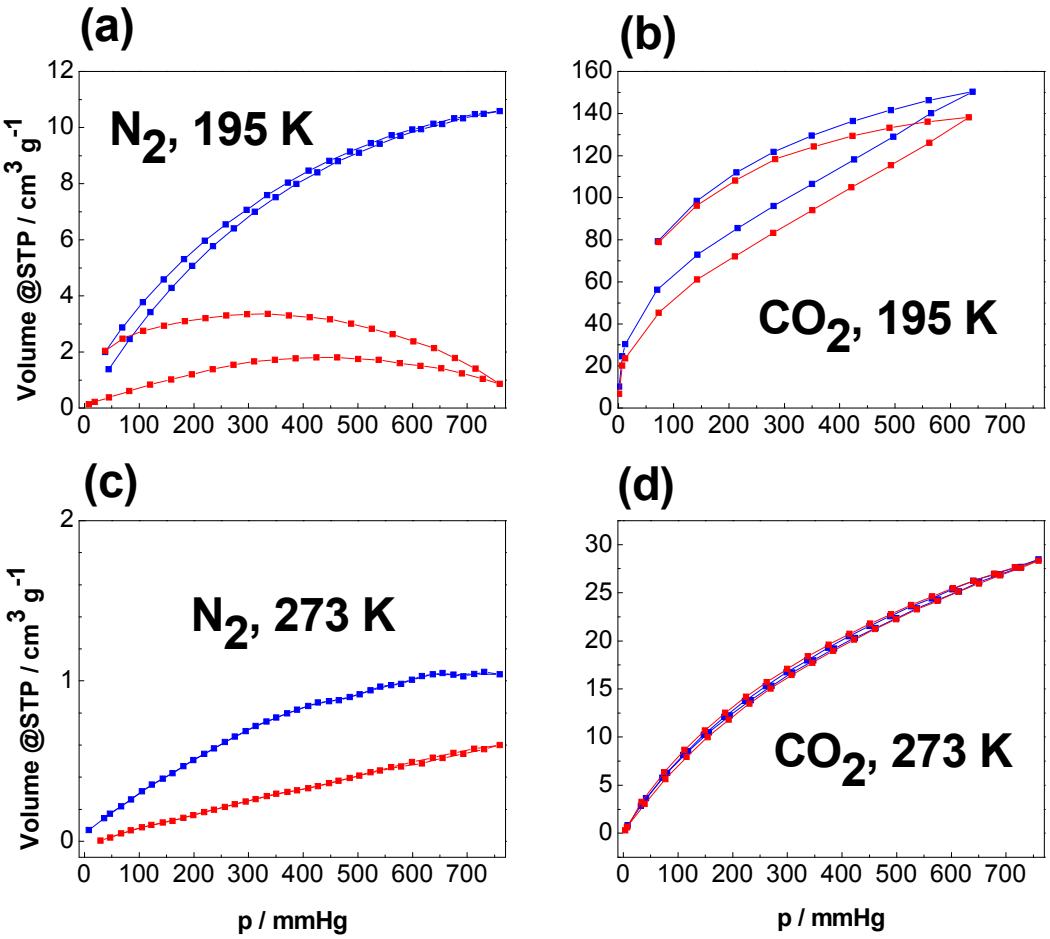

Figure 19. Nitrogen and carbon dioxide sorption isotherms at different temperatures (see legend) of a freeze-dried (blue) and evaporative dried (red) material.

The hysteresis of the evaporative dried sample at 195 K should be accounted to experimental error, i.e. virtually no adsorption takes place at this temperature. Presumably, the microstructure collapses on thermal drying of the sample and a slight temperature elevation does not support the opening of the voids that would lead to an increased gas uptake. Further temperature rise from 195 K to

273 K (Figure 19c) overloads the freeze-dried material with thermal energy, dramatically minimising its gas uptake (ca. 10 $cm^3 \cdot g^{-1}$ → 1 $cm^3 \cdot g^{-1}$; see the explanation of the latter temperature effect above). At the same time, the temperature elevation seems to finally let a marginal amount of N_2 into the evaporative dried material. Although the overall uptake is only ca. 0.6 $cm^3 \cdot g^{-1}$, the isotherm is entirely reversible, which means that minimal adsorption does take place (see the explanation of the former temperature effect above).

On the other hand, the CO_2 sorption at 195 K (Figure 19b) does not feature any major qualitative distinction from the sorption behaviour at 273 K (Figure 19d), i.e. the overall gas uptake of both samples is somewhat equal and rather large, comparing to N_2 sorption. However, the freeze-dried material at 195 K shows a pronounced hysteresis, indicating that supposedly at this low temperature there is a contribution of kinetic effect present and the CO_2 molecules have restricted access and/or exit even to this material. It should be noted that the pressure region for the measurement was controlled in accordance to thermodynamic properties of the CO_2, i.e. keeping it in a fluid state. However, the condensation takes place at these conditions. Moreover, CO_2 can lead to elastic distortion of the material and is known to be able to dissolve in polymers, especially in polyimides.[118–120]

Summing up the above presented data, an obvious conclusion can be made that CO_2 has better access to the micropores of the material, probably because of its special interactions with the adsorbent. Hereby, an explanation should be introduced to illustrate this matter. It is reasonable to infer possible favourable interactions between the adsorbate and the surface of the adsorbent. Having a larger quadrupole moment compared to N_2, the CO_2 molecule can exhibit stronger interactions with the polar surfaces. The ester linkages in line with the hydroxyl and acid side groups of the network are alleged to be the preferential adsorption sites for these interactions. One can assume that not merely physisorption is accounted for the general CO_2 sorption on differently processed materials. Regardless of the microstructure, the chemical content of those

materials should be identical, thus providing the same adsorption sites and hence resulting in equal gas uptake. To survey this hypothesis, the isosteric heats of adsorption have been calculated from the CO_2 adsorption isotherms at 273 K, 278 K and 283 K, see Figure 20b. An example of the adsorption isotherms for the evaporative dried sample is given in Figure 20a.

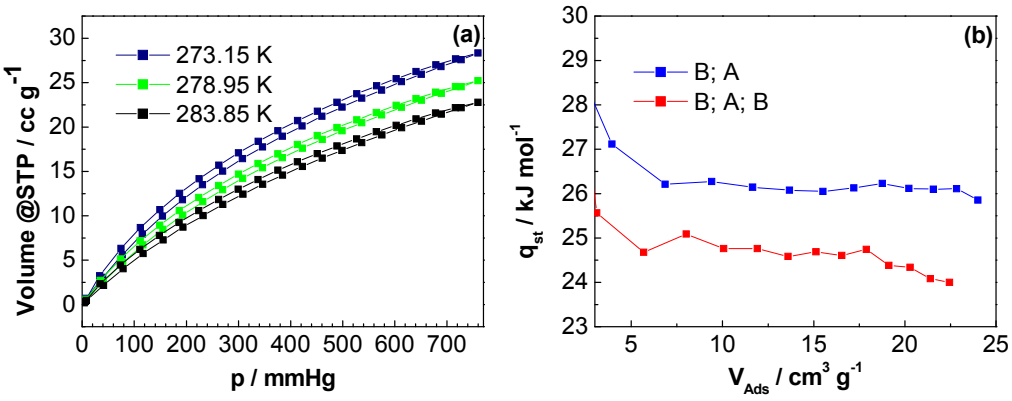

Figure 20. (a) CO_2 sorption isotherms of an evaporative dried sample at given temperatures; (b) isosteric heats of adsorption of CO_2 calculated from the adsorption branch of a freeze-dried (blue) and an evaporative dried (red) material.

The final value for the isosteric heat of adsorption at high volume uptake reaches ca. 24 kJ·mol^{-1} for the evaporative and 26 kJ·mol^{-1} for the freeze-dried sample respectively ($|\Delta H_{ads}| = q_{st}$, isosteric heat of adsorption is the absolute value of differential enthalpy of adsorption mentioned in Chapter 3.1). These quantities may be presumed as equal, neglecting the minor difference accountable for the experimental error. Similar findings have been obtained for another experimental batch. According to BET theory, the adsorption heat should decrease rapidly from its maximum value until it becomes equal to the latent heat of condensation of the gas being adsorbed (ca. 20 kJ·mol^{-1} for CO_2), at the point where the first monolayer has been completed.[121,122] The deviation in the experimental values may occur due to the heterogeneity of the adsorbent or due to the start of the formation of the second monolayer, before the first one has been completed. In fact, the largest observed value of the enthalpy of

physisorption is −25 kJ·mol^{-1}, whereas the chemisorption process delivers values around −200 kJ·mol^{-1}.[73] Thus, the CO_2 adsorption can be regarded as rather physisorptive, without any additional contributions from chemisorption.

To determine other implications of the temperature, gas adsorption, at a temperature where saturation pressure is equal to the atmospheric pressure, has been recorded for several adsorbates (77 K for N_2, 195 K for CO_2 and 87 K for Ar). The argon adsorption measurement was only performed for the freeze-dried sample, since like for N_2 at 77 K, none or negligible adsorption was expected to take place. Argon exhibits much weaker attractive fluid-pore interactions for most adsorbents. It does not possess a quadrupole moment like N_2 and CO_2 and therefore does not develop specific interactions with the surface functional groups. Hence, argon fills micropores of less than 1 nm in diameter at higher relative pressures compared with nitrogen. This enables high-resolution measurements in less time compared to nitrogen, which was also observed.

The diffusion phenomenon mentioned in Chapter 3.1 regarding the nitrogen sorption should also be present. Consequently, longer equilibrium times are expected since the pores are being filled slower because of the diffusion in the smaller channels.

It is noticeable that the isotherms, collected for the freeze-dried sample, of all three gases at their saturation pressure (Figure 21) are both qualitatively and quantitatively similar. The isotherms exhibit dual-mode sorption behaviour (see Chapter 2.1). In the low pressure region an idealised Langmuir behaviour can describe the isotherm progression:

$$C_H = \frac{C'_H bp}{1 + bp} \qquad (4\text{-}1)$$

In higher pressure regions at higher gas concentration, the isotherm increases linearly following Henry´s law:

$$C_D = k_D p \qquad (4\text{-}2)$$

It accounts for the dissolved adsorbate molecules in the polymer matrix. The obtained isotherms were, however, not fitted with Langmuir model due to its unrealistic assumptions for the materials presented in this work (e.g. perfectly planar surface and mere monolayer coverage).

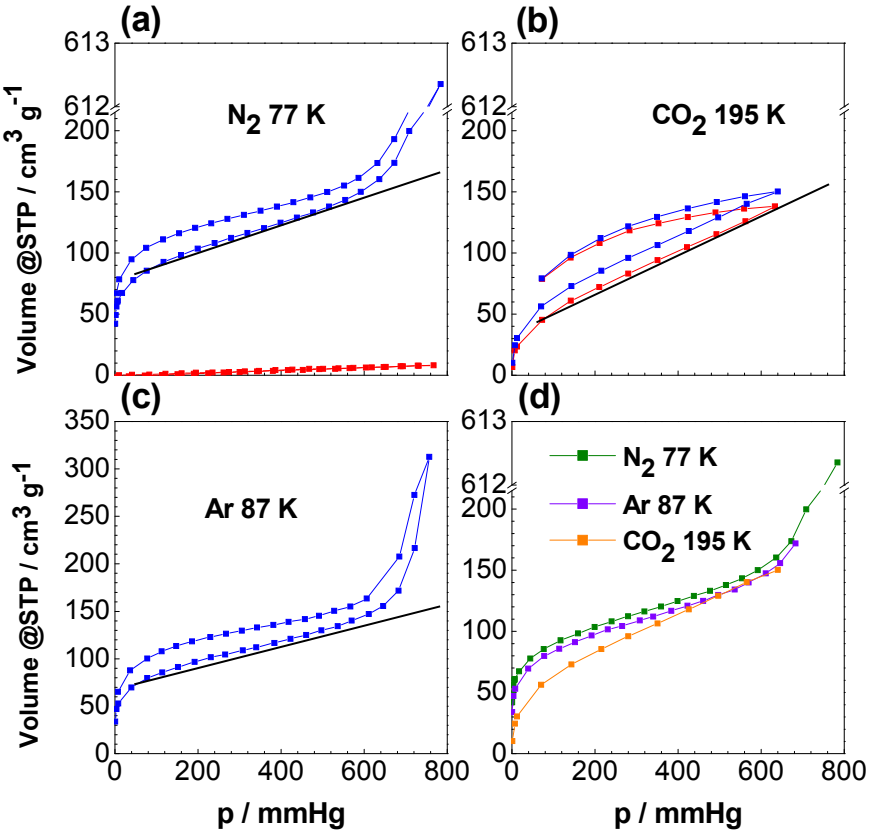

Figure 21. (a) Nitrogen, (b) carbon dioxide and (c) argon adsorption isotherms at different temperatures (see legend) of a freeze-dried (blue) and evaporative dried (red) material; (d) adsorption part of the isotherm of the freeze-dried sample. Black lines are added to emphasize almost linear component of the isotherm.

The other point that attracts attention is that all these isotherms recorded at the saturation pressure of the gas do not end in a plateau at higher relative/absolute pressure, which would be expected for microporous solids in a *Type I*[27] isotherm, see Figure 7. This could be due to the condensation of adsorbate among the network particles. It can also be suggested that with the restricted diffusion at the saturation pressure of the gas, the pores are filled very slowly. Thus, the single points of the obtained isotherms do not correspond to the

genuine equilibrium conditions, but only to the tolerance pressure region set in the experimental parameters. It is to assume that the real equilibrium conditions are not accessible at a realistic experimental timescale. Similar findings have been reported for activated carbons; the diffusion rate can be inconceivably slow because of the low kinetic energy of nitrogen at 77 K.[123,124]

The appearance of the hysteresis at high relative pressures, typical for meso- and macropores of the two most recently mentioned curves, could presumably result from the faster diffusion at higher pressure. This, however, is not of interest for this work and will not be discussed further.

In micropores, “liquid plugs” can occur, blocking the inner volume of the pore for adsorption and slowing down the diffusion, see Figure 22.

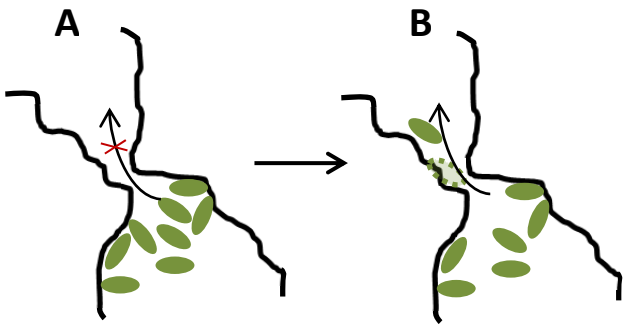

Figure 22. Graphic representation of a liquid plug at low p/p_0 (**A**) and pore filling via solvation-diffusion mechanism in higher pressure region (**B**).

In **A**, the adsorbate molecules cannot pass the narrow pore entrances due to restricted diffusion in low pressure region at the time scale of the measurement. Over the course of the experiment the pore filling takes place via a solution-diffusion mechanism, see **B**. Hence, restricted access due to slow diffusion is responsible for the above mentioned adsorption processes of adsorbates at their saturation pressure. The restricted access can also be explained thermodynamically. With increasing relative pressure, the solvation pressure of the fluid also increases. The solvation pressure describes interactions between solid surfaces separated by thin liquid layers. It depends on the state of fluid in

the gap between the surfaces and the gap width.[125] Solvation pressure was reported to become positive at increasing adsorption of Kr and Xe on zeolite X. The densification of packing in the adsorbed phase comes forward, the adsorption stress increases, and, consequently, the material expands. At very low pressure contraction of the solid framework is induced by attractive dispersive forces with guest molecules, serving as “bridges” between the framework molecules. This behaviour is typical for most zeolites and other microporous materials.[126]

Increasing the measurement temperature from 77 K to 87 K brings about some qualitative changes in the isotherm. For better comparison, absolute isotherms collected for nitrogen sorption on a freeze-dried sample at 77 K and 87 K and for argon at 87 K respectively, are displayed in Figure 23. The hysteresis of all three isotherms is pointing to swelling effects of a non-rigid network. The evaporative dried sample displayed the similar negligible nitrogen uptake at 87 K like at 77 K and is not shown in the graph.

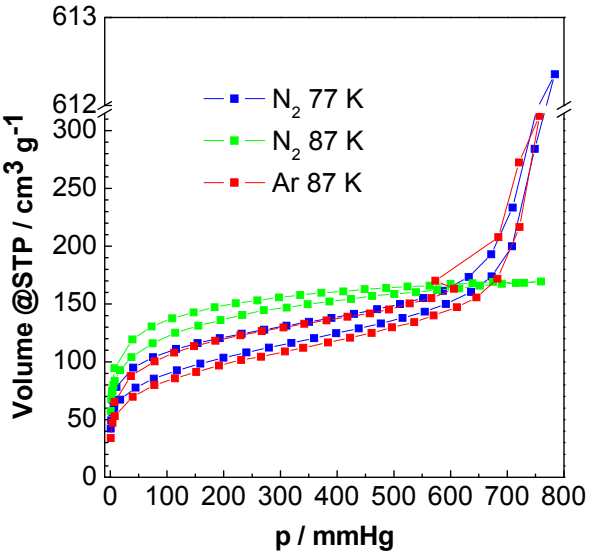

Figure 23. Absolute isotherms obtained by nitrogen and argon sorption (see legend) of a freeze-dried sample.

In general, the results of the N_2 sorption at 87 K and those at 77 K follow the same trend, featuring almost non-existent nitrogen uptake in the evaporative and the large uptake in the freeze-dried material. In this case a complementing CO_2 measurement could not be performed as the gas would solidify at given conditions.

The already discussed isotherms of the freeze-dried sample measured at saturation pressure (N_2 at 77 K, Ar at 87 K) do not end in a plateau due to restricted access and slow pore filling. On the contrary, the nitrogen adsorption isotherm measured at 87 K displays almost perfect *Type I* shape with a plateau in high-pressure region. Furthermore, a higher gas uptake is registered in the low-pressure region.

Plotting *relative* isotherms of N_2 sorption measurements at 77 K and 87 K enables a deeper insight into the microstructure, see Figure 24. A higher uptake at 87 K and a more pronounced hysteresis at 77 K are clearly evident.

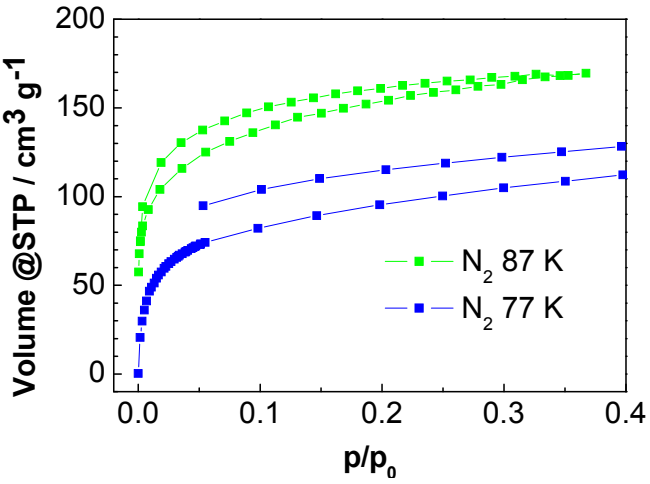

Figure 24. Relative isotherms obtained by nitrogen sorption at 77 K and 88 K.

This can probably not be explained by gating effects of the polymer since the difference of 10 K would likely be insufficient to accomplish this. The observed behaviour can be associated with the higher thermal energy of nitrogen at 87 K and hence faster diffusion. The isotherm is most probably obtained in good

equilibrium conditions. Similar findings were reported for nitrogen adsorption at 77 K and 90 K for activated carbons.[124] Adsorption at 77 K proceeded extremely slowly and proper equilibrium measurements required as long as 6 weeks, which indicated that the pore dimensions are similar to those of the nitrogen molecule. At 90 K, the time required for equilibrium is dramatically reduced, and the amount adsorbed is larger than that determined in conditions of apparent equilibrium, but smaller than that corresponding to proper equilibrium conditions. In this work, only the isotherms in apparent equilibrium were collected, but the qualitative behaviour of the isotherms coincides with the ones reported in ref. [124]. The fact that the amount adsorbed at 87 K or 90 K is larger than that at 77 K confirms the restricted diffusion of the nitrogen molecules at 77 K due to the constrictions of the micropores so that the entry into the cavities is a rate process with a positive temperature coefficient. Hence, an increase in adsorption temperature leads to an increase of the diffusion of adsorbate molecules through the constrictions and consequently to an increase of the overall gas uptake.

Looking at the plateau limit of the N_2 at 87 K isotherm from Figure 23, one can observe that it lies around 170 $cm^3 \cdot g^{-1}$ (at standard temperature and pressure, STP). The gas uptake of all three isotherms is equal to this value at ca. 670 mmHg. Considering the faster diffusion of N_2 at 87 K, the plateau limit of complete micropore filling and consequently equilibrium conditions, one can deduce that the correct micropore volume (in the absence of mesopores) derived from the measurements at 77 K should be chosen at this pressure value, i.e. not at $p/p_0 = 1$ or $p/p_0 = 0.1$ (as sometimes done for microporous materials)[127] but at $p/p_0 \approx 0.85$.

From the points mentioned above, I can draw the conclusion that the evaluation of a microporous material is not at all complete from a simple N_2 adsorption measurement at 77 K. It is highly probable that all standard sorption measurements on microporous materials are conducted in non-genuine equilibrium and therefore the pore volume and the pore size distributions

calculated from those measurements are erroneous. It is thus indispensable that new theoretical models like NLDFT and QSDFT at 87 K are developed to overcome this problem, as N_2 adsorption at 87 K appears to be a wise choice to obtain correct data about the micropores.

Assumption 3: surface barrier layer and processing

Reviewing the speculations presented above, the question about the microstructure of the polyester network is still open. The discussion originated from N_2 and CO_2 adsorption measurements at 77 K and 273 K respectively. The standard nitrogen sorption at 77 K indicated that the processing method was crucial for the stability of the micropores and that the evaporative drying may have led to pore collapse, as no apparent surface area was detected for those materials. On the contrary, the CO_2 uptake at 273 K was comparable for all materials, irrespective of the drying protocol. The question arose if these two measurements could be directly compared and if a plausible explanation regarding the microstructure could be rendered despite the discrepancies between them. Thus, in the third assumption, I stated that a certain surface barrier, impenetrable for some of the adsorbates, could have emerged after the processing. The discussion of this assumption follows hereafter.

An additional porosity analysis was conducted by the means of ^{129}Xe nuclear magnetic resonance. Loading the material with xenon was only possible for the freeze-dried sample. The apparent pore collapse observed in the evaporative dried sample was affirmed by the xenon measurements. The ^{129}Xe-NMR spectra of the freeze-dried sample display only faint signal in the range from 162 ppm to 210 ppm at 100 mbar to 1300 mbar xenon pressure respectively, see Figure 25a. The pronounced peak around 1-2 ppm belongs to xenon, adsorbed at the outer surface and xenon between the particles. In this case the movement of the atoms is not constrained, inducing a sharp signal. The high values of the chemical shift indicate that the material possesses very small pores. In these pores, the xenon atoms are intensively exposed to interactions with the absorption sites

and interatomic collisions, which leads to a very broad signal. On the whole, the chemical shift is dependent on the xenon pressure. The higher the pressure, the less the xenon nuclei are shielded by the surrounding electron density and the more the signal is shifted downfield, i.e. to a higher chemical shift. To visualise this feature, the chemical shift values were plotted against the xenon load pressure and fitted linearly.

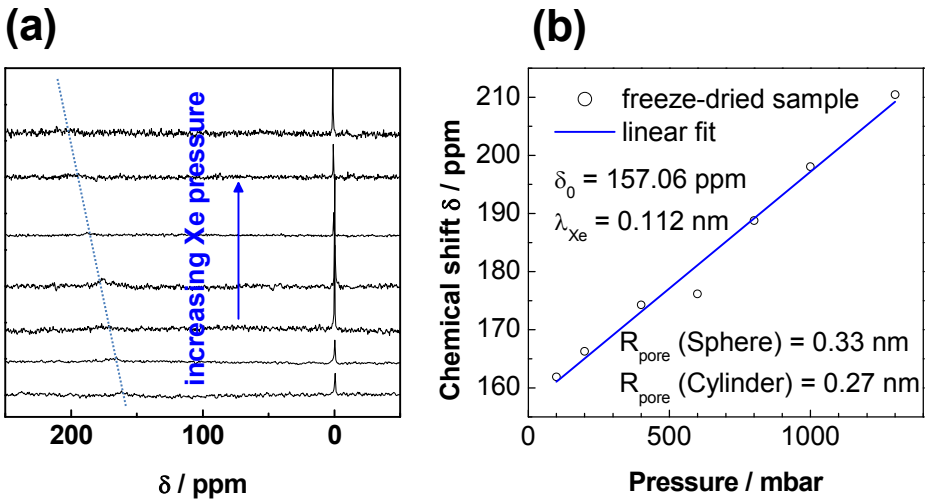

Figure 25. (a) ^{129}Xe-NMR spectra of the freeze-dried sample loaded with xenon from 100 mbar (the lowest curve) to 1300 mbar (the most upper curve), the dotted line should emphasize the signal location; (b) chemical shift of xenon confined within pores as a function of applied xenon pressure.

According to equation (3.6) of the Fraissard model with δ – the intercept value of the linear fit (Figure 25b) and λ – the mean free path of xenon, pore radii of 2.7 Å and 3.3 Å were calculated for cylindrical and spherical pores, respectively. The values obtained from CO_2 sorption at 273 K using a DFT method are in the range from 1.8 Å to 4 Å. Nitrogen sorption at 77 K revealed expectedly larger pore radii of 7 – 8.3 Å according to QSDFT calculations on slit pores. As mentioned above, the constrained diffusion of the adsorptive at this temperature may not allow nitrogen to enter the narrowest pores, thus only detecting the larger pores. Along with this, ^{129}Xe-NMR measurements show that the pores of a freeze-dried sample are very small and those of an evaporative dried sample apparently

absent (no xenon load was achieved in the experiment). This delivers a first hint that the processing dramatically influences the surface, possibly creating a so-called surface barrier.[128]

Recalling the feature that both the freeze-dried and the evaporative dried samples had in common, which is the comparable CO_2-uptake at 273 K (Figure 16b), one can suggest a general CO_2-affinity of the material. Table 4-5 contains values for adsorbed volumes of CO_2 and N_2, both measured at 273 K, and the respective CO_2/N_2 selectivities of the freeze-dried and the evaporative dried samples.

Table 4-3. Adsorbed volume for CO_2 and N_2 at 273 K and the respective CO_2/N_2 selectivities of the freeze-dried and the evaporative dried samples, determined from the total uptake of the gas at 760 mmHg.

	$V_{ads}/cm^3 \cdot g^{-1}$ freeze-dried	$V_{ads}/cm^3 \cdot g^{-1}$ evap. dried
CO_2, 273 K	28.49	28.34
N_2, 273 K	1.04	0.60
CO_2/N_2	27	47

Due to the low N_2-uptake of the evaporative dried sample (like in all nitrogen adsorption measurements), its CO_2/N_2 selectivity exhibits a high value of 47. On one hand, this could be a first indication of a potential application as a membrane, provided the material is processable. A closer look to this issue is given in Chapter 4.2: “Soluble polymers from betulin”. On the other hand, this can give a second hint to the existence of a surface barrier, arising after evaporative drying of the sample.

Furthermore, the structure was investigated by means of small-angle X-ray scattering, see Figure 26a. The evaporative dried material displays a small and broad halo at a scattering vector $q \approx 3.65$ nm^{-1} (corresponding to a real space value of ≈ 1.7 nm). This halo is also weakly visible in the SAXS-pattern of the freeze-dried materials, showing their structural identity on a micropore level. The

freeze-dried samples additionally exhibit a decay of the scattering intensity with a power of -4 at small *q*, which partially overlaps with the above-mentioned peak. This decay is the well-known *Porod* behaviour of a two-phase system.[129] Finally, all samples show an increase of the scattering intensity at large *q*, which is the onset of a peak at q = 9.6 nm^{-1} (visible in wide-angle X-ray scattering, WAXS, see Figure 26b).

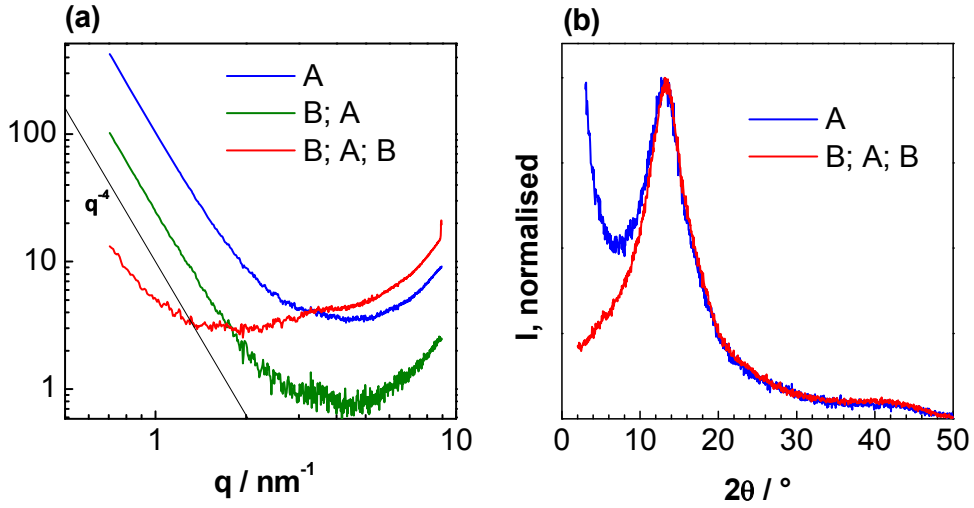

Figure 26. (a) SAXS patterns and (b) normalised WAXS patterns of the same network batch, dried in a different way; *A* – freeze-dried, *B* – evaporative dried.

This peak dominates the WAXS regime of all samples and was insensitive to the applied drying method. The minor difference of *d* value ≈ 6.6 Å for the freeze-dried and 6.5 Å for the evaporative dried sample is in the range of experimental accuracy and could be accounted for an unequal sample amount or height by its positioning during the measurement. Commonly the WAXS features of amorphous polymers are limited to one or two amorphous halos, representing distances of closest approach between segments of different chains. For *PIM-1*, X-ray scattering has been recently measured and modelled by molecular dynamics simulations.[11,130] It has been shown that the measured broad peaks represent characteristic distances between segments or sites of contortion on different chains. It would be helpful if such models would be developed further, since the creation of the packing model for the calculations that accurately

represents the material, is non-trivial and this research field is rather young. Concluding this, one can say that WAXS data suggest that on the atomic level there are no differences present. This is seconded by SAXS patterns, which reveal the consistency of both structures. Combining this implication with the comparable CO_2-uptake of both samples (see Table 4-5), it is feasible to propose that the bulk microstructure of both materials is the same and a surface effect is indeed present.

All in all, gas sorption techniques provide quantitative measurements of the accessible internal surface area, but are subject to kinetic limitations and do not probe closed pores. It is feasible that the gas sorption measurements presented above cannot illustrate the unambiguous picture of the microstructure. The pores are present in the networks freeze-dried from dioxane but seem to be non-existent if the same batch is let to dry at elevated temperature *in vacuo*, as probed by N_2 at 77 K. Resembling findings have been reported for crystalline Zn-containing MOFs.[128,131,132] Authors stated a discrepancy between the porosity predicted by crystallography and porosity measured by gas sorption analysis, referring to *surface barrier*. Most of the external surface appears to be blocked, while the transport resistance of the remaining open pores is negligibly small. Surface barrier is a special case of the transport resistances that may appear quite generally at phase boundaries and the boundaries of compartments such as cell membranes. It can be investigated via interference microscopy (IFM) and IR microscopy (IRM). Positron annihilation lifetime spectroscopy (PALS) helped to reveal a densified surface layer preventing the entry of even small molecular species into the MOFs in ref. [131]. The authors showed that at higher temperatures, occurring degradation is accounted for collapsing of the larger pores responsible for gas transport. Moreover, the material was mechanically crushed to determine whether the surface layer was due to the presence of a dense guest-filled layer or collapse of the crystal itself. No porosity was detected by N_2 at 77 K, indicating that the surface collapse is presumably due to inherent instability of the dry material. In this work, a comparable experiment was

conducted with the evaporative dried network. The resulting isotherms of nitrogen sorption at 77 K are presented in Figure 27. One could suppose that there is no dense external layer hindering the gas adsorption at 77 K and the material is instable on drying.

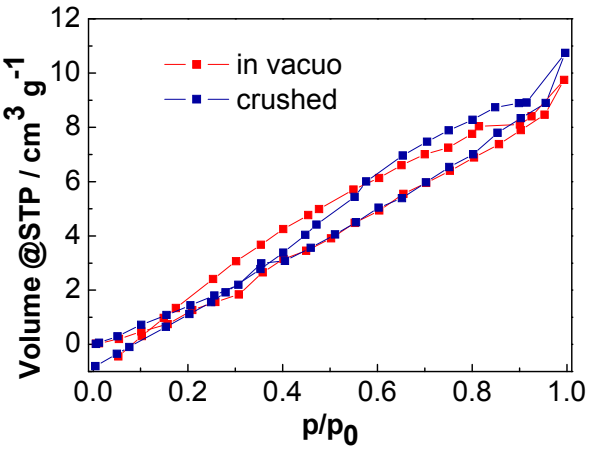

Figure 27. Nitrogen sorption isotherms of the evaporative dried (red) network and the same network mechanically crushed (dark blue), measured at 77 K.

However, it is highly probable that the physical crushing results in formation of loose polymer ends at the surface. These would naturally be more mobile than those in the bulk. Subsequently, they would reorientate and plug the pores at the surface, blocking the way to the inner bulk. Therefore, the following hypothesis can be introduced: the dense surface layer was formed while evaporative drying is impermeable for larger molecules with poor solution properties, such as N_2 and Xe. At the same time, it appears to be reachable by smaller probes having good solubility, like CO_2. Additionally, freeze-drying keeps the surface layer open. Figure 28 displays a simplified graphical representation of this hypothesis.

There is also another indirect evidence of the presence of the surface barrier layer. The X-ray scattering and the CO_2 adsorption data indicated that both evaporative dried and freeze-dried materials were identical. In other words, the "bulk" is identical. Other gas adsorption data pointed out a sharp distinction in the differently processed samples.

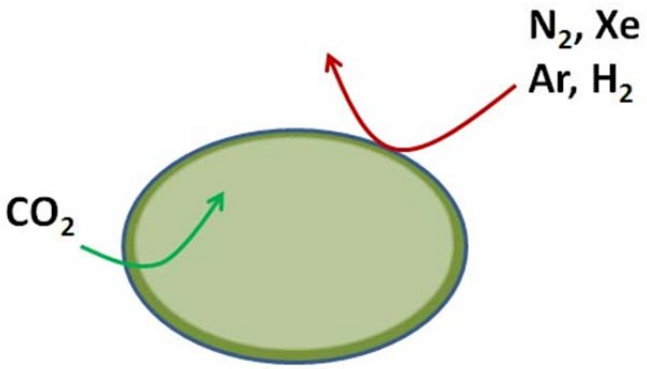

Figure 28. Surface barrier layer formed upon drying is shown as a blue-green boundary.

This disparity should consequently be explained by the presence of a surface barrier layer. It could presumably add up to not more than 1 wt.% (and therefore be left undetected), but is apparently crucial for material properties.

Concluding the discussion of the third assumption, it is plausible to suggest that the evaluation of the microporous structure of the material should not be relied solely upon the standard N_2 measurement at 77 K and that the complementary measurements of N_2 at 87 K and CO_2 at 273 K should be utilised in an attempt to characterize microporous materials. Recent publications on microporous organic networks do not even present standard N_2 adsorption isotherms, but only the results of CO_2 adsorption measurements, explaining the failure to obtain the former by low diffusivity of nitrogen into the narrow pores.[133]

Chemical analysis of the microstructure

In addition to physical analysis methods, a deeper insight into the micropore structure was acquired with chemical modification of the sample. A polyester network prepared with an excess of 1,3,5-benzenetricarbonyl trichloride of 25 mol%, has been chosen for the study. This way one can assume that the unreacted carbonyl chloride groups would be hydrolysed during work-up, building excess acid functionality in the material, see the upper image in Figure 29. Hydrogen bonds can narrow down the distance between the parts of the network, thus closing up the pores. If this is true, a treatment in basic conditions

should remove them and effectuate at higher detectable surface area, see the bottom image in Figure 29. To prove this assumption, the network was at first washed with NaOH and afterwards with HCl. After each step the sample was freeze-dried and analysed by IR-spectroscopy and gas adsorption.

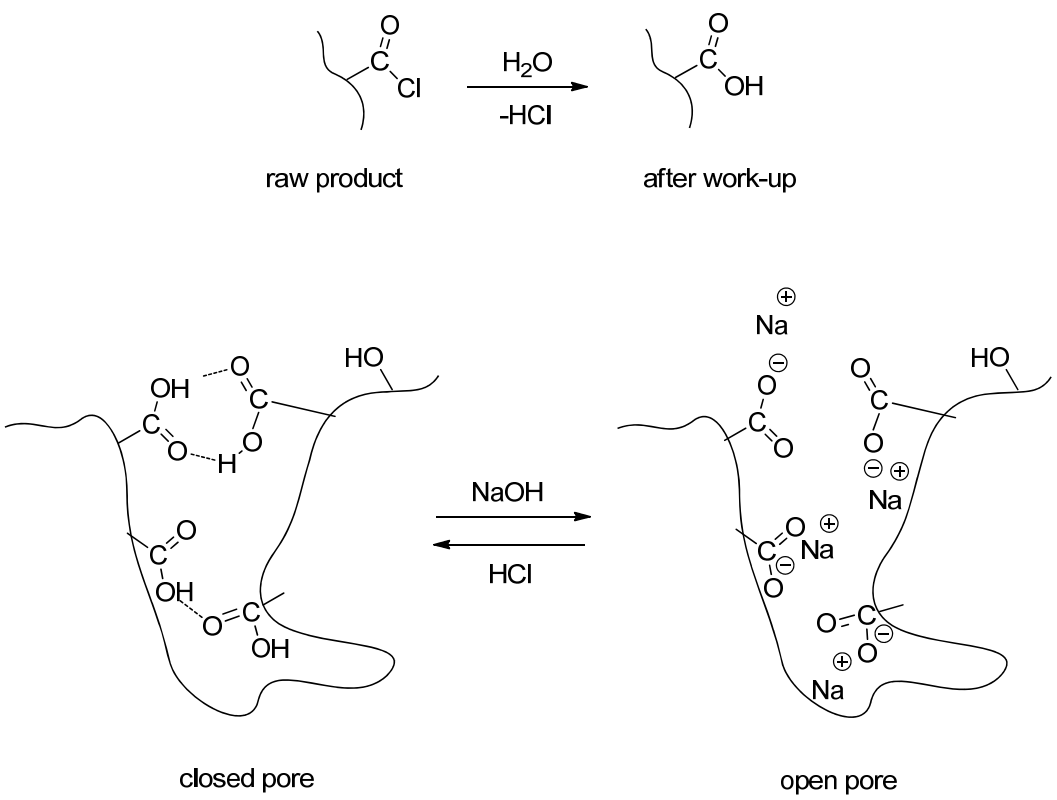

Figure 29. Schematic representation of hydrolysis of the carbonyl chloride groups (above) and a pore with surface functionality and the differences caused by basic treatment (below).

The IR-spectra for this analysis were measured in a KBr-pellet for better resolution of carbonyl and hydroxyl groups' resonance. Next to the ester carbonyl band at 1730 cm^{-1} in the FTIR spectrum of the initial network (black curve in Figure 30), there are two additional peaks at 1645 cm^{-1} and 1606 cm^{-1} (the pronounced band at ca. 2355 cm^{-1} belongs to free CO_2). Though the acid carbonyl groups normally absorb at higher wavelength than the esters, it is feasible to assume that these two bands belong to the existing acid groups,

interconnected via hydrogen bonding. The hydrogen bonding weakens the C-O double bond, which leads to resonance absorption at lower energy.[134]

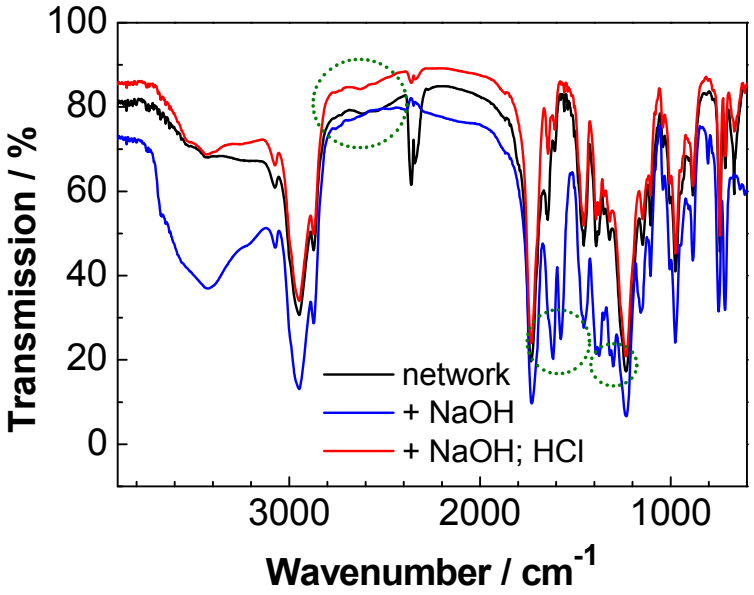

Figure 30. FTIR spectra (measured with KBr) of the same network (black), which was washed with 1M NaOH (blue) and subsequently with 1M HCl (red). The sample was freeze-dried after each washing. The dotted green circles emphasize the vibration bands mentioned in text.

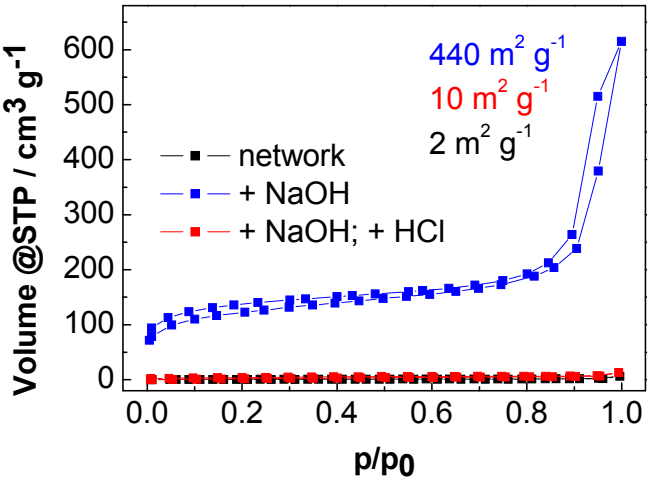

Figure 31. Nitrogen isotherms obtained at 77 K and for the same network (black), which was subsequently washed with 1M NaOH (blue) and afterwards with 1M HCl (red). The sample was freeze-dried after each washing.

Hydrogen bonding can also be responsible for the absence of high nitrogen uptake of ca. 350-450 $m^2 \cdot g^{-1}$ like normally observed after freeze-drying. The

apparent specific surface area measured by N_2 at 77 K of the freeze-dried sample amounted to 2 $m^2 \cdot g^{-1}$, see Figure 31 (black).

To prove this hypothesis, at first the network was allowed to swell in THF and then diluted sodium hydroxide was introduced directly into the mixture, since the networks displayed high hydrophobicity. After 10 min the mixture was washed with water, followed by solvent exchange and freeze-drying from dioxane. Two distinctive bands were detected by FTIR at 1620 cm^{-1} and 1576 cm^{-1} (blue), whereas the two peaks at 1645 cm^{-1} and 1606 cm^{-1} of the unmodified network (black) were absent (Figure 30). Shifting of the carbonyl band to even lower wavenumber can be associated with the building of a resonance stabilised carboxylate group. The delocalisation of the electron density results in lower absorption energy. Moreover, two almost coinciding bands appear at 1300 cm^{-1} and 1317 cm^{-1} and can be attributed to the symmetric stretching vibration of the carboxylate moiety. In addition to this, the electrostatic repulsion of the carboxylate groups combined with the "fixing" of the structure by freeze-drying led to high nitrogen uptake (Figure 31, blue).

Ester bond hydrolysis could potentially occur, but might only happen to a very small extent, since only mild basic conditions were applied for a short period of time. However, if it had been valid for all of the ester linkages, the subsequent washing in acidic media would not have changed the outcome. In other words, if the pores were chemically "etched" in the network, the residual parts would be removed by washing and another washing in acidic conditions would not bring about any change, since the pores are already present. Nevertheless, this was not the case. The acidic treatment was carried out in a similar procedure as described for the treatment with base. No significant nitrogen uptake was detected afterwards (Figure 31, red). The FTIR-spectrum revealed the disappearance of the peaks attributed to absorption in delocalised carboxylate at 1620 cm^{-1} and 1576 cm^{-1} (blue curve) and appearance of two weak bands at 1645 cm^{-1} and 1606 cm^{-1} (red curve, Figure 30). Altogether, this can suggest that the sodium carboxylate was replaced by hydrogen bonded acid groups.

Additional CO_2 adsorption investigations were performed to gain more insight. As have been already discussed above, CO_2 is more suitable for analysing microporous materials as it is able to address smaller pores than N_2. A larger CO_2-uptake was detected for the sample treated with NaOH, comparing with the sample, which was subsequently washed with HCl, see Figure 32a. The calculated values for the isosteric heat of adsorption are 26 kJ·mol^{-1} and 24 kJ·mol^{-1} respectively. The small difference is in the range of experimental error. It could also reflect the distinction in pore size distribution at ca. 2-3 Å in Figure 32b. The sample treated with NaOH has a higher pore volume in this region, than the sample, which was subsequently washed in acidic conditions.

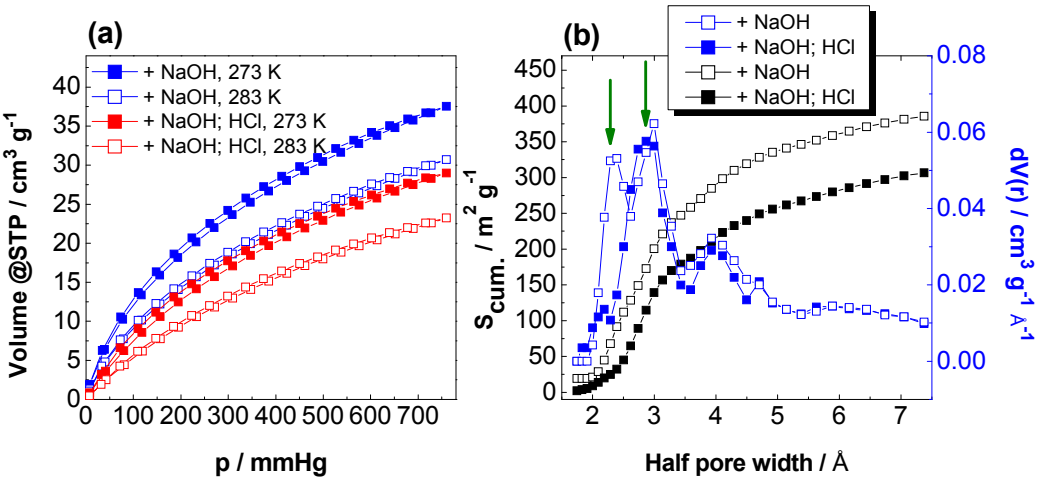

Figure 32. (a) Absolute CO_2 adsorption isotherms and (b) pore size distribution calculated using Monte-Carlo (MC) method for the network washed with NaOH and subsequently with HCl, see legend.

Apparently more CO_2 is adsorbed in more accessible small pores of the sample treated with NaOH. The small pores are also "seen" after washing with HCl but they cannot incorporate the same amount of CO_2 and are therefore quasi-restricted. Therefore it may be speculated that the small difference in the heats of adsorption might come not only from experimental error. It is probable that reaching the restricted adsorption sites of a more densified material requires some energy. Thus, the overall energy release upon adsorption would be slightly minimised. This hypothesis could also explain a similar disparity in values for

heats of adsorption for the evaporative and freeze-dried sample, see Figure 20b. The former possesses a more densified structure and its heat of adsorption is smaller than that of a freeze-dried sample.

Summing up the results of this chapter, it was proven for this model microporous polyester network that microporosity is its inherent characteristic and that it needs to be "fixed" by appropriate methods to get detected by the standard nitrogen sorption measurement. This is another example of the necessity to apply other methods than N_2 adsorption at 77 K for the characterisation of microporous materials. It has been discussed earlier that this method may be taken solely as the primary indicator of microporosity in polymer-based materials[3] and that other methods need to be applied for detailed investigations.[3,83,84,123] The above presented study endorses this statement.[108]

4.2 Soluble polymers from betulin

4.2.1 Introduction

The synthesised polyester networks with betulin and benzene moieties have been thoroughly investigated with respect to their microstructure. Porosity analysis indicated a small size of the pores, which could restrict the potential applications of the material in adsorption or catalysis, as larger molecules would not be able to enter the pores. The material was tested for Paracetamol absorption. Paracetamol is a widely-spread analgesic and antipyretic drug, which can be quantitatively detected by means of UV-spectroscopy.[135] The insoluble network was loaded with Paracetamol, diluted in water, ethanol or THF. After drying the release was monitored by a UV-signal at 244 nm in water. The results of the experiment showed that Paracetamol was probably not incorporated in the pores. The immediate release of ca. 15 mg per 1 g network indicated that the pores were too small, and Paracetamol only resided at the surface, not being absorbed into the material.

However, materials with such small pores are of interest for separation applications as membranes, promising a good trade-off between selectivity and permeability. The nitrogen and CO_2 sorption investigations at 273 K have shown that the networks have favourable CO_2/N_2 selectivity. Therefore it was attempted to synthesize soluble betulin-based polyesters with comparable structure. There are two straightforward ways to synthesize soluble polymers in a polycondensation reaction: the most obvious one is to let two difunctional monomers to react with each other, eventually adding driving force to the reaction by removing the low-molecular byproduct *in situ*.[71,136] In this classic step-growth polymerisation reaction, high molecular masses can only be achieved at high conversions when the starting substances are used in exact stoichiometric amount. This method results in linear polymers. Another way to prepare a soluble polymer is to allow an AB_n monomer to polymerise (e.g. polymerisation of an AB_2 monomer would result in a hyperbranched polymer). Having A_2 and B_3 monomers reacting with each other and stopping the reaction before the gelation occurs, will also yield a branched polymer.[137–139] The first statistical explanation of the theory of polycondensation was introduced by Flory in early 1952.[140] He was able to describe the molecular weight distribution in branched systems using a procedure involving direct enumeration of configurations.

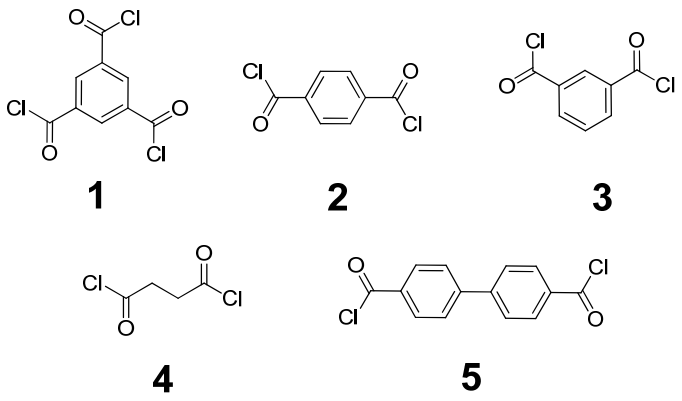

Figure 33. Structural formulae of monomers used for synthesising soluble polymers, **1)** – 1,3,5-benzenetricarbonyl trichloride (BTC), **2)** – terephthalic acid chloride (TPC), **3)** – isophthalic acid chloride (IPC), **4)** – succinic acid chloride, **5)** – [1,1'-biphenyl]-4,4'-dicarbonyl dichloride.

Both linear and hyperbranched polymers were synthesised and investigated in this work. A selection of utilised monomers is depicted in Figure 33.

The reaction scheme of the polycondensation reaction is illustrated in Figure 34 for the most investigated **2** and **3**.

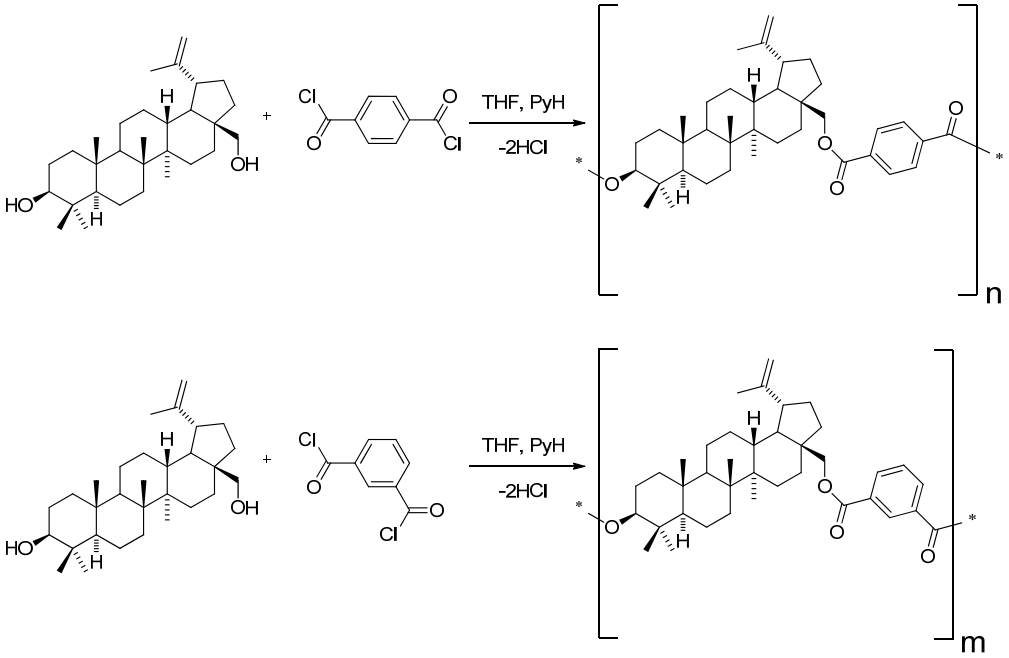

Figure 34. Reaction scheme of the polycondensation reaction of betulin with terephthalic acid chloride (top) and isophthalic acid chloride (down).

The succinic acid chloride, **4**, and the [1,1'-biphenyl]-4,4'-dicarbonyl dichloride, **5**, yielded polyesters with moderate molecular weight distributions (M_n = 2826 g·mol^{-1}, M_w = 5425 g·mol^{-1} and M_n = 7806 g·mol^{-1}, M_w = 21260 g·mol^{-1}, respectively) and low specific surface areas calculated from BET model from nitrogen sorption measurements at 77 K (both ca. 30 m^2·g^{-1}). Having in mind the potential application of the processable polymers, a film was cast from a polymer prepared from **5**. However, the brittleness of the formed film led to exclusion of this polymer from ongoing investigations. Further experiments did not result in polyesters with higher molecular weights, which could theoretically be superior candidates for film casting. High molecular weights were also not achieved with **3**, the isophthalic acid chloride. The 120° angle between the functional groups of

the benzene ring appears to be rather small, thus resulting in steric repulsion between the side groups of the fused ring system of betulin and the benzene ring. Furthermore, it can hinder the connection of these kinked oligomers to each other, yielding only polymers with moderate molar masses, which also were insufficient to form a uniform non-brittle film.

Thus, the most studied soluble polyesters were formed by the first two monomers presented in Figure 33, BTC (1,3,5-benzenetricarbonyl trichloride) and TPC (terephthalic acid chloride). Hyperbranched polymers with broad molecular weight distribution were formed from the former and linear polymers with relative high molar masses from the latter. An overview of some selected experiments is given in Table 4-4. The typical synthesis was carried out in THF with an excess of pyridine at elevated temperature. As in the network synthesis, the excess of this base has been established to result in better conversions.

Table 4-4. Overview of selected experiments resulting in soluble (denoted *S*) polymers. Concentrations are given with respect to betulin in M = mol/L; "c_{all}" denotes concentration of betulin in both THF and pyridine. GPC was performed in THF with PS as internal standard. "EtOH" in the second column means that the crude betulin extract was recrystallised from ethanol. The number stands for the drying temperature *in vacuo*.

Exp.	Betulin	Comonomer	c_{THF}/ M	c_{all}/ M	M_n/ g·mol^{-1}	M_w/ g·mol^{-1}	PDI	Comment
S1	comm.	TPC	0.030	0.029	1644	3295	2.0	
S2	comm.	TPC	0.143	0.125	4010	8353	2.1	
S3	EtOH/80	IPC	0.177	0.156	3301	7394	2.2	
S4	EtOH/140	TPC	0.400	0.302	11680	41060	3.5	CO_2/N_2
S5	EtOH/140	TPC	0.167	0.151	24320	94220	3.9	
S6	EtOH/80	BTC	0.073	0.071	71970	287000	4.0	CO_2/N_2
S7	EtOH/80	BTC	0.073	0.071	12950	128000	9.9	
S8	EtOH/40	BTC	0.073	0.071	3231	8949	2.8	@RT
S9	EtOH/40	BTC	0.073	0.071	812	2403	3.0	
S10	EtOH/140	BTC	0.073	0.071				gel
S11	EtOH/140	BTC	0.055	0.054	14950	142400	9.5	+EtOH

Hereafter, the polymer was purified from THF by precipitating in ethanol. The precipitate was dissolved in chloroform (6 wt.%) and cast as a film. The

experimental data manifested the optimal conditions for the synthesis of linear polymers: relative high concentrations (c ≈ 0.17 M) and careful moisture-free reaction implementation. An increase in concentration in more than 4 times (*S1* → *S2*) resulted in molar masses ca. 2.5 times higher. Similar concentrations in reactions with IPC (*S3*) yielded polyesters with lower molecular weight. Casting IPC-based polymers did not result in the formation of stable films.

Polyesterification in high concentration using TPC, however, formed polymers with high molecular weights (*S4*, *S5*). Stable flexible transparent films were produced by letting a chloroform solution dry on air, see Figure 35.

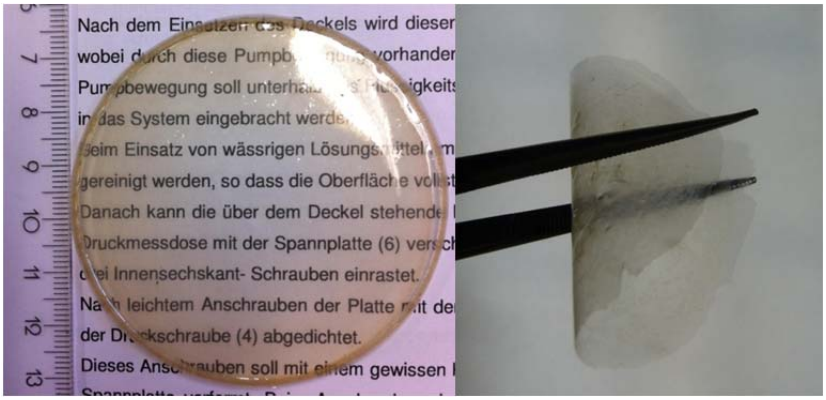

Figure 35. Photographs of films made from TPC-betulin polymer.

The hyperbranched polymers were synthesised using birch bark extract, recrystallised from ethanol. Using low concentrations of starting compounds and/or the crosslinker and stopping the reaction before the gelation point can provide a feasible way to prepare a soluble polymer from A_2+B_3 monomers. In this work, an elegant alternative was found: a hyperbranched polymer was prepared with low crosslinker concentration due to the presence of ethanol in the solvate structure. It is known that recrystallisation from ethanol can lead to a solvate with equimolar composition (ca. 10 wt.% of ethanol), which only disintegrates at high temperatures *in vacuo*.[141,142]

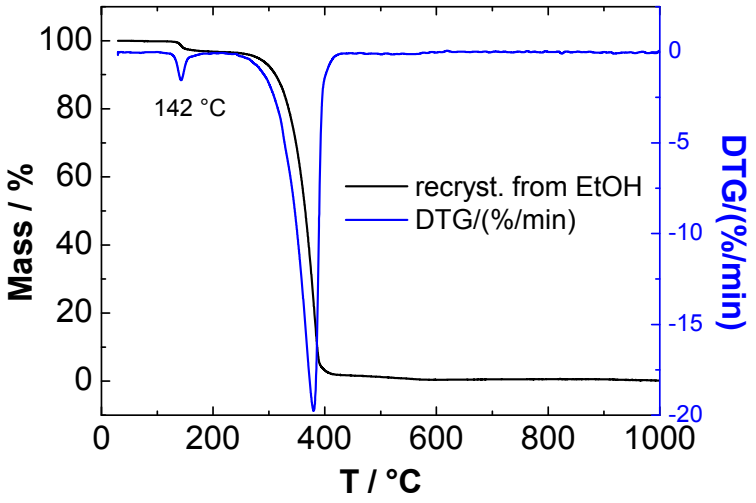

Figure 36. TGA plot of betulin recrystallised from EtOH after drying *in vacuo* at 80 °C for 24 h, measured in nitrogen flow.

Even drying *in vacuo* at 80 °C for 24 h still does not remove all the ethanol, leaving 3 wt.% encaptured, see Figure 36.

It should also be noted that the reactivity of the primary and secondary hydroxyl groups of betulin is not equal. It was reported that in pyridine, the primary hydroxyl group is four times more active.[24] The drastic effect of having a reactive alcohol alongside bulky betulin in the system can be observed in *S8* and *S9* (Table 4-4). The betulin was recrystallised and dried at 40 °C (*in vacuo*) for this reaction, yielding only soluble polyester (45%) with low molecular weights (M_n = 3231 g·mol^{-1}, M_w = 8949 g·mol^{-1} and M_n = 812 g·mol^{-1} and M_w = 2403 g·mol^{-1}, respectively). Even smaller molecular weights resulted for *S9* probably because of two reasons: presence of EtOH in the crystal structure of betulin and short heating time of the reaction. The reaction was let at room temperature after 5 h of heating at 70 °C. From the GPC curves (Figure 37) it can be seen that the growth of molecular weight proceeded only as long as the reaction mixture was heated. This can probably be explained by the lower reactivity of the secondary hydroxyl group of betulin, which needs additional thermal energy to overcome the energy barrier.

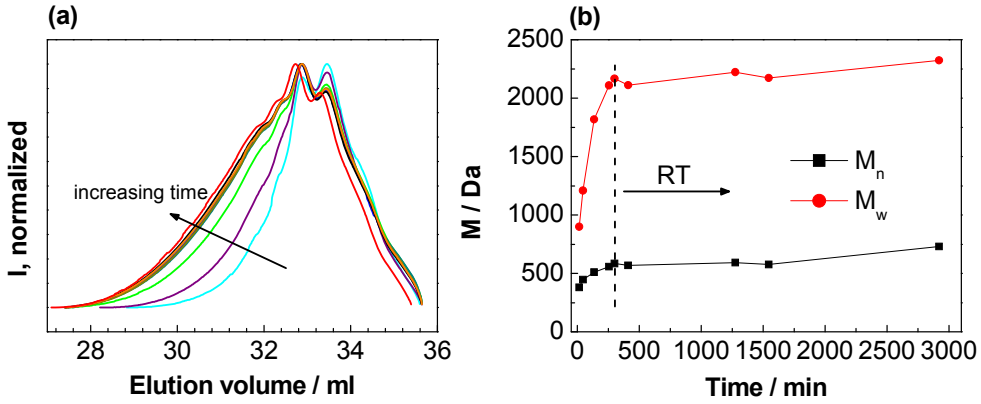

Figure 37. (a) Elution volume curves (RI detection) of the reaction progressing with time; (b) molecular weight evolution. *RT* stands for room temperature.

Apparently, more than 5 h of heating time is required for larger conversions and molecular weights. All in all, the solvate ethanol is obviously deactivating the trifunctional monomer to a high extent. The polymerisation can proceed if 1,3,5-benzenetricarbonyl trichloride reacts with a single ethanol molecule. Double or triple addition lead either to chain end or monomer dispense. Drying the recrystallised betulin at 80 °C *in vacuo* did not allow the complete removal of the entrapped ethanol (3 wt.% according to TGA in nitrogen flow, Figure 36), but resulted in hyperbranched polymer with broad polydispersity, *S6*.

The reactions above were reiterated in a slightly modified way. The betulin-ethanol solvate was fully decomposed at 150 °C in vacuo (no traces of ethanol (*quartet* at δ = 3.72 ppm) according to NMR) and introduced to the experiment. The same conditions were employed as in *S6* with the difference of gradual ethanol addition in three steps in the course of the reaction (*S10*). The gelation occurred after ca. 3h, i.e. the amount of ethanol (15 mol% respective to the amount of BTC) was insufficient to prevent it. Leaving all the variables identical and increasing the amount of ethanol to 45 mol% and the THF volume by 30% (*S11*) resulted in 80% yield of soluble polymer with high molecular weight and broad molecular weight distribution. The GPC diagrams are presented in Figure

38. The first three elution curves were obtained from the precipitated samples taken before each addition of ethanol. During the first 2.5 h predominantly weakly branched chains were formed, whereas at the end of the third hour these chains began to conjoin (appearing intensity at ca. 18-22 ml in cyan curve, Figure 38). The resulting polymer (24 h reaction time) features very broad polydispersity of 9.5.

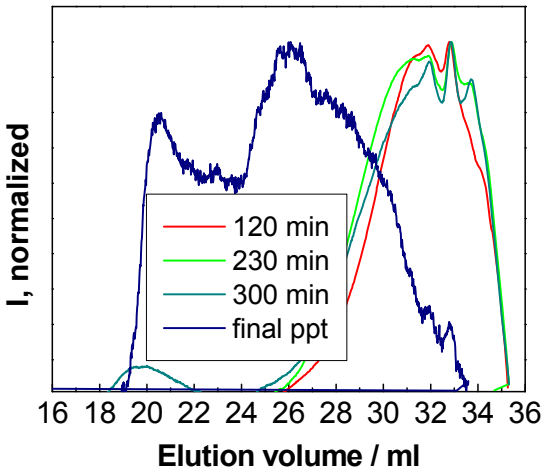

Figure 38. Elution curves (RI detection) of *S11* in progress of the reaction (see legend) and the final curve of the precipitated and filtrated sample (dark blue).

The hyperbranched polyesters, in general, did not turn out to form a stable film easily. It is known that hyperbranched polymers generally have poor film-forming ability because of the lack of chain entanglement.[105] It is also probable that the huge highly branched segments precipitate on losing solvent before it comes to film formation. Presumably, those are also incapable of packing closely like the linear chains, which is to be expected from their geometry. It is generally known that hyperbranched aromatic polyesters are very brittle bulk materials and their dense, irregular branching does not allow crystallinity or entanglement formation.[143]

4.2.2 Characterisation and discussion

Thermogravimetric analysis of linear betulin-TPC polymer showed the same trend as in the insoluble network: the degradation starts after ca. 310 °C in an inert atmosphere, see Figure 39. A small step around 100-170 °C is due to the evacuation of solvent residues. Thermal behaviour was also investigated by means of DSC, differential scanning calorimetry. However, it did not reveal any distinctive features, i.e. no T_g could be determined in the range from −90 °C to 300 °C. The glass transition may be almost invisible if it is too broad or does not absorb a significant amount of heat easily detectable by DSC.

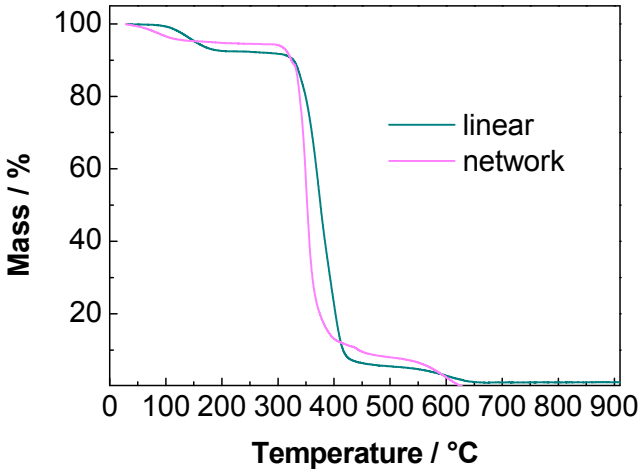

Figure 39. Thermogravimetric analysis diagram measured under nitrogen flow for linear betulin-TPC polymer (dark cyan) and a network (magenta).

The gas adsorption was investigated on both precipitated and cast samples. Furthermore, the apparent single gas selectivity of the gas pair CO_2/N_2 was calculated. Nitrogen sorption at 77 K (not shown here) indicated the absence of pronounced microporosity. In some cases, a strong hysteresis was observed upon desorption, which is actually a common feature of microporous polymers. However, all samples were able to take up CO_2 at 273 K, see upper curves in Figure 40. There was a remarkable difference between the cast films and the precipitated powders. The denser systems (films) featured hysteresis upon

desorption, whereas this was not observed for the powders. CO_2 capacity between 0.8 and 1 mmol·g^{-1} was comparable for cast and precipitated materials with the tendency of slightly higher uptake of the latter. In case of nitrogen uptake at 273 K, significant differences were observed between cast and precipitated samples. This can be explained by a less dense packing, which allows nitrogen to access the narrow pores easily.[49]

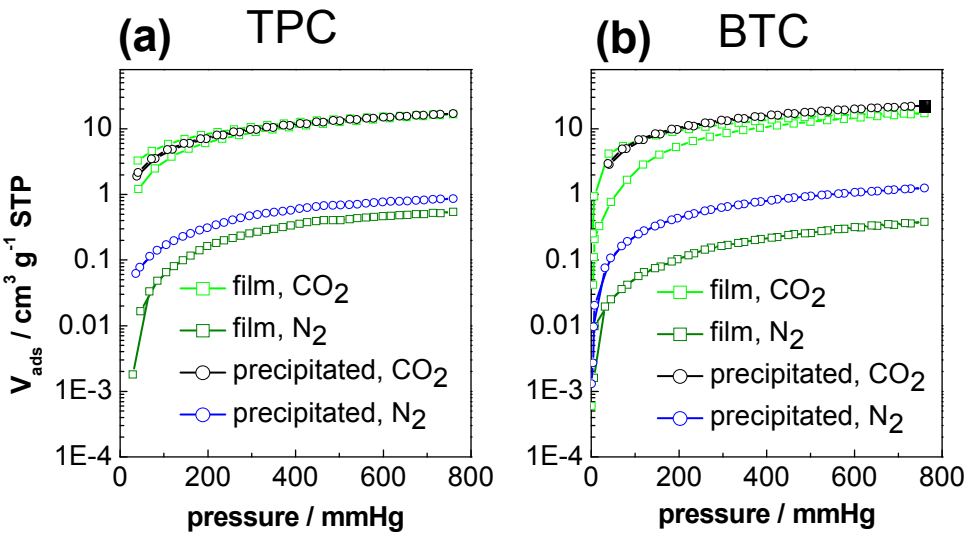

Figure 40. CO_2 and N_2 adsorption/desorption isotherms (273 K) of (a) betulin-TPC and (b) betulin-BTC polymers.

Consequently, high apparent CO_2 over N_2 selectivity (1 bar, 273 K) resulted for cast compared to precipitated samples, see Table 4-5. Selectivity of around 30-45 are within and even above the range, which was lately discussed for polymer membranes with CO_2 capture applications.[144,145]

Table 4-5. CO_2 over N_2 selectivities at 1 bar and 273 K for precipitated and cast samples of betulin-TPC and betulin-BTC polymers, as well as the evaporative and freeze-dried networks.

	Betulin-TPC	betulin-BTC	evap. dried	freeze-dried
Precipitate	20	18		
Film	31	45		
Network			47	27

It is highly probable that betulin polyesters have promising potential in those applications because they are based on renewable resource (total content of more than 77 wt.%).

The CO_2 over N_2 selectivities of the soluble polymers are comparable to those of the networks. It is evident that the highest selectivities were achieved for films in general and the evaporative dried network sample. This is mostly due to the restricted ability of nitrogen molecules to adsorb on a denser material and a common feature of all discussed materials to adsorb similar amounts of CO_2.

The selectivity calculated from the adsorption of pure gases at 1 bar is of course not the decisive factor for the future membrane performance. Also, high-pressure measurements are required for industrial applications of gas separation.

4.3 Other polymers

4.3.1 Polyurethanes

Conventional polyurethane synthesis involves a polyaddition reaction of diols with diisocyanates. Polyurethanes have already been synthesised from renewable reactants, e.g. from lignin.[146] Betulin-based polyurethanes have been reported previously. Linear polyurethanes from betulin and commercially available linear extended aromatic polyisocyanates Desmodur E 22 (solution of multi-block copolymer of diphenylmethane-*p,p'*-diisocyanate and dipropylene glycol ether) were synthesised as early as the 1980s.[147] Also, polyurethane films were prepared from betulin esters of fatty acids and Desmodur N (solvent-free aliphatic polyisocyanate resin based on hexamethylene diisocyanates).[148]

After successful reactions of betulin with trifunctional acid chloride resulting in microporous polyester networks, it was plausible to assume that betulin could also form microporous polyurethane networks.

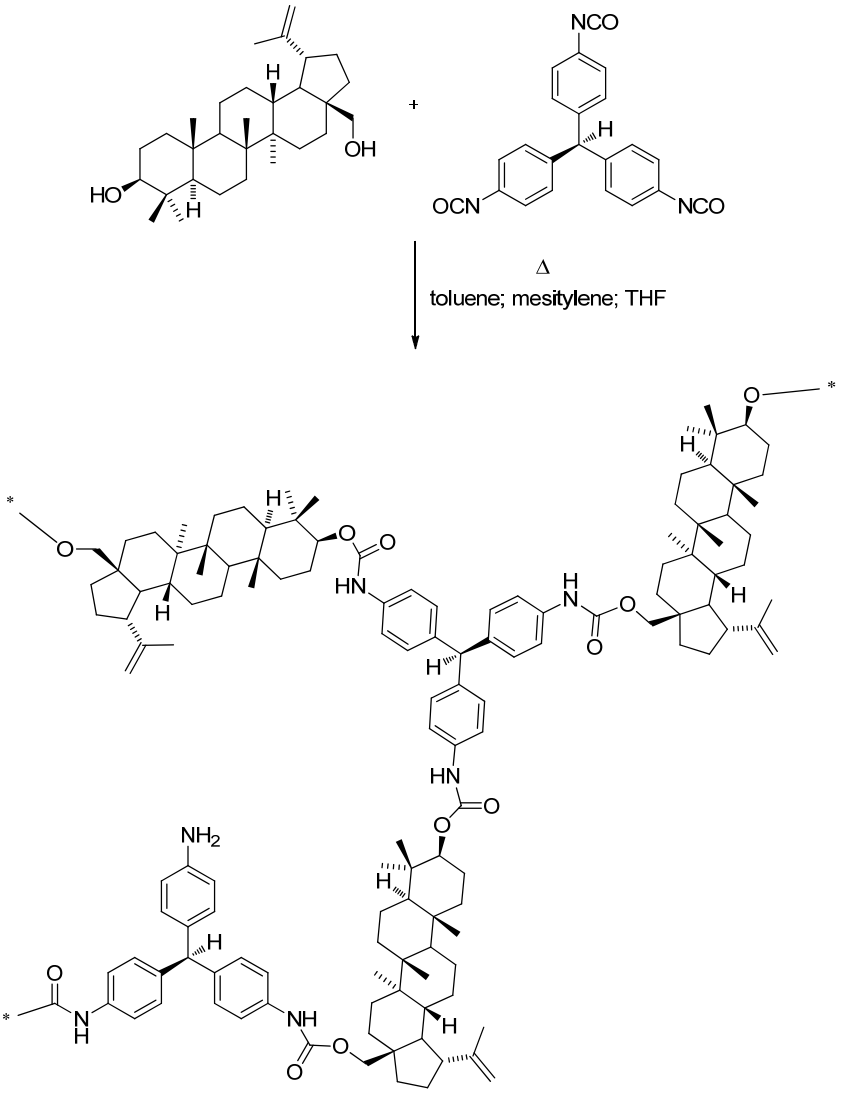

Figure 41. Reaction scheme for polyurethane formation from betulin and triphenylmethante-4,4',4''-triisocyanate. The product structure is a segment of one of the possible linkages.

Especially introducing another sterically hindered monomer, triphenylmethane-4,4',4''-triisocyanate (Figure 41), one could expect a microporous structure. The triisocyanate was used as a 20% solution in EtOAc, provided by Bayer (Desmodur RE®).

The synthesis was carried out in different conditions in each THF, mesitylene and toluene at the respective boiling point of the solvent. With optimum reaction conditions (T = 160 °C), the reaction was accomplished in several minutes in

mesitylene (T_b = 164.7 °C). The ideal composition of the network (betulin:triisocyanate, 3:2) would imply that the renewable resource is represented with 64%. Solid state NMR data shown in Figure 42 and Figure 43 was collected for ^{1}H, ^{15}N and ^{13}C nuclei.

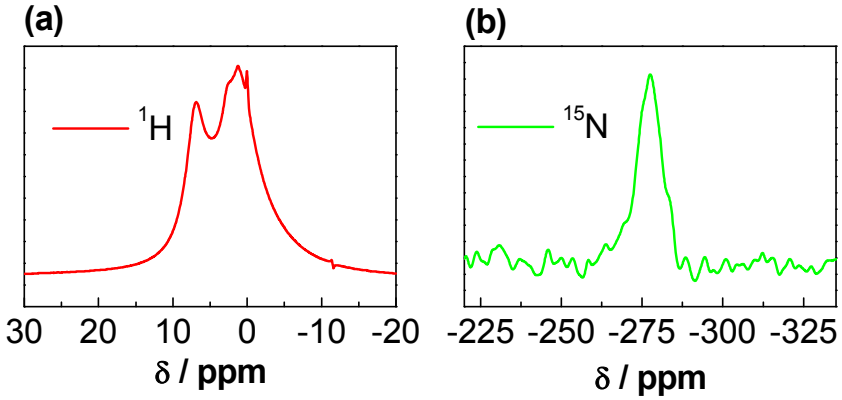

Figure 42. (a) ^{1}H-NMR and (b) ^{15}N-NMR spectra of a polyurethane network prepared from betulin and Desmodur Re®.

The ^{1}H-NMR delivered a typical spectrum measured in solid state with broad signals, distinguishable for aromatic (δ ≈ 6.4 ppm) and aliphatic (δ ≈ 1.2 ppm) protons.

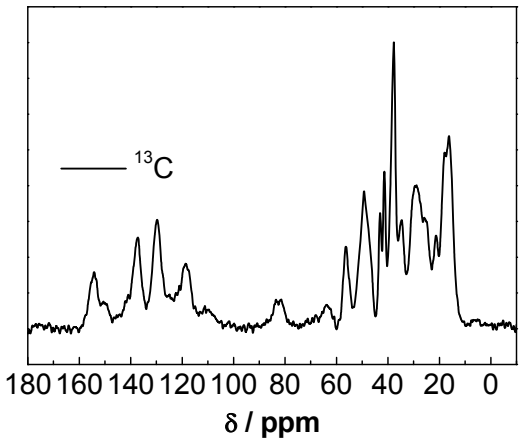

Figure 43. Solid state NMR spectrum of a polyurethane network prepared from betulin and Desmodur Re®.

The ^{13}C spectrum confirmed the formation of the urethane linkage (δ = 154.3 ppm). The neighbouring peak at 150.8 ppm can be designated to the 20-C at the double bond (see Figure 5 for atom numbering). Apart from aromatic C-atoms of triphenylmethane-4,4',4''-triisocyanate between ca. 110 ppm and 140 ppm and aliphatic C-atoms of betulin, the signals of oxygen-bearing C-atoms of betulin (3-C, 28-C) can be distinguished at 82.2 ppm and 63.8 ppm.

The most interesting measurement from the analytical point of view is the ^{15}N-NMR, which is difficult to obtain due to the low natural occurrence of the ^{15}N isotope (0.37%).[134] Without the ^{15}N-enrichment of the sample, even with large sample mass, strong magnetic fields and long accumulation time do not often reveal good interpretable data. This is why this spectrum was obtained only after an over-night measurement. The anisotropic broadened signal in ^{15}N-spectrum in Figure 42b indicates that the chemical environment of the nitrogen in the urethane linkage is not homogenous and that hydrogen bonds are possibly present. It can also be speculated that aside from that, some of the common side products in the polyurethane synthesis (e.g. urea, biuret) are present.

Formation of a polyurethane was also confirmed by IR analysis shown in Figure 44a. Diminishing signal of the hydroxyl groups at 3370 cm^{-1} and appearing carbonyl band at 1709 cm^{-1} and –NH bending stretch at 1592 cm^{-1} indicate a successful formation of a polyurethane –NH-COO linkage.

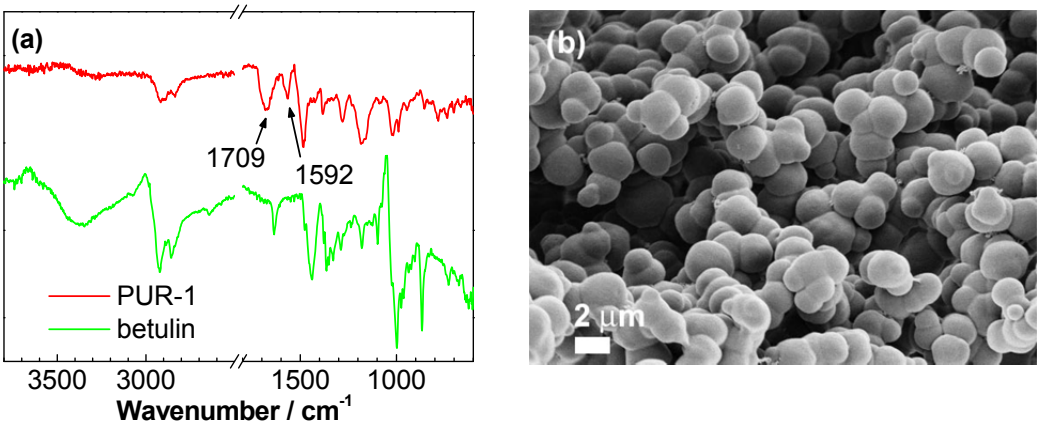

Figure 44. (a) IR spectra of betulin (green) and a polyurethane network *PUR-1*; (b) SEM image of *PUR-1*.

The relatively broad carbonyl signal at 1709 cm^{-1} can be an indicator of an overlay of two carbonyl containing compounds: the desired urethane group and the product of a side reaction, a urea linkage, see Figure 45.

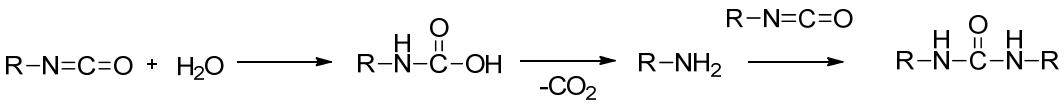

Figure 45. Side reaction occurring during polyurethane synthesis: isocyanate reacting with water is forming a urea via an amine intermediate.

The broad signal in ^{13}C-NMR between 150 ppm and 155 ppm can also be designated not only to the signals described above, but also to an eventual urea carbonyl.

A SEM image of a typical network is presented in Figure 44b. It does not expose any porous structure like that of the polyester network (Figure 17a) but rather a well-defined microstructure of interconnected microglobules.[149] Nitrogen adsorption isotherms collected at 77 K were indicative of a typical non-porous material. Unlike with polyesters, freeze-drying from dioxane did not result in a porous structure, as indicated by nitrogen sorption (Figure 46).

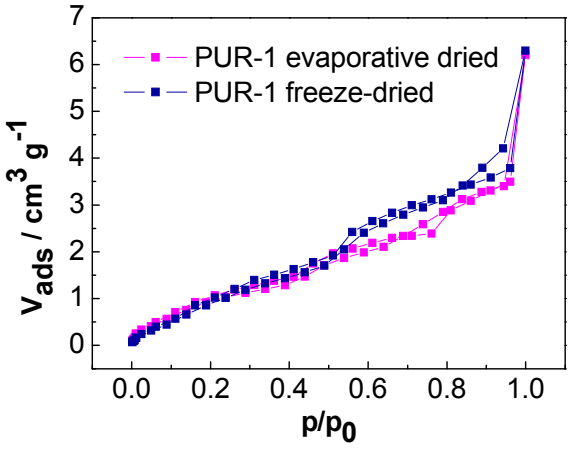

Figure 46. N_2 sorption at 77 K of PUR-1 evaporative dried (magenta) and freeze-dried (dark blue).

It can be speculated that the presence of the hydrogen bonds is responsible for that. Similar observations were made for carboxylated *PIM-1* polymers.[34] Containing acid groups and hydrogen bonds, they did not take up any nitrogen at 77 K, unlike their unhydrolysed precursors.

CO_2 uptake at 273 K was, however, comparable to the polyester networks (Figure 47a, Figure 16b), although the isosteric heats of adsorptions (Figure 47b) offered a suggestion of weaker polyurethane-CO_2 interactions.

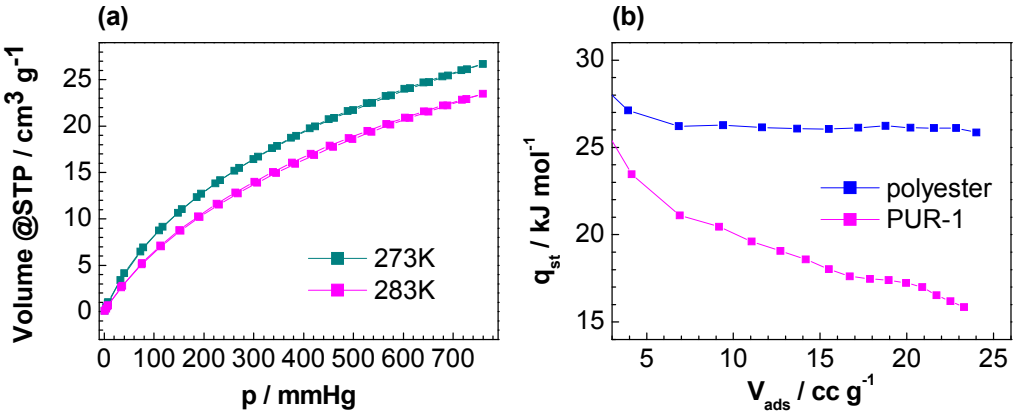

Figure 47. (a) CO_2 sorption at 273 K and 283 K of *PUR-1*; (b) isosteric heats of adsorption of *PUR-1* (magenta) and freeze-dried polyester network (from Figure 20b) calculated from CO_2 adsorption measurements at 273 K and 283 K.

This was also in accordance with the data obtained from ^{13}C-NMR of the sample loaded with $^{13}CO_2$, see Figure 48. The sharp distinct signal at $\delta \approx 123$ ppm belongs to free CO_2 (the broad signal at $\delta \approx 109$ ppm is originating from the Teflon sample holder). One could speculate that if some of the initial isocyanate groups hydrolyse and build amines, these CO_2-affine amines could incorporate $^{13}CO_2$ to some extent and form carbamates. However, no other signal was detected.

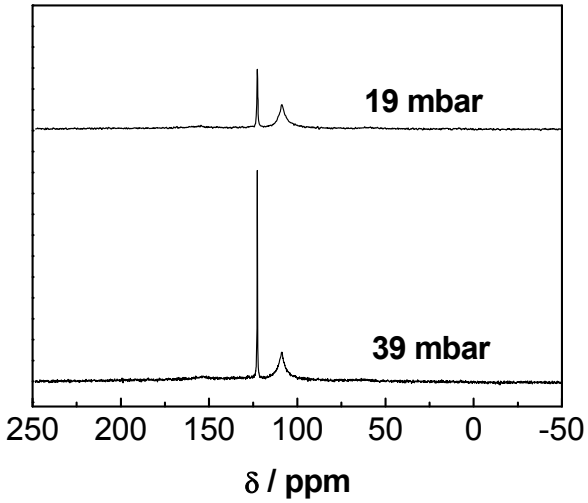

Figure 48. ^{13}C-NMR spectrum of PUR-1, loaded with $^{13}CO_2$.

As chemisorption typically occurs at low pressures and no other signal was detected under the utilised experimental conditions (at 19 mbar and 39 mbar), it can be concluded that CO_2 is rather free-moving and thus only physisorption takes place.

The distinctive structure of microglobules has triggered the attempt to prepare a polyurethane monolith. THF was chosen as a solvent for this experiment for the reason of higher betulin solubility.

Figure 49. *PUR-2*, polyurethane obtained in a Schlenk flask by reaction in THF without stirring.

The reaction was stopped after several days when the product appeared to have densified. Washing and consequent drying lead to a dark purple, vessel-shaped product. The rupture of the product stick was probably caused by arising surface tension during solvent exchange and drying, see Figure 49. This however can be evaded in future investigations using defined drying protocols.

The purple colour of the product can be explained by the presence of impurities in the starting compound Desmodur RE®, which is a dark-purple solution. The structure of its main component is based on triphenylmethane. Combined with substituents with *+M*-effect (e.g. amine groups), it represents a scaffold for widely-used commercial dyes, see Figure 50.

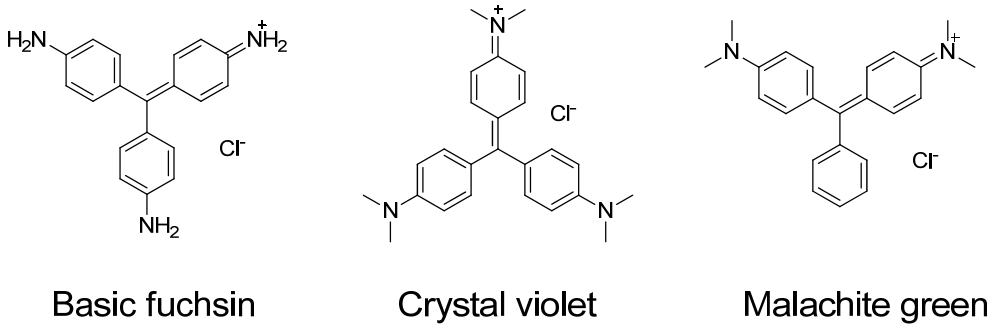

Figure 50. Chemical structure of three common dyes which can be present as impurities in Desmodur RE®.

These compounds are permanent companions of the industrial chemical Desmodur RE®, which when present in traces, can alter its colour dramatically though not affecting its bulk chemical properties.

This and other experiments (not presented here) have shown that this can be a promising approach in attempt to prepare a monolith. Of course, more research is required to prepare a betulin-based polyurethane monolith, but this can be seen as outlook and potential direction for further investigations.

4.3.2 PEO-containing polymers

Betulin, a naturally-occurring triterpene, has already been described as an easily extractable renewable resource. In this work, it has been used for the preparation of novel microporous polyester networks, soluble polyesters and polyurethanes. Owing to its double functionality, it can be utilised as a diverse reagent in preparation of further substances.

Macromolecules containing synthetic polymers and biological components are often referred to as polymer bioconjugates. They have been one of the most popular topics in polymer science and biochemistry.[150,151] Great potential is open for advanced polymer materials bearing combined adjustable properties of the synthetic component and the characteristic features of the biological component. Among other polymers, poly(ethylene oxide) (PEO) has been the most widely utilised synthetic polymer by virtue of its biocompatibility, hydrophilicity and nontoxicity.[152] It has been coupled with polysaccharides, peptides and other bioactive compounds and extensively investigated.[153–155] Betulin-PEO conjugates have also been reported recently.[21,156] Zhao *et al.*[21] have studied PEO-terpene conjugates prepared by metal-free anionic ring-opening polymerisation. The betulin-PEO conjugate with PEO weight% of 68% and 82% were synthesised with expected low polydispersity. The differential scanning calorimetry revealed glass transition and melting temperatures, but no liquid crystal transition as with cholesterol-PEO conjugate. It has been revealed that the properties of polymer conjugates based on other analogous natural terpenes (e.g. cholesterol and bile acids) depend greatly, among others, on the molecular architecture.[157] Inspired by the bifunctionality of betulin-PEO conjugate (**6**, Figure 51), it was intended to turn it into a multiblock-like molecular structure by utilising facile polycondensation and further compare the properties of betulin-PEO conjugate and the multiblock.

The betulin-PEO conjugates (supplied by Junpeng Zhao) were modified with [1,1'-biphenyl]-4,4'-dicarbonyl dichloride, terephthalic, isophthalic and adipic acid

chlorides, see Figure 33. Highly viscous yellowish liquids were obtained after the reaction of solid betulin-PEO conjugate with corresponding diacid dichlorides.

Betulin-PEO-TPA (reaction scheme in Figure 51) was chosen as a model compound due to good conversions and narrow molecular weight distribution; see Table 4-6 and Figure 52. The betulin-PEO conjugate with longer chain is denoted **6a**, the one with the shorter PEO-chain – **6b**. The products of their reaction with TPC are named **7a** and **7b**, respectively.

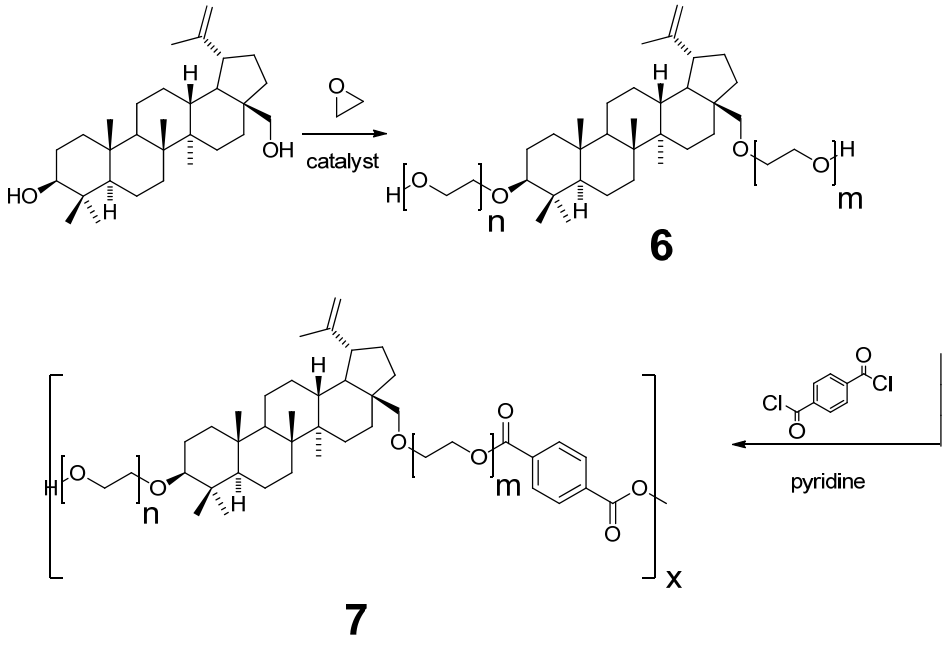

Figure 51. Reaction path for the synthesis of betulin-PEO conjugate **6** and betulin-PEO-TPA **7** from betulin.

Although both betulin-PEO conjugates were highly soluble in water, all the betulin-PEO-TPA polymers exhibited rather low solubility. Possibly the aromatic linkages of TPA have exerted enough hydrophobicity to diminish hydration.

Table 4-6. Molecular weight overview, PEO weight fraction and degree of crystallinity of betulin-PEO conjugates **6a** and **6b** and their coupling products with TPC, **7a** and **7b**, respectively. GPC in THF, PEO-calibration. The molecular weights for **7b** are given for the polymer, fractionated from chloroform and hexane.

	6a	**7a**	**6b**	**7b**
$M_{n,\,SEC}$ / g·mol^{-1}	$3.03\cdot10^3$	$1.63\cdot10^4$	$1.87\cdot10^3$	$1.66\cdot10^4$
$M_{w\,,SEC}$ / g·mol^{-1}	$3.29\cdot10^3$	$2.36\cdot10^4$	$1.96\cdot10^3$	$6.04\cdot10^4$
MALDI-TOF, M_n	$2.49\cdot10^3$	n.d.	$1.76\cdot10^3$	n.d.
w_{PEO} [a]	0.82	0.78	0.75	0.70
$X_{c,\,PEO}$/% [b]	69.8	33.1	54.1	22.8 [c]

[a]PEO weight fraction, as calculated from MALDI-TOF MS data for **6a** and **6b**; for **7a** and **7b**: M_n(PEO)/(M_n(**6**)+132) with contribution of 132 g·mol^{-1} from TPC assuming the ratio of betulin-PEO and TPA moieties in the polycondensation product is stoichiometrically 1:1; [b]crystallinity of PEO, as determined by DSC; calculated as the ratio of measured melting enthalpy per gram of PEO to the heat fusion of a 100% crystalline PEO, 200 J·g^{-1}.[21,158] [c] Cold crystallisation in the heating process.

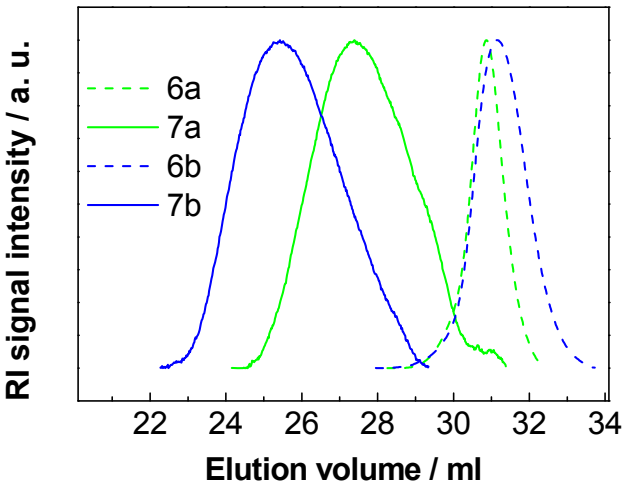

Figure 52. Normalised GPC curves of betulin-PEO conjugates (**6a**, **6b**) and their products with TPC (**7a**, **7b**).

The starting substance **6a** showed a crystallisation peak, T_c, upon cooling at 14 °C and a melting peak, T_m, upon heating at 41 °C (Figure 53a, dash-dot), whereas **6b** with shorter PEO-chains showed T_c of 6 °C and T_m of 37 °C, respectively (Figure 53b, dash-dot). Hence, the betulin-PEO with higher PEO-content is more

favourable for crystallisation. It crystallizes better because the longer PEO-chains can modify their conformation and order themselves more freely than the shorter ones, which in turn are more constrained from both termini. Introducing ester linkages of terephthalic acid changes the thermal behaviour radically.

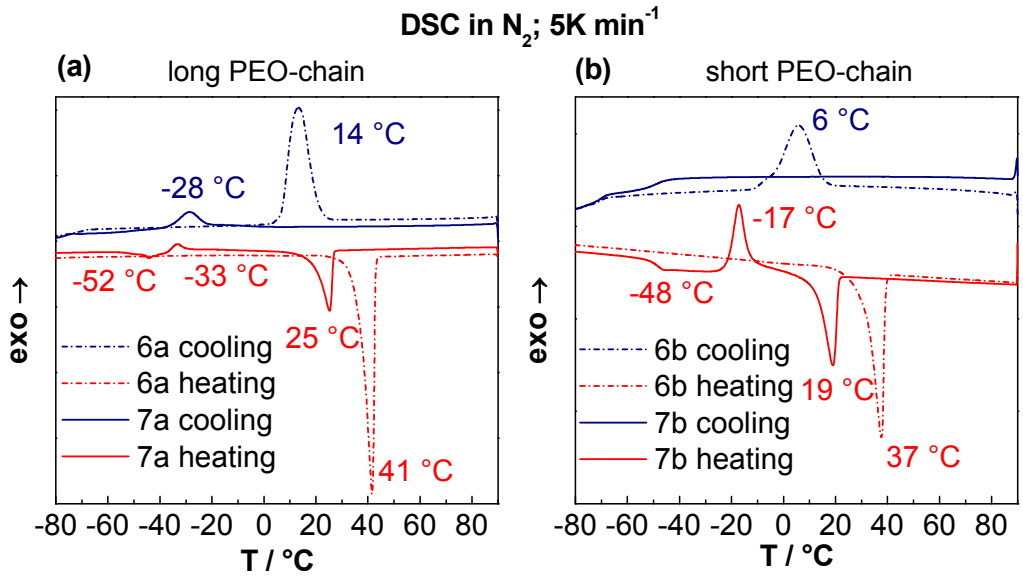

Figure 53. DSC curves of (a) long- and (b) short-chain betulin-PEO-TPA polymer (see Table 4-6 for molecular weight).

7a, prepared from the longer-chained reagent **6a,** exhibits a decrease in crystallisation (14 °C → −28 °C) and melting (41 °C → 25 °C) temperatures. The degree of crystallinity calculated from the melting peak decreases dramatically from 69.8% to 33.1%. Due to such a low crystallinity, the glass transition of ***7a*** was detected in the heating curve, with a glass transition temperature, T_g, being −52 °C. Unlike its precursor **6b**, the multiblock **7b** (with shorter PEO-chains compared to **6b**) displayed no crystallisation peak in the cooling curve. A glass transition (T_g = −48 °C), a cold crystallisation peak (−17 °C) followed by a melting peak (19 °C) were clearly observed in the heating curve, which is the typical thermal property for semicrystalline polymers. It is obvious that the introduction of terephthalic acid moieties to connect the individual betulin-PEO

macromolecules brings in a stiff element in the chain and causes some loss of the degree of freedom of PEO chains, which reduces the PEO ability to crystallize.

The stiff betulin moieties with flexible chain in between could also bring in the required objects for a liquid crystalline structure. This assumption was probed by means of SAXS on betulin-PEO and betulin-PEO-TPA polymers, see Figure 54.

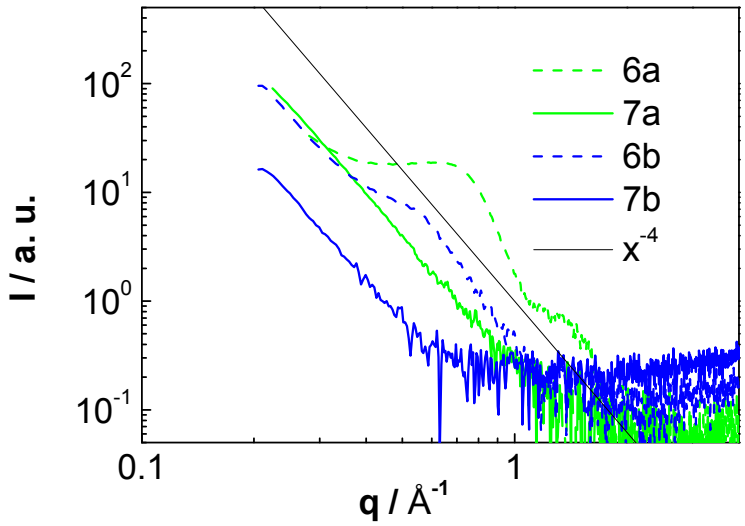

Figure 54. SAXS patterns of betulin-PEO conjugates (**6a**, **6b**) and their products with TPC (**7a**, **7b**).

The collected curves show that whatever ordered state of the initial betulin-PEO conjugates **6a** and **6b** has existed, the introduction of TPA-linkages destroys it. The periodic character is more pronounced in longer-chained **6a** comparing to **6b**. This is associated with the better capability of the longer chains to access the more energetic favourable confirmation discussed above. Connecting the betulin-PEO conjugates via TPA results in decreased intensity and straightening of the curve on the double logarithmic plot. Cooling down the **7b** in an attempt to lock down the thermal movement, which could distort the eventual two phases of stacked ordered betulin unities and flexible PEO-chains, could not be experimentally achieved. Apparently, the betulin moieties are too short and the PEO-chains too long to give rise to ordered liquid crystalline structure.

Though the betulin-PEOs (**6a, 6b**) had high water solubility, neither of the betulin-PEO-TPA multiblocks (**7a, 7b**) could be directly dissolved in water. This may be due to the increased hydrophobic content introduced by the aromatic linkages of TPA. However, based on the weight fraction of PEO in each sample (w_{PEO}, Table 4-6), this does not seem to be the case, since w_{PEO} is reduced by merely ≤ 5% and the comparison of **6b** (w_{PEO} = 75 %) and **7a** (w_{PEO} = 78 %) can also lead to such a conclusion. Furthermore, there is another betulin-PEO sample (**6c**, not shown) which has the lowest w_{PEO} (68 %) of all and still hold very good water solubility at room temperature. Therefore, the most possible explanation should be the different hydration ability between the betulin-PEO conjugates and the polycondensation product (multiblock), namely, the loss of PEO free chain ends leads to the significantly reduction of hydration of the PEO chains.

The aqueous solution behaviour of the betulin-PEO conjugates and their polycondensation products was investigated by light scattering. The betulin-PEO conjugates **6a** and **6b** were readily soluble in water. Both of them showed bimodal hydrodynamic radius (R_h) distributions (see Figure 55a for **6a**), with a small species located at ca. 3 nm and a large species at > 100 nm. The large species can be some loose and highly hydrated aggregates, which however, should be much less in number and mass compared to the small species and contribute very little to the property of the solution. It is still difficult to make the judgement if the small species is betulin-PEO unimers or small micellar aggregates, but it is obviously the dominant component of the solution.

As mentioned above, the polycondensation products **7a** and **7b**, unlike their precursors, were not readily soluble in water. The loss of water solubility must be related to the reduced hydration of those *α*-, *ω*-tethered PEO chains and the additional hydrophobicity introduced by the TPA linkages. Nevertheless, by adding water slowly to their THF solution, followed by evaporating THF under reduced pressure and compensating the water loss, it was possible to obtain their aqueous solution with the desired concentration (< 0.1 wt.%).

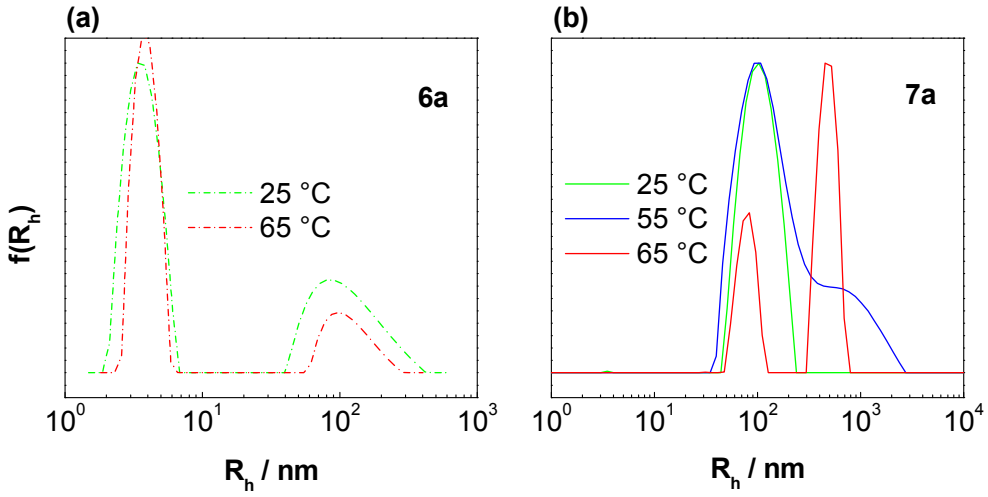

Figure 55. Hydrodynamic radius ($R_{h;}$ CONTIN method) distribution at 90 ° for (a) **6a** (0.1 wt.%) and (b) **7a** (0.06 wt.%).

Light scattering measurements showed distinct aggregates in a range from 25 °C to 65 °C. Heating resulted in gradual growth of aggregates, see example of **7a** in Figure 55b. At 25 °C (green curve) the average aggregate size is ca. 103 nm. With increasing temperature larger aggregates are beginning to form (blue curve) and they grow on until an average size of ca. 480 nm at the expense of the smaller ones (red curve).

Temperature dependence of R_h of **7a** and **7b** is presented in Figure 56a. Figure 56b gives complement information on the thermal behaviour of **7a** in water. According to turbidity measurements, the sample begins to precipitate at around 53 °C, whereas the process of aggregates growing can be observed via more sensitive light scattering method already starting from 40 °C. The aggregates of the shorter-PEO-chained **7b** also enlarge, however, not to the same extent. This could be explained by its greater hydrophobicity.

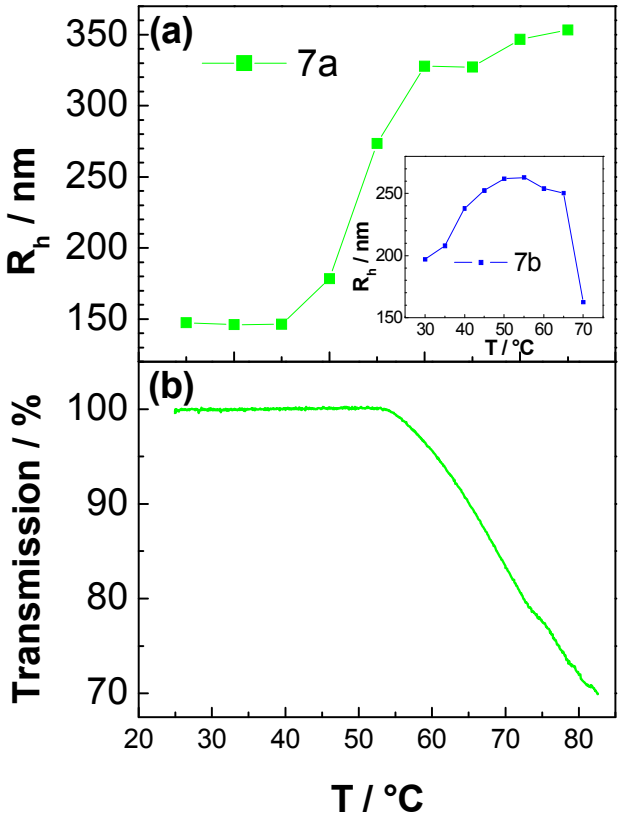

Figure 56. Temperature dependence of (a) R_h (cumulant fit) at 30 ° for **7a** (0.06 wt.% in water) and **7b** (0.04 wt.% in water); (b) turbidity measurements of the same sample of **7a**, heating rate 1 K·min^{-1}.

For clarity reasons, the results of DLS measurements for betulin-PEO conjugates and their products with TPC are shown in Figure 57 for several temperatures. The former ones do not form aggregates even after heating, with the DLS signal almost identical at 25 °C (or 30 °C) and 65 °C (dash-dotted lines). The aggregates of the longer PEO-chained **7a** (green solid line) change from ca. 100 nm at 25 °C to a bimodal distribution of 490 nm and 80 nm at 65 °C. A similar behaviour is displayed by the shorter PEO-chained **7b** (blue solid line), featuring aggregates of 131 nm at 30 °C and 250 nm and 65 nm at 65 °C. The less pronounced change of the latter is probably also explained by its hydrophobicity. The more hydrophobic multiblock polymer exhibits slighter variation in temperature dependent aggregation. It should be noted that the concentrations

of **7a** and **7b** needed to be adjusted for the DLS measurements because of their poor solubility in water.

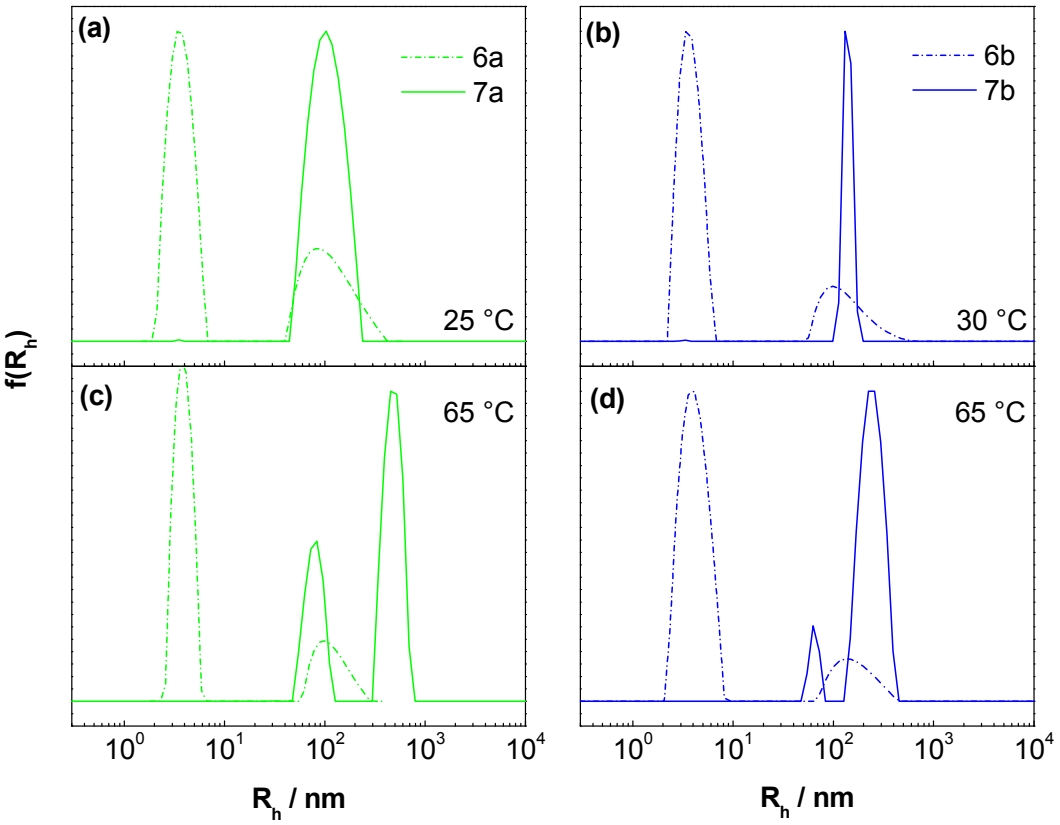

Figure 57. Hydrodynamic radius (R_h; CONTIN method) distribution at 90° for **6a** (0.1 wt.%) and **7a** (0.06 wt.%) at (a) 25 °C and (c) 65 °C and **6b** (0.1 wt.%) and **7b** (0.04 wt.%) at (b) 30 °C and (d) 65 °C.

It was shown that betulin-PEO conjugates are well soluble in water and do not form aggregates at low concentrations independently of temperature between 25 °C and 65 °C. The PEO-chains of lengths used in **6a** and **6b** are apparently both long enough to provide for the hydrophilicity of the compound. The hydrophobic betulin entity in the molecule is probably insufficient to trigger profound aggregation in water even at high temperature. However, allowing reaction of these conjugates with TPC provides a method to receive more hydrophobic biohybrid multiblock polymers which are poorly soluble in water.

Their aggregates formed at low concentrations in water showed the tendency of increasing in size with rising temperature.

These results clearly show that the free PEO chain ends play an important role in the physical properties (crystallisation, hydration) of betulin-PEO conjugates with different molecular structures. The loss of free PEO chain ends due to the polycondensation not only reduces the crystallinity but also diminishes the hydration and overall hydrophilicity of the conjugate. Therefore, these results provide important information for sophisticated bioconjugates polymer design based on structure-properties relationship. Certainly, there are additional studies required, but this can also be considered as an example of a further alternative for the potential use of betulin in biohybrid polymers, e.g. for preparation of “renewable” surfactants or stabilisers.

5 Conclusions and Outlook

The ubiquity of betulin as a byproduct of the wood industry reveals a great potential for developing new materials for various applications. Microporous polyester networks and soluble polymers from betulin, an abundant natural product, were synthesised and analysed with respect to their microstructure. For the first time, the microstructure of microporous polyester has been thoroughly investigated. The studies have been performed in detail with a model system, intending to comprehend the inherent nature of the subject.

The class of the microporous polymers based on aromatic monomers, such as PIMs, COFs, HCPs, aromatic microporous polyimides and polyarylate esters has been extended and now comprises microporous polyesters from an abundant natural resource. A simple preparation method, which did not include any tedious multistage synthesis of individual monomers, has been introduced to obtain this result.

The novel microporous polyester networks with ca. 78 wt.% of natural resource have been analysed in detail with respect to their porous microstructure. The combination of gas adsorption measurements of various adsorbates at different temperatures proved that nitrogen adsorption at 77 K, being the most used technique for analysing the structure of a porous material, is not to be blindly relied upon when applied to microporous materials. It has been groundbreakingly shown that nitrogen adsorption at 87 K can be a better method to solve the microstructure of the material. It has also been established that most standard sorption measurements on microporous materials are probably conducted in non-genuine equilibrium and therefore the pore size distributions and the pore volume derived from those measurements are imperfect. Thus, it is essential to develop new theoretical models in order to achieve and proceed the correct data about the micropores.

The idea of utilising the ultrasmall pores for applications emerged after having found and investigated the microstructure of the insoluble polyester network. Soluble and, thus, processable polyesters with high potential for selective gas adsorption for membrane applications have been synthesised. Consisting of ca. 77 wt.% natural resource and exhibiting high CO_2/N_2 selectivities, these polymers have delivered promising results when tested in gas permeation experiments. It has already been possible to achieve transparent homogeneous films by simple casting. Further films may be prepared via spin-coating technique and subsequently be analysed in gas permeation using different moduli of mixed gas flow.

Besides utilising betulin for preparation of soluble and insoluble polyesters, its potential as a monomer for diverse polymers has been presented as well. Polyurethane networks have been synthesised from commercially available triisocyanate. A foundation for preparation of monoliths based on betulin has been introduced. Moreover, betulin-PEO biohybrid polymer conjugates and their temperature-responsive behaviour of self-assembly in water is presented in this work. This may be the first step on the way of preparation of new classes of "renewable" surfactants and stabilizers.

All in all, it can be concluded that betulin shows a huge potential in polymer synthesis. This aspect of scientific interest might have been stagnated since the early reports in the 1980s because much research is nowadays rather directed towards the synthesis of betulin-derivatives for medical purposes. In this work, betulin, as a starting compound for polyester synthesis, has aided to prepare, and for the first time to thoroughly analyse microporous polyester with respect to its pores and microstructure. In my opinion, betulin, as an easily extractable natural resource, should experience its rebirth in polymer science.

6 Appendix

6.1 Experimental

Extraction of birch bark

Birch bark from *Betula pendula* was dried at 40 °C *in vacuo* and cut into small pieces. 3.93 g were extracted with dichlormethane for 24 h. After evaporating the solvent and drying at 40 °C in vacuo 1.46 g (37% from dried weight) of a light yellowish powder was obtained. The crude extract was recrystallised from ethanol and dried *in vacuo* at 140 °C to remove the ethanol from the solvate.

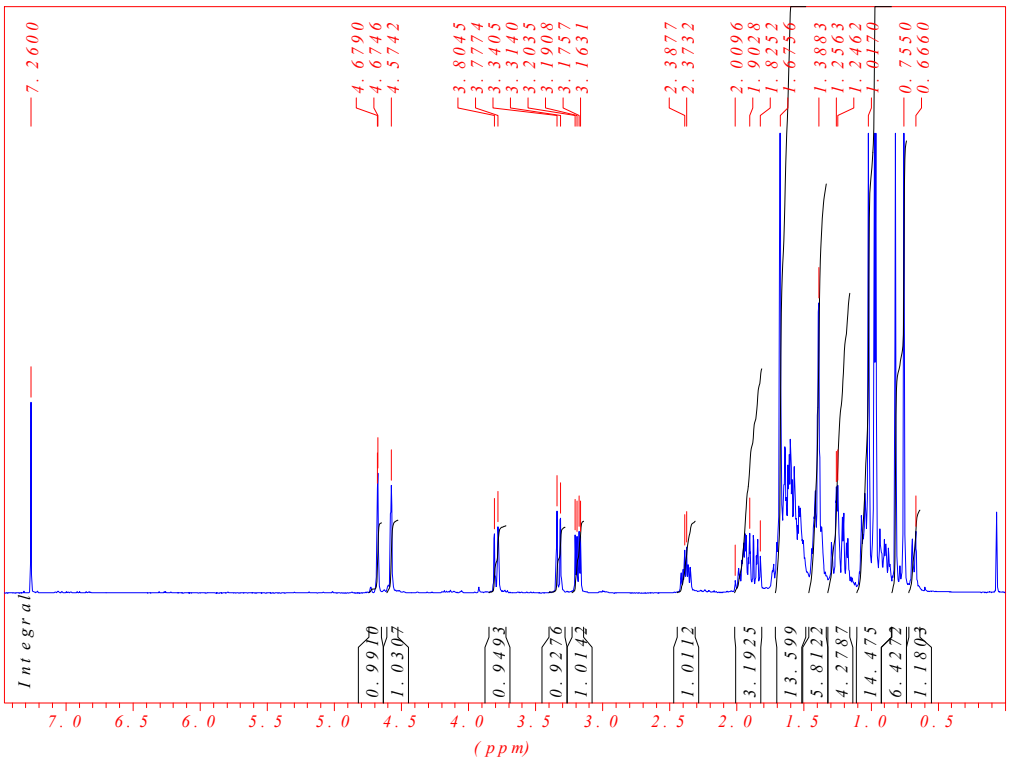

Figure 58. ^{1}H-NMR spectrum of betulin obtained from birch bark and recrystallised from ethanol.

^{1}H-NMR: 400 MHz, $CDCl_3$; δ / ppm = 4.68 (s, 1H, 29a-H), 4.57 (s, 1H, 29b-H), 3.78 (d, 1H, 28a-H), 3.32 (d, 1H, 28b-H), 3.17 (dd, 1H, 3-H), 2.37 (m, 1H, 19-H), 1.9 (m, 3H, 30-H), 1.67-0.66 (m, 40H).

IR: ATR; ν / cm^{-1} = 3360 br, s (O-H), 3080 w (C_{sp2}-H), 2930 s (C_{sp3}-H), 2865 s (C_{sp3}-H), 1644 w (C=C), 1450 s, 1375 s, 1300 w, 1185 m, 1105 m, 1025 s (C-O), 880 s.

Example of a polyester network synthesis

The crude birch bark extract (1.0 g, <2.2 mmol) was stirred with 1,3,5-benzenetricarbonyl trichloride (374 mg, 1.4 mmol) in dry degassed THF. 2.0 ml (24.7 mmol) dry pyridine was added through a syringe and the mixture immediately turned turbid. After refluxing for ca. 20 h a gelatinous precipitate was formed. It was washed with 1M HCl solution, water, THF and dioxane. The resulting gel was either dried *in vacuo* at 50 °C, or swollen in dioxane and freeze-dried to give a white powder with a slight yellow stain: Total yield 688 mg. Typical yield in %, 90-100. Found: C, 75.5; H, 8.85; N, 0.0.

IR: ATR; ν / cm^{-1} = 3070 w (C_{sp2}-H), 2940 s (C_{sp3}-H), 2870 m (C_{sp3}-H), 1725 s (C=O), 1644 w (C=C), 1450 s, 1375 m, 1320 w, 1228 s (C-O), 1145 m, 1107 m, 974 s, 883 m, 740 s, 714 m, 670 m.

^{13}C-NMR: 100.6 MHz; δ / ppm = 164 (C=O), 135-126 (C_{ar}), 100 (29-C, betulin), 88 (3-C, betulin), 69 (28-C, betulin), 57-5 (C_{sp3}); see Figure 11.

Modification of the network in basic and acidic conditions

431 mg of a polyester network were let to swell in 6 ml THF for 15 min. 6 ml of 1M NaOH solution were added and the mixture was stirred for another 10 min. After washing the gel with water, the solvent was exchanged to dioxane and the gel was freeze-dried.

IR: KBr-pellet; ν / cm^{-1} = 3420 br, s (O-H), 3075 m (C_{sp2}-H), 2950 s (C_{sp3}-H), 2872 m (C_{sp3}-H), 1730 s (C=O), 1620 s (COO^-, antisym.), 1576 s (COO^-, antisym.), 1454 s (C_{ar}- C_{ar}), 1390 s, 1317 m (COO^-,

sym.), 1300 m (COO^-, sym.), 1232 s (C-O), 1153 m, 1103 m, 974 s, 881 m, 804 w, 746 m, 714 m.

This network was subsequently washed in acidic conditions. 400 mg were swollen in 6 ml THF for 15 min and after addition of 1M HCl solution, additionally stirred for another 10 min. The gel was washed with water and dioxane and freeze-dried from dioxane.

IR: KBr-pellet; ν / cm^{-1} = 3420 br, m (O-H), 3075 m (C_{sp2}-H), 2950 s (C_{sp3}-H), 2872 s (C_{sp3}-H), 1730 s (C=O), 1645 s (C=O, H-bonds), 1606 s (C=O, H-bonds), 1454 s (C_{ar}- C_{ar}), 1390 s, 1321 m, 1232 s (C-O), 1153 m, 1103 m, 974 s, 881 m, 746 m, 714 m.

Example of a soluble betulin-TPA polyester synthesis (*S4* in Table 4-4, page 63)

The birch bark extract as obtained (270 mg, <0.6 mmol) was stirred with terephthalic acid chloride (122 mg, 0.6 mmol) in dry degassed THF. 0.48 ml (6.0 mmol) dry pyridine was added through a syringe and the mixture immediately turned turbid. After refluxing for ca. 15 h the solvent was removed under reduced pressure. The crude product was washed with 1M HCl solution and water, precipitated from ethanol and dried in vacuo at 40 °C yielding white powder with a slight yellow stain. Total yield 343 mg, 99%. Found: C, 76.5; H, 9.27; N, 0.0.

^{1}H-NMR: 400 MHz, $CDCl_3$; δ / ppm = 8.10 (s, 4H, C_{ar}-H), 4.73 (s, 1H, 29a-H), 4.62 (s, 1H, 29b-H), 4.57 (d, 1H, 28a-H), 4.12 (d, 1H, 28b-H), 2.52 (s, 1H, 19-H), 1.90-0.91 (m, 42H, C_{sp3}-H); Figure 59.

IR: ATR; ν / cm^{-1} = 3070 w (C_{sp2}-H), 2940 s (C_{sp3}-H), 2870 m (C_{sp3}-H), 1720 s (C=O), 1644 w (C=C), 1450 s, 1375 m, 1320 w, 1265 s (C-O), 1246 s (C-O), 1117 m, 1100 s, 1018 m, 968 m, 878 m, 793 w, 729 s.

GPC: in THF, PS standards; M_n = 11680 g·mol^{-1}, M_w = 41060 g·mol^{-1}, PDI = 3.5.

DSC: in the range from −90 °C to 300 °C no signal detected.

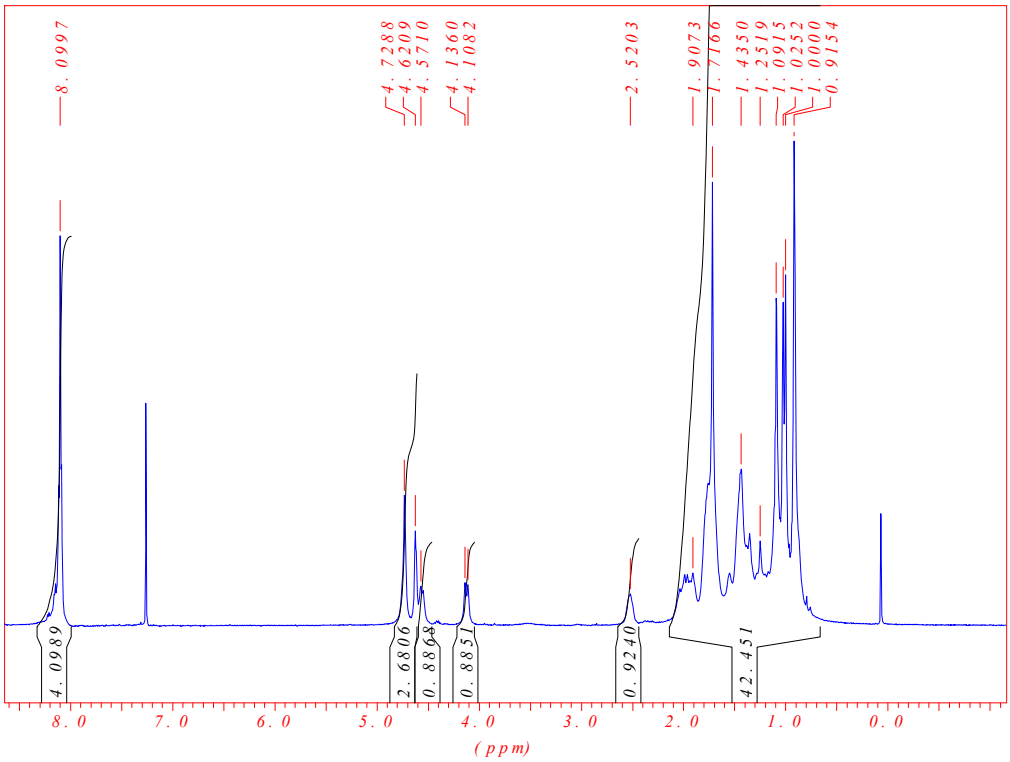

Figure 59. ^{1}H-NMR spectrum of a soluble betulin-TPA polymer.

Example of a hyperbranched polyester synthesis (*S6* in Table 4-4, page 63)

The birch bark extract, recrystallised from ethanol (491 mg, <1.1 mmol) was stirred with 1,3,5-benzenetricarbonyl trichloride (188 mg, 0.7 mmol) in dry degassed THF. 0.56 ml (6.9 mmol) dry pyridine was added through a syringe and the mixture immediately turned turbid. After refluxing for ca. 20 h the supernatant was removed. The product was washed with 1M HCl solution and water, precipitated from ethanol and dried in vacuo at 40 °C yielding white powder with a slight yellow stain. Total yield 483 mg. See Table 4-4 (page 63) for characteristics.

IR: ATR; ν / cm^{-1} = 3070 w (C_{sp2}-H), 2940 s (C_{sp3}-H), 2870 m (C_{sp3}-H), 1725 s (C=O), 1645 w (C=C), 1606 w, 1450 s, 1375 m, 1320 w, 1228 s (C-O), 1145 m, 1103 m, 1009 m, 976 s, 883 m, 804 w, 741 s, 714 s.

GPC: in THF, PS standards; M_n = 71970 $g \cdot mol^{-1}$, M_w = 287000 $g \cdot mol^{-1}$, PDI = 4.0.

DSC: in the range from −90 °C to 300 °C no signal detected.

Synthesis of a polyurethane network (*PUR-1*)

1.1 ml (297 mg, 0.8 mmol) of Desmodur RE solution was introduced to a solution of betulin (531 mg, 1.2 mmol) in 12 ml toluene at 110 °C. The mixture was refluxed for 1.5 h. Brown precipitate was formed after 15 min, gradually changing its colour to violet. The precipitate was extracted with THF in soxhlet for 20 h and dried in vacuo at 60 °C. Yield: white-rosa powder, 675 mg, 92%.

IR: ATR; ν / cm^{-1} = 3300 br (O-H), 2920 w (C_{sp3}-H), 2835 w (C_{sp3}-H), 1709 s (C=O), 1592 m (N-H), 1485 s (C=C), 1385 w, 1280 m, 1180 m, 1020 m, 990 w.

^{1}H-NMR: 400 MHz; δ / ppm = 6.8 (C_{sp2}-H), 1.2 (C_{sp3}-H), Figure 42a.

^{15}N-NMR: 40.5 MHz; δ / ppm = −277 (NH), Figure 42b.

^{13}C-NMR: 100.6 MHz; δ / ppm = 154.3 (NH-COO), 150.8 (20-C, betulin), 137.4-118.4 (C_{ar}), 110.2 (29-C), 82.2 (3-C), 63.8 (COO-*C*H_2), 56.4-16.2 (C_{sp3}), Figure 43.

Synthesis of a polyurethane monolith (*PUR-2*)

After dissolving betulin (267 mg, 0.6 mmol) in 3 ml THF at RT in a Schlenk flask, Desmodur RE solution (0.6 ml, ca. 0.44 mmol) was added and the mixture was

shortly stirred. Hereafter the stirring bar was removed and the reaction mixture was put in an oil bath at 70 °C for 7d. The resulted purple block was washed with THF and dried *in vacuo* at 60 °C, yielding 409 mg (95 wt.%).

IR: ATR; ν / cm^{-1} = 3300 br, s (O-H), 2930 s (C-H), 2860 s (C-H), 1710 s (C=O), 1595 m (C_{ar}-C_{ar}), 1515 s (C_{ar}-C_{ar}), 1454 m (C-H), 1410 m, 1305 s, 1200 s, 1040 s (C-O), 970 m, 880 m, 810 m, 760 m.

Synthesis of a betulin-PEO-TPA (**7b**)

The reaction was performed under argon atmosphere using dried solvents. 2.0 g (≈ 1.05 mmol) of betulin-PEG conjugate (M_n ≈ 1900 Da) were dissolved in 12 ml THF and 0.8 ml (9.8 mmol) pyridine to form a yellowish transparent solution. 8 ml of 0.13M TPC (1.06 mmol) solution in THF were introduced by portions of 0.5 ml and 1.0 ml within 1h. After heating at 65 °C for 23h the solvent was removed under reduced pressure from the turbid reaction mixture and the product was washed with water. The product was fractionated from 5 wt.% chloroform solution in hexane. Overall yield: highly viscous yellowish liquid, 95%.

GPC: in THF, PEO calibration; M_n = $1.66 \cdot 10^4$ $g \cdot mol^{-1}$, M_w = $6.04 \cdot 10^4$ $g \cdot mol^{-1}$, PDI = 3.6, see Table 4-6 and Figure 52.

DSC: T_g = −48 °C, T_c = −17 °C, T_m = −19 °C; Figure 53.

^{1}H-NMR: 400 MHz, $CDCl_3$; δ / ppm = 8.11 (m, 4H, C_{ar}-H), 4.67 (s, 1H, 29a-H), 4.56 (s, 1H, 29b-H), 4.49 (m, 2H, 28-H), 2.39 (s, 1H, 19-H), 3.63 (m, 113H, O-CH_2-), 1.92-0.73 (m, 42H, C_{sp3}-H); Figure 60.

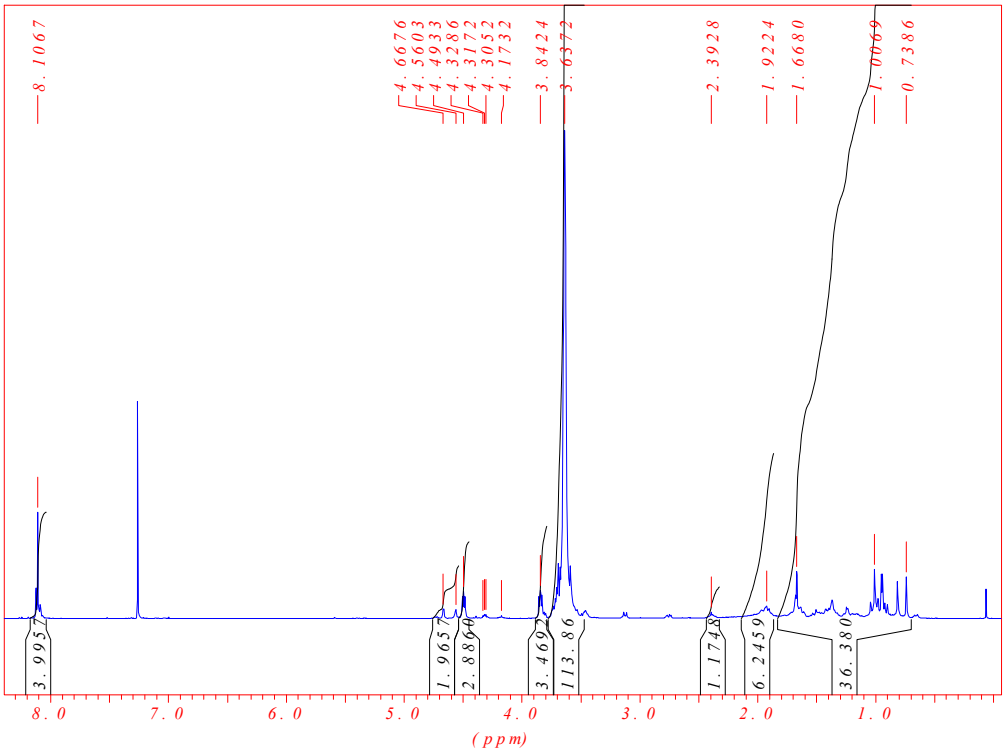

Figure 60. ^{1}H-NMR spectrum of a betulin-PEO-TPA polymer **7b**.

6.2 Characterisation

Differential scanning calorimetry (DSC)

DSC measurements were performed on a *DSC 1 STAR^{e} System* apparatus of *METTLER TOLEDO* under nitrogen atmosphere at a heating rate of 5 K·min^{-1}.

Dynamic light scattering (DLS)

DLS experiments were performed on a goniometer setup at angles of 30°-150° using a He-Ne laser (*Polytec*, 34 mW) operating at 633 nm. The instrument was equipped with a photon detector (*ALV/SO-SIPD*) and a digital correlator (*ALV 5000*).

Elemental analysis (EA)

Elemental analysis was obtained on a *Vario EL micro and macro CHNOS* elemental analyser.

Gas sorption

Prior to gas sorption measurements the samples were degassed at 70 °C *in vacuo*. The nitrogen and carbon dioxide sorption analyses were conducted on a *Quantachrome Quadrasorb* apparatus at 77 K and on a *Quantachrome Autosorb* apparatus at 247 K respectively. BET surface areas were determined over a p/p_0 range according to methods described elsewhere. Density functional theory (DFT) pore size distribution was determined using the carbon/slit-cylindrical pore model of *Quadrawin* software.

Gel permeation chromatography (GPC)

GPC with simultaneous UV/RI detection was performed at 25 °C with THF as the eluent and PSS-VS columns with average particle size of 5 μm and porosities of 10^3, 10^5 and 10^6 Å. Polystyrene (PSS, Mainz, Germany) and polyethylene glycol standards were used for calibration.

Infrared spectroscopy (IR)

Infrared spectra were collected in attenuated total reflection (ATR) mode (if not stated otherwise) on a *Thermo Nicolet FT-IR Nexus 470* instrument.

Nuclear magnetic resonance (NMR)

^{1}H-NMR measurements were carried out at room temperature using a *Bruker DPX-400* spectrometer operating at 400.1 MHz. $CDCl_3$ was used as a solvent.

Solid state **^{13}C-NMR** measurements were performed on a *Bruker Avance 400* spectrometer at a resonance frequency of 100.61 MHz and spinning frequency of 12 kHz. The ^{13}C-NMR scale was calibrated with adamantane as external standard (signals at 28.1 and 37.5 ppm).

^{129}Xe-NMR measurements were undertaken on a *Bruker MSL 300* at 83.0159 MHz. The samples were evacuated under vacuum, loaded with xenon and sealed. For each measurement 2000-10000 scans were performed using pulse length of 4.9 μs, a recycle delay of 6 s and magic angle spinning with a rotational frequency of 4 kHz. The xenon chemical shifts were referenced to the chemical shift of xenon gas extrapolated to zero pressure. The chemical shift of the sample was related to the signal at 77.8 ppm of the external standard (NaY zeolith, loaded with xenon at 526 mbar).

Scanning electron microscopy (SEM)

The SEM measurements were performed by using a *Gemini 1550* (*LEO, Zeiss AG*) instrument at acceleration voltage of 3 kV. The samples were prepared by spattering with Pd/C.

Small angle X-ray scattering (SAXS)

SAXS measurements were performed on a *Nonius* rotating anode instrument (4 kW, Cu Kα) with pinhole collimation and a *MARCCD* detector (pixel size 79, wavelength 0.154 nm). 2D diffraction patterns were transformed into a 1D radial average of the scattering intensity.

Thermogravimetric analysis (TGA)

TGA was performed on a *Netzsch TG 209 F1* apparatus in the range from 25 °C to 1000 °C with the heating rate of 10 K·min^{-1}.

Wide angle X-ray scattering (WAXS)

WAXS measurements were performed on a *D8 Advance* machine from *Bruker Instruments*. Cu-$K_{\alpha 1}$ radiation was used in reflection geometry. Samples powder was measured on a silicon holder.

6.3 Chemicals

1,3,5-benzenetricarbonyl trichloride, 98%	Sigma-Aldrich
Betulin, 98%	Sigma-Aldrich
[1,1'-biphenyl]-4,4'-dicarbonyl dichloride	TCI
Chloroform	Merck
Chloroform-d	Sigma-Aldrich
Desmodur RE (27% solution in EtOAc)	Bayer
1,4-dioxane	Sigma-Aldrich
Ethanol	Sigma-Aldrich
HCl solution, 1M	Merck
n-Hexane	VWR
Isophthalic acid chloride	Fluka
Mesitylene	Sigma-Aldrich
NaOH solution, 1M	Merck
Pyridine	99.5% extra dry, Acros Organics
Succinyl chloride	Sigma-Aldrich
Terephthalic acid chloride	99%, Sigma-Aldrich
THF	anhydrous, Sigma-Aldrich
Toluene	AppliChem
Triethylamine	Sigma-Aldrich; distilled prior to use

6.4 Nomenclature

ar	aromatic
ATR	Attenuated total reflection
BJH	Barrett, Joyner, Halenda (method)
br	broad
BTC	1,3,5-benzenetricarbonyl trichloride
COF	Covalent organic framework
CTF	Covalent triazine framework

δ	Chemical shift
Da	Dalton
dd	Double duplet
DSC	Differential scanning calorimetry
EtOAc	Ethylacetate
f_v	Fractional free volume
GPC	Gel permeation chromatography
h	hour
ΔH_{ads}	Differential enthalpy of adsorption
HCP	Hyper-crosslinked polymers
HK	Horvath and Kawazoe (method)
FTIR	Fourier transform infrared spectroscopy
IPC	Isophthalic acid chloride
IFM	Interference microscopy
IRM	Infrared microscopy
IUPAC	International Union of Pure and Applied Chemistry
K	Kelvin
λ	Mean free path
NLDFT	Non-Local Density Functional Theory
NMR	Nuclear magnetic resonance
m	multiplet
m	medium
M	molar
MALDI-TOF MS	Matrix-assisted laser desorption/ionisation time-of-flight mass spectrometry
MC	Monte-Carlo (method)
MOF	Metal organic framework
MOP	Microporous organic polymer
PALS	Positron anhilation spectroscopy
PDI	Polydispersity index
PET	Polyethylene terephthalate

PIM	Polymer of intrinsic microporosity
Py	Pyridine
q	Scattering vector
QSDFT	Quenched Solid Density Functional Theory
q_{st}	Isosteric heat of adsorption
RT	Room temperature
s	strong
SAXS	Small angle X-ray scattering
SEC	Size exclusion chromatography
SEM	Scanning electron microscopy
STP	Standard temperature and pressure (T = 273.15 K, p = 100 kPa)
T	Temperature
T_b	Boiling point
T_c	Crystallisation temperature
T_g	Glass transition temperature
TGA	Thermogravimetrical analysis
THF	Tetrahydrofuran
T_m	Melting temperature
TPC	Terephthalic acid chloride
UV	Ultraviolet
V	Specific volume
V_w	van der Waals volume
w	weak
WAXS	Wide angle X-ray scattering

6.5 Acknowledgements

I would like to thank Prof. Dr. Markus Antonietti for giving me the opportunity to work on my thesis at Max Planck Institute of Colloids and Interfaces and for suggesting an interesting project to work on.

A very big thank-you goes to Dr. Jens Weber for his excellent supervision, always great support and help throughout this time.

This work would not have been possible without the assistance of cooperation partners and technicians: Jessica Brandt, Dr. Winfried Boehlmann, Dr. Junpeng Zhao, Dr. habil PD Helmut Schlaad, Marlies Gräwert, Prof. Christian Jäger, Prof. Stefan Kaskel, Rona Pitschke, Miriam Unterlass, Irina Shekova, Olaf Niemeyer, Ingrid Zenke, Regina Rothe and Sylvia Pirok.

I want to thank my group, my office and lab mates and many of my colleagues for the nice atmosphere at the institute: Antje, Irene, Pablo, Sebastian, Filipe, Clara, Tim, Betty, Alfonso…

I am grateful to Jens, Deniz, Vladislav, Junpeng and Sebastião for proof-reading my thesis.

I would like to thank my friends who have been there for me during my time in Golm. I am very happy to have met so many wonderful people since I have come to live in Berlin for my diploma and later, for the PhD thesis. I am also grateful to my “old” friends for their interest and support.

I want to thank my family for always supporting my decisions, for their love and help, for believing in me. Without them I would not have gone to study to Germany, would not have had this education, would not have spent such amazing time discovering new places and meeting new people during my studies.

7 Literature

[1] A. Thomas, *Angewandte Chemie International Edition* **2010**, *49*, 8328–8344.
[2] R. Palkovits, M. Antonietti, P. Kuhn, A. Thomas, F. Schüth, *Angewandte Chemie* **2009**, *121*, 7042–7045.
[3] N. B. McKeown, P. M. Budd, *Macromolecules* **2010**, *43*, 5163–5176.
[4] H. C. Cho, H. S. Lee, J. Chun, S. M. Lee, H. J. Kim, S. U. Son, *Chemical Communications* **2011**, *47*, 917–919.
[5] F. Schüth, K. S. W. Sing, J. Weitkamp, *Handbook of Porous Solids*, Wiley-vch Verlag Gmbh & Co. Kgaa, **2002**.
[6] M. S. Silverstein, N. R. Cameron, M. A. Hillmyer, *Porous Polymers*, John Wiley & Sons, **2011**.
[7] P. M. Budd, E. S. Elabas, B. S. Ghanem, S. Makhseed, N. B. McKeown, K. J. Msayib, C. E. Tattershall, D. Wang, *Advanced Materials* **2004**, *16*, 456–459.
[8] P. M. Budd, B. S. Ghanem, S. Makhseed, N. B. McKeown, K. J. Msayib, C. E. Tattershall, *Chemical Communications* **2004**, 230.
[9] N. B. McKeown, P. M. Budd, K. J. Msayib, B. S. Ghanem, H. J. Kingston, C. E. Tattershall, S. Makhseed, K. J. Reynolds, D. Fritsch, *Chemistry - A European Journal* **2005**, *11*, 2610–2620.
[10] P. M. Budd, N. B. McKeown, B. S. Ghanem, K. J. Msayib, D. Fritsch, L. Starannikova, N. Belov, O. Sanfirova, Y. Yampolskii, V. Shantarovich, *Journal of Membrane Science* **2008**, *325*, 851–860.
[11] G. S. Larsen, P. Lin, K. E. Hart, C. M. Colina, *Macromolecules* **2011**, *44*, 6944–6951.
[12] W. Fang, L. Zhang, J. Jiang, *J. Phys. Chem. C* **2011**, *115*, 14123–14130.
[13] T. Emmler, K. Heinrich, D. Fritsch, P. M. Budd, N. Chaukura, D. Ehlers, K. Rätzke, F. Faupel, *Macromolecules* **2010**, *43*, 6075–6084.
[14] A. Thomas, P. Kuhn, J. Weber, M. Titirici, M. Antonietti, *Macromolecular Rapid Communications* **2009**, *30*, 221–236.
[15] P. M. Budd, N. B. McKeown, *Polym. Chem.* **2010**, *1*, 63–68.
[16] V. Guarino, F. Causa, A. Salerno, L. Ambrosio, P. A. Netti, *Materials Science and Technology* **2008**, *24*, 1111–1117.
[17] R. Demir-Cakan, N. Baccile, M. Antonietti, M.-M. Titirici, *Chem. Mater.* **2009**, *21*, 484–490.
[18] M. A. R. Meier, J. O. Metzger, U. S. Schubert, *Chemical Society Reviews* **2007**, *36*, 1788.
[19] A. Gandini, *Macromolecules* **2008**, *41*, 9491–9504.
[20] R. T. Mathers, K. Damodaran, M. G. Rendos, M. S. Lavrich, *Macromolecules* **2009**, *42*, 1512–1518.
[21] J. Zhao, H. Schlaad, S. Weidner, M. Antonietti, *Polym. Chem.* **2011**, DOI 10.1039/C1PY00388G.
[22] V. Ära, T. Mustonen, P. Jääskeläinen, *Macromol. Chem., Rapid Commun.* **1981**, *2*, 283–286.
[23] A. Lehtinen, V. Ära, T. Mustonen, E. Anttalainen, *Macromol. Chem., Rapid Commun.* **1980**, *1*, 499–502.
[24] V. Vasnev, I. Konkina, V. Korshak, S. Vinogradova, J. Lindberg, P. Jääskeläinen, K. Piiroinen, *Macromol. Chem.* **1987**, *188*, 683–691.

[25] K. S. W. Sing, R. T. Williams, *Particle & Particle Systems Characterization* **2004**, *21*, 71–79.
[26] D. H. Everett, *Pure and Applied Chemistry* **1972**, *31*, 577–638.
[27] K. S. W. Sing, *Pure and Applied Chemistry* **1985**, *57*, 603–619.
[28] S. D. Kimmins, N. R. Cameron, *Advanced Functional Materials* **2011**, *21*, 211–225.
[29] C. T. Kresge, M. E. Leonowicz, W. J. Roth, J. C. Vartuli, J. S. Beck, *Nature* **1992**, *359*, 710–712.
[30] Y. Wan, Y. Shi, D. Zhao, *Chem. Mater.* **2007**, *20*, 932–945.
[31] J. S. Beck, J. C. Vartuli, W. J. Roth, M. E. Leonowicz, C. T. Kresge, K. D. Schmitt, C. T. W. Chu, D. H. Olson, E. W. Sheppard, *J. Am. Chem. Soc.* **1992**, *114*, 10834–10843.
[32] D. Zhao, Q. Huo, J. Feng, B. F. Chmelka, G. D. Stucky, *J. Am. Chem. Soc.* **1998**, *120*, 6024–6036.
[33] M. Heuchel, D. Fritsch, P. M. Budd, N. B. McKeown, D. Hofmann, *Journal of Membrane Science* **2008**, *318*, 84–99.
[34] J. Weber, N. Du, M. D. Guiver, *Macromolecules* **2011**, *44*, 1763–1767.
[35] T. Masuda, E. Isobe, T. Higashimura, K. Takada, *J. Am. Chem. Soc.* **1983**, *105*, 7473–7474.
[36] A. K. Doolittle, *Journal of Applied Physics* **1951**, *22*, 1471–1475.
[37] S. Kanehashi, K. Nagai, *Journal of Membrane Science* **2005**, *253*, 117–138.
[38] W. R. Vieth, P. M. Tam, A. S. Michaels, *Journal of Colloid and Interface Science* **1966**, *22*, 360–370.
[39] A. S. Michaels, W. R. Vieth, J. A. Barrie, *Journal of Applied Physics* **1963**, *34*, 1–12.
[40] O. M. Ilinitch, V. B. Fenelonov, A. A. Lapkin, L. G. Okkel, V. V. Terskikh, K. I. Zamaraev, *Microporous and Mesoporous Materials* **1999**, *31*, 97–110.
[41] A. P. Côté, A. I. Benin, N. W. Ockwig, M. O'Keeffe, A. J. Matzger, O. M. Yaghi, *Science* **2005**, *310*, 1166 –1170.
[42] H. M. El-Kaderi, J. R. Hunt, J. L. Mendoza-Cortés, A. P. Côté, R. E. Taylor, M. O'Keeffe, O. M. Yaghi, *Science* **2007**, *316*, 268–272.
[43] R. Palkovits, M. Antonietti, P. Kuhn, A. Thomas, F. Schüth, *Angewandte Chemie International Edition* **2009**, *48*, 6909–6912.
[44] P. Kuhn, A. Thomas, M. Antonietti, *Macromolecules* **2008**, *42*, 319–326.
[45] P. Kuhn, M. Antonietti, A. Thomas, *Angewandte Chemie International Edition* **2008**, *47*, 3450–3453.
[46] M. J. Bojdys, J. Jeromenok, A. Thomas, M. Antonietti, *Advanced Materials* **2010**, *22*, 2202–2205.
[47] Y. Xiao, B. T. Low, S. S. Hosseini, T. S. Chung, D. R. Paul, *Progress in Polymer Science* **2009**, *34*, 561–580.
[48] M. K. Ghosh, K. L. Mittal, *Polyimides: Fundamentals and Applications*, Marcel Dekker, **1996**.
[49] N. Ritter, I. Senkovska, S. Kaskel, J. Weber, *Macromolecules* **2011**, *44*, 2025–2033.
[50] J. Weber, Q. Su, M. Antonietti, A. Thomas, *Macromolecular Rapid Communications* **2007**, *28*, 1871–1876.
[51] J. Weber, M. Antonietti, A. Thomas, *Macromolecules* **2008**, *41*, 2880–2885.
[52] Z. A. B. Z. Alauddin, P. Lahijani, M. Mohammadi, A. R. Mohamed, *Renewable and Sustainable Energy Reviews* **2010**, *14*, 2852–2862.
[53] G. Berndes, M. Hoogwijk, R. van den Broek, *Biomass and Bioenergy* **2003**, *25*, 1–28.
[54] "Fachagentur Nachwachsende Rohstoffe e.V.: Anbau," can be found under http://www.nachwachsenderohstoffe.de/service/daten-und-fakten/anbau/, **2012**.
[55] "Linoleum - Wikipedia, the free encyclopedia," can be found under http://en.wikipedia.org/wiki/Linoleum, **n.d.**

[56] S. Pilla, *Handbook of Bioplastics and Biocomposites Engineering Applications*, John Wiley And Sons, **2011**.
[57] H. Tian, Z. Tang, X. Zhuang, X. Chen, X. Jing, *Progress in Polymer Science* **2012**, *37*, 237–280.
[58] E. W. H. Hayek, U. Jordis, W. Moche, F. Sauter, *Phytochemistry* **1989**, *28*, 2229–2242.
[59] M. Kvasnica, J. Sarek, E. Klinotova, P. Dzubak, M. Hajduch, *Bioorganic & Medicinal Chemistry* **2005**, *13*, 3447–3454.
[60] S. Alakurtti, T. Mäkelä, S. Koskimies, J. Yli-Kauhaluoma, *European Journal of Pharmaceutical Sciences* **2006**, *29*, 1–13.
[61] C. Gauthier, J. Legault, M. Lebrun, P. Dufour, A. Pichette, *Bioorganic & Medicinal Chemistry* **2006**, *14*, 6713–6725.
[62] L. Tripathi, P. Kumar, R. Singh, *Current Bioactive Compounds* **2009**, *5*, 160–168.
[63] W.-Y. Lin, F.-H. Lin, S. Sadhasivam, S. Savitha, *Materials Science and Engineering: C* **2010**, *30*, 597–604.
[64] Y. Kashiwada, J. Chiyo, Y. Ikeshiro, T. Nagao, H. Okabe, L. M. Cosentino, K. Fowke, K. H. Lee, *Bioorganic & Medicinal Chemistry Letters* **2001**, *11*, 183–185.
[65] I.-C. Sun, H.-K. Wang, Y. Kashiwada, J.-K. Shen, L. M. Cosentino, C.-H. Chen, L.-M. Yang, K.-H. Lee, *J. Med. Chem.* **1998**, *41*, 4648–4657.
[66] J. Xiong, Y. Kashiwada, C.-H. Chen, K. Qian, S. L. Morris-Natschke, K.-H. Lee, Y. Takaishi, *Bioorganic & Medicinal Chemistry* **2010**, *18*, 6451–6469.
[67] V. E. Nemilov, T. V. Orlova, Y. S. Chulkova, *Russian Journal of Applied Chemistry* **2005**, *78*, 1162–1165.
[68] V. Nemilov, Nemilov, *ZHURNAL PRIKL HIM* **1999**, *72*, 1534.
[69] *Ullmann's Encyclopedia of Industrial Chemistry. 2003 Electronic Release: Online Plus CD-ROM*, Wiley-vch, **2003**.
[70] R. Brückner, *Reaktionsmechanismen: Organische Reaktionen, Stereochemie, Moderne Synthesemethoden*, Spektrum Akademischer Verlag, **2004**.
[71] B. Tieke, *Makromolekulare Chemie: Eine Einführung*, Wiley-vch Verlag Gmbh & Co. Kgaa, **2005**.
[72] P. J. Flory, *Principles of Polymer Chemistry*, Cornell University Press, **1953**.
[73] P. W. Atkins, J. de Paula, *Physikalische Chemie: Auflage V. 4*, Wiley-vch Verlag Gmbh & Co. Kgaa, **2006**.
[74] C. G. V. Burgess, D. H. Everett, S. Nuttall, *Pure and Applied Chemistry* **1989**, *61*, 1845–1852.
[75] M. A. Hernández, F. Rojas, V. H. Lara, *J. Por. Solids* **2000**, *7*, 443–454.
[76] J. Weber, A. Thomas, *J. Am. Chem. Soc.* **2008**, *130*, 6334–6335.
[77] K. S. Walton, R. Q. Snurr, *J. Am. Chem. Soc.* **2007**, *129*, 8552–8556.
[78] M. Thommes, R. Köhn, M. Fröba, *J. Phys. Chem. B* **2000**, *104*, 7932–7943.
[79] P. I. Ravikovitch, A. Vishnyakov, A. V. Neimark, *Phys. Rev. E* **2001**, *64*, 011602.
[80] P. I. Ravikovitch, A. V. Neimark, *Langmuir* **2006**, *22*, 11171–11179.
[81] V. Y. Gavrilov, R. S. Zakharov, *Kinet Catal* **2010**, *51*, 609–614.
[82] M. Om P., *Carbon* **1991**, *29*, 735–742.
[83] H. Marsh, W. F. K. Wynne-Jones, *Carbon* **1964**, *1*, 269–279.
[84] P. L. Walker Jr., M. Shelef, *Carbon* **1967**, *5*, 7–11.
[85] Y. Tsujita, *Progress in Polymer Science* **2003**, *28*, 1377–1401.
[86] R. Dawson, D. J. Adams, A. I. Cooper, *Chemical Science* **2011**, *2*, 1173–1177.
[87] A. F. Ismail, W. Lorna, *Separation and Purification Technology* **2002**, *27*, 173–194.
[88] Z. Zhang, Y. P. Handa, *Journal of Polymer Science Part B: Polymer Physics* **1998**, *36*, 977–982.

[89] R. Dawson, E. Stöckel, J. R. Holst, D. J. Adams, A. I. Cooper, *Energy & Environmental Science* **2011**, *4*, 4239–4245.
[90] A. Torrisi, R. G. Bell, C. Mellot-Draznieks, *Crystal Growth & Design* **2010**, *10*, 2839–2841.
[91] C. Dybowski, N. Bansal, T. M. Duncan, *Annual Review of Physical Chemistry* **1991**, *42*, 433–464.
[92] J. Fraissard, T. Ito, *Zeolites* **1988**, *8*, 350–361.
[93] K. W. Miller, *Proceedings of the National Academy of Sciences* **1981**, *78*, 4946–4949.
[94] T. Suzuki, M. Miyauchi, H. Yoshimizu, Y. Tsujita, *Polymer Journal* **2001**, *33*, 934.
[95] G. Golemme, J. B. Nagy, A. Fonseca, C. Algieri, Y. Yampolskii, *Polymer* **2003**, *44*, 5039–5045.
[96] S. Pawsey, K. K. Kalebaila, I. Moudrakovski, J. A. Ripmeester, S. L. Brock, *J. Phys. Chem. C* **2010**, *114*, 13187–13195.
[97] Y. J. Lee, K.-D. Park, S.-J. Huang, S.-B. Liu, H.-J. Lee, *Journal of Nanoscience and Nanotechnology* **2007**, *7*, 3932–3937.
[98] J. Weber, J. Schmidt, A. Thomas, W. Böhlmann, *Langmuir* **2010**, *26*, 15650–15656.
[99] M. A. Springuel-Huet, J. L. Bonardet, A. Gédéon, J. Fraissard, *Langmuir* **1997**, *13*, 1229–1236.
[100] T. Domeniconi, J.-L. Bonardet, M.-A. Springuel-Huet, J. Fraissard, J.-M. Dereppe, in *Catalyst Deactivation Proceedings of the 7th International Symposium*, Elsevier, **1997**, pp. 647–654.
[101] A. GÃ©dÃ©on, J. L. Bonardet, C. Lepetit, J. Fraissard, *Solid State Nuclear Magnetic Resonance* **1995**, *5*, 201–212.
[102] T. Ito, J. L. Bonardet, J. Fraissard, J. B. Nagy, C. AndrÃ©, Z. Gabelica, E. G. Derouane, *Applied Catalysis* **1988**, *43*, L5–L11.
[103] M. Springuel-Huet, J. Demarquay, T. Ito, J. Fraissard, in *Innovation in Zeolite Materials Science Proceedings of an International Symposium*, Elsevier, **1988**, pp. 183–189.
[104] J. Demarquay, J. Fraissard, *Chemical Physics Letters* **1987**, *136*, 314–318.
[105] B. Zhang, Z. Wang, *Chem. Mater.* **2010**, *22*, 2780–2789.
[106] M. M. O'Connell, M. D. Bentley, C. S. Campbell, B. J. W. Cole, *Phytochemistry* **1988**, *27*, 2175–2176.
[107] M.-F. Guidoin, J. Yang, A. Pichette, C. Roy, *Thermochimica Acta* **2003**, *398*, 153–166.
[108] J. Jeromenok, W. Böhlmann, M. Antonietti, J. Weber, *Macromolecular Rapid Communications* **2011**, *32*, 1846–1851.
[109] L. Pohjala, S. Alakurtti, T. Ahola, J. Yli-Kauhaluoma, P. Tammela, *J. Nat. Prod.* **2009**, *72*, 1917–1926.
[110] J. Hasegawa, K. Kanamori, K. Nakanishi, T. Hanada, S. Yamago, *Macromolecular Rapid Communications* **2009**, *30*, 986–990.
[111] J. Weber, L. Bergström, *Langmuir* **2010**, *26*, 10158–10164.
[112] J. Weber, J. Schmidt, A. Thomas, W. Böhlmann, *Langmuir* **2010**, *26*, 15650–15656.
[113] J. Garrido, A. Linares-Solano, J. M. Martin-Martinez, M. Molina-Sabio, F. Rodriguez-Reinoso, R. Torregrosa, *Langmuir* **1987**, *3*, 76–81.
[114] M. Thommes, C. Morlay, R. Ahmad, J. P. Joly, *Adsorption* **2011**, *17*, 653–661.
[115] S. E. Kentish, C. A. Scholes, G. W. Stevens, *Recent Patents on Chemical Engineering* **2010**, *1*, 52–66.

[116] N. B. McKeown, B. Gahnem, K. J. Msayib, P. M. Budd, C. E. Tattershall, K. Mahmood, S. Tan, D. Book, H. W. Langmi, A. Walton, *Angewandte Chemie International Edition* **2006**, *45*, 1804–1807.
[117] J. Germain, J. Hradil, J. M. J. Fréchet, F. Svec, *Chem. Mater.* **2006**, *18*, 4430–4435.
[118] R. Kirchheim, *Macromolecules* **1998**, *31*, 2349–2352.
[119] M. Wessling, I. Huisman, T. v. d Boomgaard, C. A. Smolders, *Journal of Polymer Science Part B: Polymer Physics* **1995**, *33*, 1371–1384.
[120] A. Bos, I. G. M. Pünt, M. Wessling, H. Strathmann, *Journal of Membrane Science* **1999**, *155*, 67–78.
[121] S. J. Gregg, K. S. W. Sing, *Adsorption, Surface Area, and Porosity*, Academic Press, **1991**.
[122] M. A. Banares-Munoz, V. Sanchez Escribano, *Langmuir* **1991**, *7*, 1779–1783.
[123] D. Lozano-Castelló, D. Cazorla-Amorós, A. Linares-Solano, *Carbon* **2004**, *42*, 1233–1242.
[124] F. Rodriguez-Reinoso, J. de D. Lopez-Gonzalez, C. Berenguer, *Carbon* **1982**, *20*, 513–518.
[125] K. Yang, Y. Lin, X. Lu, A. V. Neimark, *Journal of Colloid and Interface Science* **2011**, *362*, 382–388.
[126] P. I. Ravikovitch, A. V. Neimark, *Langmuir* **2006**, *22*, 10864–10868.
[127] J. Brandt, J. Schmidt, A. Thomas, J. D. Epping, J. Weber, *Polymer Chemistry* **2011**, *2*, 1950–1952.
[128] F. Hibbe, C. Chmelik, L. Heinke, S. Pramanik, J. Li, D. M. Ruthven, D. Tzoulaki, J. Kärger, *J. Am. Chem. Soc.* **2011**, *133*, 2804–2807.
[129] O. Glatter, O. Kratky, *Small Angle X-ray Scattering*, Academic Press, London; New York, **1982**.
[130] A. G. McDermott, G. S. Larsen, P. M. Budd, C. M. Colina, J. Runt, *Macromolecules* **2010**, *44*, 14–16.
[131] J. I. Feldblyum, M. Liu, D. W. Gidley, A. J. Matzger, *J. Am. Chem. Soc.* **2011**, *133*, 18257–18263.
[132] L. Heinke, J. Kärger, *Phys. Rev. Lett.* **2011**, *106*, 074501.
[133] S.-Y. Moon, J.-S. Bae, E. Jeon, J.-W. Park, *Angewandte Chemie* **2010**, *122*, 9694–9698.
[134] M. Hesse, H. Meier, B. Zeeh, *Spektroskopische Methoden in Der Organischen Chemie*, Thieme, Stuttgart, **2005**.
[135] A. S. El-Shahawy, A.-B. M. El-Nady, S. M. Ahmed, N. K. Sayed, *Spectroscopy Letters: An International Journal for Rapid Communication* **2006**, *39*, 163.
[136] H.-G. Elias, *Polymere*, Utb, Stuttgart, **1996**.
[137] C. Gao, D. Yan, *Progress in Polymer Science* **2004**, *29*, 183–275.
[138] D. Schmaljohann, B. Voit, *Macromol. Theory Simul.* **2003**, *12*, 679–689.
[139] S. Kuchanov, H. Slot, A. Stroeks, *Progress in Polymer Science* **2004**, *29*, 563–633.
[140] P. J. Flory, *Journal of the American Chemical Society* **1952**, *74*, 2718–2723.
[141] T. N. Drebushchak, M. A. Mikhailenko, M. E. Brezgunova, T. P. Shakhtshneider, S. A. Kuznetsova, *Journal of Structural Chemistry* **2010**, *51*, 798–801.
[142] M. A. Mikhailenko, T. P. Shakhtshneider, V. A. Drebushchak, S. A. Kuznetsova, G. P. Skvortsova, V. V. Boldyrev, *Chem Nat Compd* **2011**, *47*, 229–233.
[143] B. Voit, *Journal of Polymer Science Part A: Polymer Chemistry* **2000**, *38*, 2505–2525.
[144] N. Du, H. B. Park, G. P. Robertson, M. M. Dal-Cin, T. Visser, L. Scoles, M. D. Guiver, *Nature Materials* **2011**, *10*, 372–375.

[145] S. Jiang, J. Bacsa, X. Wu, J. T. A. Jones, R. Dawson, A. Trewin, D. J. Adams, A. I. Cooper, *Chem. Commun.* **2011**, *47*, 8919–8921.
[146] S. K. Sharma, A. Mudhoo, J. H. Clark, G. A. Kraus, *A Handbook of Applied Biopolymer Technology: Synthesis, Degradation and Applications*, Royal Society Of Chemistry, **2011**.
[147] "Polyurethanes from betulinol - Erä - 2003 - Die Angewandte Makromolekulare Chemie - Wiley Online Library," can be found under http://onlinelibrary.wiley.com/doi/10.1002/apmc.1980.050880106/abstract, **n.d.**
[148] V. Erä, P. Jääskeläinen, K. Ukkonen, *Journal of the American Oil Chemists' Society* **1981**, *58*, 20–23.
[149] M. R. Buchmeiser, *Polymer* **2007**, *48*, 2187–2198.
[150] J.-F. Lutz, H. G. Börner, *Progress in Polymer Science* **2008**, *33*, 1–39.
[151] H. Klok, *Journal of Polymer Science Part A: Polymer Chemistry* **2005**, *43*, 1–17.
[152] B. Obermeier, F. Wurm, C. Mangold, H. Frey, *Angewandte Chemie International Edition* **2011**, *50*, 7988–7997.
[153] D. Filpula, H. Zhao, *Advanced Drug Delivery Reviews* **2008**, *60*, 29–49.
[154] N. Bhattarai, J. Gunn, M. Zhang, *Advanced Drug Delivery Reviews* **2010**, *62*, 83–99.
[155] G. Pasut, F. M. Veronese, *Advanced Drug Delivery Reviews* **2009**, *61*, 1177–1188.
[156] B. Y. Chung, I. W. Jeong, I. J. Woo, S. S. Bang, H. S. Ko, J. H. Choi, *Pegylated Betulin Derivative, and Cosmetic Composition Containing the Same*, **2010**, U.S. Patent WO2010114305.
[157] J. Zhao, H. Schlaad, *Adv. Polym. Sci.* **n.d.**, DOI 10.1007/12_2011_166.
[158] J. Zhao, G. Mountrichas, G. Zhang, S. Pispas, *Macromolecules* **2010**, *43*, 1771–1777.

Eidesstattliche Erklärung

Hiermit erkläre ich, dass ich die vorliegende Dissertation selbstständig verfasst und keine anderen als die angegebenen Quellen und Hilfsmittel verwendet habe. Ferner erkläre ich, dass ich nicht versucht habe, anderweitig eine Dissertation einzureichen.

Jekaterina Jeromenok

Potsdam/Golm

März 2012

Publications and conference contributions

2012 J. Zhao, J. Jeromenok, J. Weber, H. Schlaad „Thermoresponsive Aggregation Behavior of Triterpene-Poly(ethyleneoxide) Conjugates in Water“, *Macromol. Biosci*. **2012**, DOI: 10.1002/mabi.201200131.

2012 Poster contribution at the „Sixth International Workshop on Characterization of Porous Materials – From Angstroms to Millimeters” in Delray Beach, Florida, USA, 30.04.-02.05.2012

2011 J. Jeromenok, W. Böhlmann, M. Antonietti, J. Weber, „Intrinsically Microporous Polyesters from Betulin-Renewable Materials for Gas Separation made from Birch Bark“, *Macromol. Rapid Commun*. **2011**, *32*, 1846-1851.

2011 Poster contribution at the „Second International Conference on Multifunctional, Hybrid and Nanomaterials”, Strasbourg, Frankreich, 06.03.-10.03.2011